EXPERIMENTS ON THE STABILITY OF THE FLAT-PLATE BOUNDARY LAYER WITH SUCTION

by

Gregory A. Reynolds

Dissertation submitted to the Graduate Faculty of the
Virginia Polytechnic Institute and State University
in partial fulfillment of the requirements for the degree of
DOCTOR OF PHILOSOPHY
in
Engineering Mechanics

APPROVED:

W. S. Saric, Chairman

D. P. Telionis

T. Herbert

P. R. Sparks

J. F. Marchman III

H. Nagib (I.I.T.)

January, 1982
Blacksburg, Virginia

ACKNOWLEDGEMENTS

The development and completion of the experiments described here could only have occurred through the help and cooperation of many individuals. While my appreciation cannot be expressed to each one here, I would like to extend my thanks to all those who helped. It has been my pleasure to see all these contributions come together as a working whole. Financial support for this work was through NASA grant NSG-1608.

In particular, I would like to thank my major professor, William S. Saric,for his help as an advisor, a co-worker, and as a good friend. His contribution to this work and to my education is quite significant and very much appreciated.

Also to be noted are Professors Thorwald Herbert, Demetri P. Telionis, James F. Marchman III, Peter R. Sparks, and Hasan Nagib (at I.I.T.) for their ideas and suggestions concerning the experimental work as well as the completion of this paper.

Special credit is due to for his dedicated work as the mechanical technician. His attention to detail in the machine work and his help in all aspects of the experiment have been a major contribution.

I would also like to express my appreciation to for her interaction with the experiment in providing her theoretical results for comparison. These interactions helped in directing the experimental program.

During various stages of the experiment, the help of ,
, and was significant in set-up and operation of the experiment. Their assistance and the contribution of their time has been very valuable.

Also to be noted was the continued interest of as evidenced by his frequent visits, and his willingness to share from his wealth of insight in the area of Laminar Flow Control.

The excellent job of typing has been done by my wife, . Her encouragement and prayers along with the support of my friends in the Body of Jesus Christ, has been a constant source of strength. Of course, to the one who answered these prayers I can acknowledge everything.

LIST OF FIGURES

LIST OF SYMBOLS

A(X)	disturbance amplitude as a function of x.
Cp	pressure coefficient, $Cp = (p - p_\infty)/\frac{1}{2}Ue^2$.
H	boundary layer shape factor; displacement thickness/momentum thickness.
m	the inverse of the exponent, n, in the hot-wire calibration equation.
n	exponent of the velocity in hot-wire calibration equation.
F	dimensionless frequency, $F = (2\pi\nu f/Ue^2) \times 10^6$.
f	dimensional frequency (Hz).
Q	suction flow rate.
p	static pressure.
R	Reynolds number based on the reference length $R = Ue\delta_1/\nu = (Rx)^{1/2}$.
Ru	square route of the unit Reynolds number, $Ru = (Ue/\nu)^2$.
Rx	Reynolds number based on distance from the leading edge, X. $Rx = UeX/\nu$.
Rt	Transition Reynolds number based on X.
U	velocity in the X or streamwise direction.
Ue, U_∞	streamwise velocity evaluated in the freestream.
$\bar{U}$	time averaged streamwise velocity.
u	mean streamwise velocity in the boundary layer.
u'	fluctuating component of the streamwise velocity.
v	mean normal velocity in the boundary layer.

v' fluctuating component of normal velocity, or fluctuating voltage.

$|\ '|$ root mean square (r.m.s.) of fluctuating components.

$\max|\ '|$ maximum of an r.m.s. quantity.

V d.c. component of anemometer output.

V_0 d.c. anemometer output at zero velocity.

X streamwise (chordwise) direction.

Y normal direction.

Z spanwise direction.

ϵ small parameter.

η boundary-layer variable in the direction normal to the wall, $\eta = y/\delta_r$.

σ disturbance growth rate.

δ boundary-layer thickness, $\delta = 5\delta_r$.

δ_r boundary-layer reference length $\delta_r = (\nu X/Ue)^{1/2}$.

δ^* displacement thickness.

θ momemtum thickness.

ρ density of air.

CONTENTS

Chapter I

INTRODUCTION

1.1 MOTIVATION

The behavior of boundary-layer flows has been of great interest ever since the first description of the boundary layer was given by Prandtl (1904). This was especially true when the character of the flow near a solid surface was considered in the light of Reynolds' (1883) earlier observations of the laminar and turbulent flow regimes. Real insight was gained into the laminar-to-turbulent transition process with the work of Schubauer & Skramstad (1947) in the first, truly low turbulence wind tunnel experiments. This work revealed that, as Tollmien (1929) and Schlichting (1933) had proposed, the transition process was closely linked to the laminar instability with respect to initially small disturbances in the boundary layer. These small disturbances would then play a significant role in the eventual laminar-turbulent transition, assuming the boundary layer was not prematurely tripped by surface roughness or high freestream turbulence, or other disturbances.

The transition process is still a topic of great interest especially for flows where viscous drag forces and heat transfer are important. In some cases it is conceivable to delay or even eliminate transition and the turbulent boundary layer. The subsequent decrease in the drag

coefficient of 60-80% in a laminar versus a turbulent boundary layer may contribute significantly to overall drag reduction. For example, in commercial transport aircraft, the viscous drag on the wings accounts for approximately 40-50% of the overall drag. If fully laminar flow can be maintained on the wings, overall drag may be reduced by 25%. Much of the work outlined here was motivated by this goal.

A number of instability mechanisms may be in operation in the boundary layer, and together these eventually lead to transition. The first type of instability is the viscous instability with respect to laminar boundary-layer disturbances, called Tollmien-Schlichting (T-S) waves. These waves are selectively amplified or damped depending on Reynolds number and wave frequency. Secondly, a three dimensional flow may exhibit cross-flow instability. The resulting inviscid instability may be of varying importance depending on the degree of wing sweep. Similarly, depending on the degree of curvature across the chord of the wing, the accompanying centrifugal forces may result in an instability due to the growth of streamwise Gortler vortices. Also of significance in transonic aircraft is shock-wave interaction with the boundary layer. The importance of all these mechanisms may be reduced by proper wing design. However, even under optimum conditions, the Reynolds number is usually high enough for the viscous instability to lead to transition.

A number of methods are known to stabilize laminar boundary layers and the application of these methods has been called Laminar Flow Control (LFC). Some of these methods include boundary-layer suction,

boundary-layer cooling in air, or heating in water. For use in aircraft, boundary-layer suction seems to be the most promising.

Boundary-layer suction is achieved by drawing air through the surface over which the boundary layer is formed. This may be accomplished by the use of either discrete suction holes or slots, or by the use of porous skin material. The pioneering work of Pfenninger and his co-workers showed that distributed suction slots seem to be the most promising method for maintaining laminar boundary-layer flows. They performed transition experiments on boundary layers in tube inlets (Pfenninger, 1961), on wings (Pfenninger & Groth, 1961), and over backward facing steps (Hahn & Pfenninger, 1973) and obtained non-turbulent boundary layers. The full-scale in-flight LFC tests carried out using a modified X-21 with wing suction through spanwise slots achieved 90% chord laminarization and a resulting 25% drag reduction. In these situations one could tolerate small growing disturbances if the growth did not become too large. Thus, the capability of accurately predicting the stability characteristics is essential for the design of an LFC aircraft because all of the airfoil and wing optimization studies, as well as the suction requirements, depend on the stability calculations. While the eventual goal of laminar flow control is to consider all of the instability mechanisms and how they can be controlled, the aim here was to consider the first step of this process, the viscous instability mechanism.

With these ideas in mind, the experiments were conducted to consider the stability of a laminar boundary layer on a flat plate with zero chordwise pressure gradient. In this case, for small amplitude T-S waves in the boundary layer, experimental results agree well with the linearized theory describing the disturbance behavior without suction. This type of experiment, first conducted by Schubauer & Skramstad (1947) and Strazisar et al. (1978) serves as the foundation for the more involved experiments. Thus the base state of the experiment was established by comparison with these existing data.

1.2 EXPERIMENTS WITHOUT SUCTION

The methods used here for investigating the behavior of T-S waves in the boundary layer were basically like those used by previous investigators. Periodic disturbances of known frequency were introduced into the boundary layer by means of a vibrating ribbon. The vibrating ribbon created fluctuating velocity components, u' and v' in the X and Y directions respectively, which were superposed on the mean boundary-layer flow. In this case the X-direction was parallel to the flow and the Y-direction was normal to the surface of the plate. A few boundary-layer thicknesses downstream of the vibrating ribbon the fluctuating disturbance components established themselves across the boundary layer into the regular pattern typified by the theoretical result shown in Figuru1001. With the use of a hot-wire anemometer, the distribution of the r.m.s. disturbance velocity, $|u'|$, through the boundary layer

was measured. The change in this disturbance amplitude was then measured in the streamwise direction.

A typical result of this type of measurement is shown in Figure 1.2. The Reynolds numbers R_I and R_{II}, where $d|u'|/dX = 0$, are the neutral stability points for a wave of a given frequency. The Reynolds number here was based on the reference length, $R = Ue\delta_r/\nu$. Between Branch I and Branch II is the unstable region where the amplitude grows. The locus of points R and R as a function of the dimensionless frequency, $F = 2\pi\nu f/Ue^2$, of the disturbance is the neutral stability curve presented in Figure 1.3. The lowest value of R found for all frequencies is the critical Reynolds number.

The results of the linear stability theory applied to laminar boundary-layer disturbances are also shown in Figure 1.3. Until recently, the linear stability theories considered the boundary-layer flow as being parallel. These models did not account for the growth of the boundary layer in the streamwise direction and hence did not fully agree with the experimental evidence. Recently however, linear stability theories which account for nonparallel-flow effects have shown much better agreement with experiment as illustrated in Figure 1.3. Recent work in this area was reviewed by Saric & Nayfeh (1977).

These linear models are valid when the velocity fluctuations in the boundary layer are small. In this case, the wave behavior is described by an eigenvalue problem and so it is not dependent on the disturbance amplitude. However, where the disturbances are large, the linear mo-

dels do not hold. For large-amplitude waves, nonlinear interactions are likely, which resulted in three-dimensionality and an exchange of energy between waves of different frequencies (Klebanoff et al. 1962; Kouvasznay et al. 1962; Kachanov et al. 1977, 1980; Saric & Reynolds, 1980). This type of behavior is very amplitude dependent and must be explained by nonlinear models. Recently, nonlinear models have been developed to predict two- and three-wave interaction (e.g., Nayfeh & Bozatli, 1980), but they are limited to two-dimensional waves.

Closely following and perhaps concurrent to the nonlinear wave development it is evident that the originally two-dimensional waves develop a three-dimensional character in the boundary layer (Klebanoff et al. 1962). Associated with the three dimensionality is a well defined spanwise periodicity and the simultaneous observation of unsteady r.m.s. disturbance amplitudes due to spanwise meandering. The exact character of this behavior appears to be Reynolds number and frequency dependent.

Further experiments on nonlinear and 3-D boundary-layer stability are currently being conducted at V.P.I. & S.U. using the experimental apparatus described here. These experiments will lead to an understanding of the nonlinear and 3-D interactions of T-S waves before transition. The influence of initial disturbance amplitudes on transition will also be investigated.

1.3 EXPERIMENTS WITH SUCTION

The experiments to measure the stability characteristics of the flat-plate boundary layer with suction were an outgrowth of the earlier experiments. With the mean-flow and linear disturbance behavior well established in the case without suction, the objective of the experiment was to investigate the stabilizing effect of suction on initially two-dimensional, growing T-S waves. It was desired that the results would be useful to the development and validation of theoretical models, to provide insight into the mechanism of laminar-flow stabilization by suction, and to provide information on the performance of the skin material for suction applications.

Because of physical constraints, it has not been possible to provide suction spacially continuous over a given surface, for example, an aircraft wing. Therefore suction was implemented by optimum positioning of needed suction levels through discrete suction slots or strips. The choice of a skin material to facilitate suction was a matter of availability and the preference as to the type of material most easily integrated into the aircraft application. The trend has changed from the previously preferred opened suction slots because of the high machining costs and because of the low structural contribution of the resulting surface material. The experiments described here used a porous Dynapore material which is described in more detail in Chapter 2. The Dynapore material provided the needed surface smoothness and porosity and could be arranged in porous strips or larger porous panels. This material was

available with current technology which was originally developed for the manufacture of filter materials. The use of Dynapore as a candidate for laminar flow control was first discussed by Pearce et al. (1978). Dynapore was less expensive than machining slots and does provided some structural contribution of its own. The alternate suction-hole configuration had previously not been considered because of the difficulty in producing small enough holes with the needed surface smoothness. However, methods using electron beams have been developed recently to produce very small 65 μm holes with very good surface quality. Perforated titanium using this method may currently be manufactured at a cost still lower than the cost of Dynapore material. The perforated titanium has a structural strength and surface quality essentially that of the original unperforated material. It remains to be seen how the perforated titanium performs for suction.

The Dynapore porous panels employed in these experiments were designed and fabricated specifically for the experiments at V.P.I. & S.U. by the McDonnell-Douglas Aircraft Co., Long Beach, California. The porous panels allowed suction to be provided through discrete porous strips or continuously over the chordwise length of the panel. This flexibility then allowed the suction distribution as well as suction intensity to be varied and optimized.

The findings of these experiments with discrete and continuous suction applied to the boundary layer over a flat plate are the primary topic of this report. The experimental apparatus is described in Chapter

2 and a description of the wind-tunnel facility, its capabilities, and its limitations for boundary-layer stability experiments are included. The flat-plate model and traversing mechanism are also described in this chapter. The experimental methods and results are presented in Chapter 3. The first section of Chapter 3 contains a description of the basic-state flow and the second section describes the linear-disturbance behavior. Some of the results with nonlinear, multiple-frequency T-S waves are presented in the third section of Chapter 3. Finally, in the fourth section of Chapter 3, the suction results with initially linear 2-D disturbances are discussed in detail and compared with theoretical predictions. Conclusions and remarks on the current state of the experiment are made in Chapter 4. A more detailed description of the instruments employed in the experiments is located in the Appendix.

Chapter II

EXPERIMENTAL APPARATUS AND INSTRUMENTATION

2.1 THE WIND-TUNNEL FACILITY

The experiments were performed in the V.P.I. & S.U. Stability Wind Tunnel. This wind tunnel was originally a NACA facility located at Langley Field in Hampton Virginia. Constructed in 1940, the facility was designed to provide a very low turbulence-level flow for conducting dynamic stability measurements. The wind tunnel was moved to V.P.I. & S.U. and reconstructed in 1958.

The facility is a closed loop tunnel and has an air-exchange tower which is open to the atmosphere. A plan view of the facility is shown in Figure 2.1. The air-exchange tower is located downstream of the fan and motor assembly and uses a boundary-layer bleed on the entry flow. The continual air exchange provides for temperature stabilization since the flow loop is otherwise closed and heat exchangers are not used. This air-exchange tower and the external flow loop configuration has the disadvantage of allowing the environmental conditions to influence the flow conditions. This was overcome by avoiding testing during periods of extreme temperature change and/or gusty wind conditions. During stable environmental conditions the facility provided a remarkably stable mean-flow velocity with no tendency to drift over time, even at very low flow velocities.

The flow is driven by a 4.3 m diameter propeller that has eight constant-pitch blades. Power for the fan is provided by a 450 kW, d.c. motor. This system is capable of providing stable, low-turbulence flow in the test section for the velocity range of 4.6 m/s to 67 m/s. Speed control is accomplished manually by a coarse and a fine rheostat control. The fan motor assembly is mounted on an isolated foundation.

Electrical power for the d.c. motor is supplied by a Westinghouse Model No. 28767 motor-generator. The motor-generator is also mounted on its own foundation. However, the generator rotational speed of 900 r.p.m., or 15 Hz, was found to be a source of vibration in the test section.

Turning vanes are located at each corner of the tunnel circuit in order to maintain uniform flow. The turning vanes have streamlined cross sections and are spaced every 30 cm along the diagonal of each corner, except the corner preceeding the turbulence screens, where the spacing between vanes is 7.6 cm. This last set of turning vanes is particularly important in reducing the existing large scale turbulence in the settling chamber and in this sense functions somewhat like a large scale honeycomb. The finer vane spacing in the last corner also reduces any large-scale vorticity which may be introduced in turning the flow. The relatively low air velocities in the settling chamber and through the turbulence screens allowes the remaining large scale turbulent eddies to be dissipated. The seven turbulence screens located in the 5.5 m by 5.5 m settling chamber are of 0.02 mm diameter stainless

steel wire with a mesh size resulting in an open-area ratio of 0.6. Experiments performed to determine optimum damping screen mesh size for low-turbulence experiments (Bradshaw 1965), suggested that screens should have an open-area ratio greater than 0.57. Each 5.5 m square screen panel is constructed from three 1.83 m x 5.5 m screens joined together. The two seams in each screen panel are approximately 2 mm wide. The screen panel furthest downstream has horizontal seams and alternate upstream panels are rotated 90 degrees. This results in four horizontal and three vertical sets of seams. The screens are drawn very tight and held by clamps around the inside perimeter of the settling chamber walls. The spacing between screens is 146 mm. The screen clamps are offset from the settling-chamber wall, which results in a 25 mm space around the perimeter of the screens. Due to the screen blockage, a wall jet is created as the flow leaves the turbulence screens. The settling chamber extends past the screens and allows the remaining small-scale turbulence to dissipate naturally before entering the nozzle. The flow undergoes a 9:1 area contraction as it passes through the nozzle and into the test section. Flow visualization in the nozzle with string tufts as well as hot-wire measurements in the wall boundary layer show that the boundary layers are not unusually thick and there is no separation bubble in the nozzle even at low speeds. This may be attributed to the wall jet mentioned earlier.

Present studies reveal that the facility has very good flow quality, even when compared with present-day wind-tunnel designs. For boun-

dary-layer experiments, extremely low freestream turbulence levels are necessary. These levels were found to be in the range of .02%-.04% of the freestream velocity. Moreover, the spectrum of the disturbances showed most of the energy below 20 Hz. The flow quality is discussed in more detail in Chapter 3.

The test section is 7.3 m long with a constant square cross section of 1.83 m. Since there is no allowance for growth of the wall boundary layers, a slight negative pressure gradient of approximately Cp = 0.3% per meter is present. Compensation for this pressure gradient was accomplished by adjusting the flat plate angle-of-attack and this is discussed in the next section. Since the zero pressure state is in the settling chamber, the test section is enclosed in an airtight control room. Thus, the problem of air leakage into the test section flow, is minimized. The diffuser angle is 3 degrees, and vortex generators are located at this point to ensure efficient diffuser operation.

2.2 THE FLAT-PLATE MODELS

Two flat-plate wind-tunnel models having 1.83 meter span and 3.7 meter chord were constructed for these experiments by the Brunswick Corporation, located in Marion, Virginia. The two plates were similar in construction, the primary difference being that the suction plate was built with cut-away locations to accomodate the porous insert panels. The features of this suction model will be described in detail here; for specific details concerning the other plate, used for the linear and nonlinear experiments without suction, consult Reynolds (1979). Other

than details concerning the porous panels, the two plates underwent the same preparation outlined below, and the same surface quality and tolerances hold for the two models. For general reference, the flat-plate model used in the non-suction experiments is shown in Figure 2.2.

The suction model was a laminated panel that consisted of a 19 mm paper honeycomb core sandwiched between two, 1 mm 6061-T6 aluminum sheets. The overall thickness of the panel was 21.6 mm. This design was chosen for its light weight, strength, and very flat surface that was insensitive to temperature and humidity changes.

The plate was constructed to accomodate suction panels with 0.3 m chord and 0.91 m span. The plate and suction panel locations are shown in Figure 2.3. At each panel location the front aluminum material was removed along with the paper honeycomb. On the back side of the plate, eight smaller holes were located for each panel to facilitate suction-air removal, as shown for panel location #4 in Figure 2.3. These openings in the front and back aluminum material were punched out before lay-up with the paper honeycomb, thus providing flat surfaces and clean, well formed openings for flush mounting of the suction panels.

Static pressures on the test side of the plate were measured by 98 static pressure ports. Each pressure port consisted of a 6.3 mm diameter cylindrical aluminum insert with an orifice at one end and a copper tube at the other end, as shown in Figure 2.4. This configuration permited easy and reliable attachment of pressure tubing and provided static pressure measurements without disturbing the flow. The pres-

sure-port inserts were press-fit into holes in the flat plate and potted in place. This arrangement is shown in Figure 2.5. The 98 pressure ports shown in Figure 2.3 were located to provide the spanwise and chordwise pressure measurements. The mounting of a number of fixtures on the back of the plate was facilitated by a number of 1/4 x 28 threaded inserts which were flush mounted and held in place by fiberglass potting resin. The leading edge and the electromagnets for the vibrating ribbon were mounted using these threaded inserts. An additional aluminum threaded insert was located under one of the vibrating-ribbon locations to allow positioning of an inductance probe for ribbon vibration monitoring. Plexiglass inserts were potted into the plate at four streamwise locations to allow insertion of the smoke-wire apparatus through the plate for placement in the boundary layer. The smoke-wire apparatus is briefly discussed in the next section. After the pressure ports and various inserts were installed, surface irregularities were removed from the entire test surface of the plate by hand finishing with 600 grit paper and rubbing compound. The surface was cleaned with a weak phosphoric acid jelly after which a protective coat of wax was applied. Height-gauge measurements of the test surface indicated that local variations from flatness did not exceed 0.1 mm and were generally less than 0.03 mm.

A 0.34 m x 1.83 m tapered leading edge was mounted, as shown in Figure 2.6, onto the front of the plate which gave a total model length of 4.0 m. The leading edge had an elliptical profile with a major-to-mi-

nor axes ratio of 67:1. This leading-edge profile was chosen to minimize the pressure rise in the region of the stagnation point and yet be insensitive to leading-edge separation at slight angles-of-attack.

The leading edge was fabricated by Dynamic Engineering Inc. in Newport News, Virginia. The elliptical profile was machined from a single piece of aluminum using a numerically controlled milling machine. Tolerances for the profile shape were ±0.03 mm near the stagnation region and ±0.1 mm near the flat-plate junction. A surface finish of 8 m (r.m.s.) was obtained by hand polishing. Four mounting brackets were epoxied to the notched area at the root of the leading edge and these brackets bolt directly to the back side of the plate with sixteen threaded inserts.. The brackets bolted directly to the back side of the plate with sixteen threaded inserts. At the leading edge/plate junction, the leading edge was parallel to the front surface of the plate. Due to the different thermal coefficients of expansion of the two materials, a slight step or gap resulted at the junction. This step or gap was generally less than .02 - .05 mm and was easily faired by using a polyester patching compound (Bondo). Repair of the leading-edge junction was usually necessary only when the seasons of the year changed which resulted in large temperature changes from the previous test series.

A variable-deflection trailing-edge flap was attached to the downstream end of the flat plate in order to control the position of the attachment line on the leading edge. The flap balanced the wind-tunnel blockage between the front and back sides of the plate in order to pre-

vent leading-edge separation. The trailing-edge flap was adjustable from zero deflection to a maximum of 33 degrees toward the test side of the plate. The flap was constructed from a 1.83 m x 0.28 m plexiglass sheet which was hinged at the plate-flap junction and had a tapered, sharp trailing edge.

Using the suction model described here, any suction panel configuration, that is, having surface slots, holes, or porous surface material, could be flush mounted and tested. In addition, threaded inserts were located so that the leading edge could be mounted on either end of the model. This allowed the plate to be mounted so that suction could be applied either fore or aft on the model, over a wide range of test conditions.

2.3 SMOKE WIRE

The smoke-wire technique developed at I.I.T. by Corke et al. (1974) was modified in various experiments at V.P.I. & S.U. in an attempt to visualize Tollmien-Schlichting waves in the boundary layer. The apparatus was adapted to the flat plate to allow insertion of the wire support tubes through the plate itself. This configuration, shown in Figure 2.7, provided easy placement of the wire parallel to the plate within the thin boundary layer. It was found that this technique permitted visualization of flow abnormalities and T-S waves, (Weber et al. 1980).

2.4 POROUS SUCTION PANELS

The porous surface material configuration was used in these experiments. The porous material, called Dynapore, was originally developed as a filter material but also has the surface smoothness needed for laminar flow control. Dynapore is a woven stainless material of 80 x 700 mesh with an 80 x 80 mesh backing layer. The woven mesh material undergoes a calendering process which reduces the porosity to the desired level and produces a very smooth finished material. Two porous panels were used in the suction experiments and these were designed and constucted at McDonnell-Douglas Aircraft Company, Long Beach, California, based on the work of Pierce et al. (1978).

A cut-away view of a porous panel installed in the model is shown in Figure 2.8 and a chordwise cross-sectional view of this assembly is shown in Figure 2.9. The Dynapore material was bonded to a porous fiberglass material which in turn was sewn to a corrugated paper sheet. This assembly was then bonded to a 3 mm solid fiberglass sheet. This construction provided structural support as well as air ducting, with each spanwise corrugation or flute being isolated from its neighbor. Along each spanwise flute, a series of 0.48 cm diameter holes were located in the fiberglass backing sheet. These holes were placed every 100 mm to allow uniform air flow through the panels. Opening or blocking of these holes allowed the appropriate flutes to be "on" or "off" to obtain the desired chordwise suction distribution. The suction distribution could be varied, ranging from continuous suction over 254 mm with

all fifteen flutes opened, to discrete strip suction over 16mm with only one flute opened.

Inspection of the finished panels revealed some curvature across the chord of each panel, apparently due to residual stresses left from the manufacturing process. This curvature resulted in a concave surface on the front of the porous panels, with a maximum deflection from flatness of 0.5 mm. Under test conditions, this corresponded to a Görtler number of over 50, a situation known to be unstable for streamwise vortices (e.g. Floryan & Saric, 1980). To remove this curvature, a series of aluminum bars were epoxied to the fiberglass backing sheet across the chord of each panel, as shown in Figure 2.8. The desired panel flattness was insured by curing this assembly between the pressure plates of a temperature controlled hydraulic press. The resulting deviation from flatness on the front surface of the panels was .05 mm at the maximum.

Once placed in the flat plate, each suction panel rested against a cushion gasket located around the circumference of the panel/plate junction and was held in place via 32 threaded inserts located on the back of each panel. Corresponding machine screws pulled the panel firmly against the cushion gasket and were then adjusted to bring the porous surface of the panel flush with the front surface of the flat-plate model. The clearance gap remaining between the panel and the flat plate was filled with polyester patching compound (Bondo) and then sanded smooth by hand. In addition to providing a smooth surface at the junction, the patching compound insured an airtight installation.

2.5 SUCTION SYSTEM

The suction system provided a constant mass flow rate to the suction panels thus allowing variable suction configurations to be easily compared and optimized. Constant mass flow rate was accomplished using a sonic choking nozzle which controlled flow into a vacuum tank. A schematic of the suction system is shown in Figure 2.10. The sonic nozzle provided constant mass flow rate from one test configuration to another as well as throughout a given test, which eliminated the need of constant adjustment of the suction flow rate. The sonic nozzle also eliminated noise generated in the primary suction piping and the vacuum pump from propagating upstream to the suction panels. When the nozzle flow became unchoked, it was easily observed from a mercury manometer connected to pressure taps on the nozzle. Changes in the mass flow rate were accomplished with the choice of three choking nozzles, giving nominal volume flow rates of ; 60.1, 211.2, and 428.4 liters/min. The nozzles were constructed from plexiglass, and their geometry is shown in Figure 2.11. Using the 12.4 cubic meters plenum tank and two small vacuum pumps, the experiment could be operated continuously.

The total mass flow rate was divided between the two suction panels in a ratio depending upon the relative blockage of each. The flow rate through each panel was monitored by an in-line J-TEC flow meter (A.19). This device uses a vortex shedding strut and an ultrasonic detector which provides an output frequency that is linearly proportion-

al to flow rate over the range 7.01 liters/min to 280 liters/min. Accurate measurement of the frequency was obtained using the spectrum analyzer and the appropriate calibration factor.

Before the flow meters, the suction flow passed into a header as shown in Figure 2.10. The header served to join the eight suction hoses from each porous panel into one line leading into the corresponding flow meter. Each of the hoses leading into the header provided suction flow from one of the exit holes on the back of the plate, shown in Figure 2.8. Each of these eight suction hoses branched into three smaller lines which then connected to the primary manifold on the back of the plate. So the suction lines for each panel then branched from one to eight to twenty four. At each stage of this process all hose lengths were equal so that within each stage the head loss was the same for each line.

2.6 VIBRATING RIBBON

The introduction of controlled disturbances into the boundary layer was accomplished using the vibrating ribbon technique first used by Schubauer & Skramstad (1947). This method still seems to be the most satisfactory one for the introduction of two-dimensional waves.

The ribbon material was a spring-tempered, phosphor-bronze alloy which was 0.025 mm thick and was obtained in precut widths of 2.5 mm. This ribbon was stretched across the span of the plate generally at a position $X = 48.3$ cm from the leading edge of the model. When placed

in a constant magnetic field the ribbon then vibrated at the frequency of the alternating current passed through it.

The necessary magnetic field was generated with thirty-eight electromagnets mounted on the back of the plate in two parallel rows. This magnet configuration is shown in Figure 2.12. The two rows of magnets had opposite polarity, producing uni-directional field lines parallel with the flow. Visualization of these field lines on the front surface of the plate can be found in Figure 2.13.

The ribbon tension was applied using a spring scale which was accurate to within 1 Newton. A tension of 20 Newtons was found to be satisfactory. Ribbon clamps on the back of the plate held the ribbon in tension and provided electrical contact. The freely vibrating length of the ribbon was generally 0.4 m and this length was centered at mid-span of the plate. The ribbon was held above the plate surface by a thin glass rod at each end of this 0.4 m length. The glass rod diameter was typically 0.2 mm; approximately a distance $y/\delta_r = 0.17$ in boundary layer coordinates. Careful placement of the ribbon made it possible to operate at freestream velocities of Ue = 15 to 20 m/s without exciting flow-induced vibration of the ribbon. Outboard of its 0.4 m vibrating length, the ribbon was taped to the plate after being insulated from the plate by a layer of transparent tape.

The variable parameters that affected the ribbon amplitude and frequency of vibration were the magnetic field strength, the alternating current in the ribbon, the tension, and length of the ribbon. Measurements of the ribbon amplitude and frequency as a function of the

parameters mentioned above provided a direct indication of the disturbances introduced by the ribbon. These measurements were accomplished by means of the inductance probe (A.16) which was flush mounted on the surface of the plate beneath the ribbon. These diagnostic measurements in the wind tunnel were combined with more detailed laboratory experiments in order to more precisely determine the various vibrational characteristics of the ribbon. These characteristics were especially important when nonlinear vibrational response of the ribbon could be confused with nonlinear disturbance behavior in the boundary layer. It was also found that the ribbon could easily be excited in its torsional mode if special care was not taken in tensioning and clamping the ribbon. A detailed description of this work may be found in Saric et al. (1982).

A number of characteristics were particularly important concerning the type of disturbances introduced by the ribbon. Measurements of the peak ribbon amplitude and spanwise phase gave an indication of the uniformity of displacement. A spanwise plot of the ribbon phase relative to the driving signal, shown in Figure 2.14, indicated a first-mode ribbon vibration, which was the case for single as well as double-frequency ribbon excitation. The phase shift of 180 degrees was due to the polarity of the magnet connections. Spectrum analysis of the ribbon vibration also indicated that harmonics of the fundamental driving frequency were present only at a low level. This was insured by using low vibration amplitudes and by the use of a low-pass filter on the

driving oscillator's output. The low-pass filter reduced the second-harmonic, present in most oscillators, from 1%-2% to 0.1%. Introduction of the second harmonic to the ribbon was avoided since this frequency could be near to the ribbon's natural frequency and the ribbon response at this frequency could produce an amplitude as large as the fundamental.

2.7 TRAVERSING MECHANISM AND TEST SECTION CONFIGURATION

The test-section layout of the flat plate experiment is shown in Figure 2.15. As shown there, the flat plate was mounted vertically and was offset from the centerline of the test section. The traversing mechanism moved in the X-direction along the 4 m chord of the model on ground steel guide rods and adjustable precision ball bushings. While the flat plate was mounted at a slight positive angle-of-attack, the guide rods were mounted parallel to the tunnel walls.

Precise placement and alignment of the X-direction guide rods within the test section was accomplished using a surveyor's transit. The goal of the alignment procedure was to place the rods parallel with the flow and, of course, parallel with one another so that smooth traverse operation was insured. The transit was therefore used to establish both the rod elevation and azimuthal alignment. The elevation adjustments were accomplished with the use of shims at each of the five support locations along each support rail. At each of these locations, side-to-side movement was possible for the azimuthal adjustment. The sightings used for

these adjustments were established from base points located at the nozzle exit and diffuser entrance so that slight local variations in test-section dimension did not influence the traverse alignment. The process of rod alignment consisted first of setting the elevation of the bottom rod to within 0.05 mm of the established level. Once that level was established, the azimuthal adjustment was made to within 0.08 mm of the line of sight parallel with the side walls. The separation between the top and bottom rails was set using a gauge rod of the desired length. The last step was then the azimuthal alignment of the top rod. Adjustments of the top rod were conducted with the same accuracy as was used for the bottom rod.

The traversing mechanism moved fore and aft along the guide rods, pulled by a chain drive loop which was attached to the front and back of the traverse. Half of the chain loop was external to the test section, under the floor,where it moved along idler pulleys and over the drive sprocket. The traversing mechanism itself initially provided two additional directions of motion. The motion of the traverse in the Y-direction (normal to the plate) was the most demanding in terms of the needed accuracy. In this direction the motion was again along guide rods with ball bushings, but was driven by a precision lead screw.

Traverse motion in the spanwise or Z-direction was accomplished by moving the Y-traverse mechanism vertically along guide rods using a double purchase chain drive system. The double-purchase chain arrangement was used primarily to reduce the torque requirements and

hence the size of the Z-traverse drive motor. The Y- and Z-drive motors were mounted on the traversing mechanism and the whole assembly was enclosed in a streamlined fairing. The traversing mechanism employed stepping motors in all three traverse directions. These motors provided accurate and reproducible traverse motion over a wide range of speeds. Most importantly however, the stepping motors provided the means to accurately determine the traverse position by counting motor pulses. The capabilities of the 3-D traversing mechanism in terms of range of movement and accuracy are shown in Figure 2.16. Details of the design and construction of this traversing mechanism were given by Cousins et al. (1978) and a description of the traverse in its finished form was given by Saric et al. (1982).

Since most measurements in the flat-plate experiment were conducted along the midspan (Z = 0) of the plate, a 2-D traverse was constructed to provide movement in the X-, and Y-directions alone. Elimination of the Z-traverse greatly simplified the traverse construction and thus provided simpler operation and a thinner cross-sectional profile. The 2-D traverse made use of the same X- and Y-traverse mechanisms, however the Z-mechanism was replaced by a 1.27 cm thick plate which spanned to the top and bottom bearing blocks and supported the Y-traverse mechanism at a fixed mid-span position. Additional details concerning this device are described in Reynolds (1979). The influence of this traverse on the mean-flow field is discussed in Chapter 3.

2.8 TRAVERSE CONTROL

The traversing mechanism was operated in either a manual or an automatic mode. The center of the control system was three SLO-SYN model ST103 translators (A.12.1) which provided trigger pulses and the appropriate voltage levels to drive the stepping motors. A central control panel was added to provide convenient selection of the motor stepping modes available through the ST103. Motor movement in the manual mode could be initiated through either the ST103 Translator, the central control panel, or through a remote hand held control box.

Automatic movement of the traverse was also possible in the Y-traverse direction, in which case the ST103 Translator was replaced by a SP153A Preset Indexer (A.12.2). With this unit, a preset motion is initiated when a trigger pulse is received. When in the external mode, the SP153A accepts appropriate trigger pulses from an external source. In this case, the pulses were provided by the HP98035A timing clock (A.3.4) peripheral on the HP9825 calculator/controller (A.3.3). The trigger pulses from the HP98035A are not of the correct duration or shape to trigger the SP153A, so an interface circuit was constructed to complete the link between these instruments. This interface circuit (A.12.4) allowed communication between the HP9825 controller and the SP153A indexer to the extent that the controller could initiate the motor movement and then monitor the motor-status signal sent from the indexer via the interface. The interface circuit consisted primarily of a 555 timing chip and a 5 volt d.c. power supply, as shown in Figure 2.17.

The HP9825 calculator/controller also controls the 40-channel data acquisition system and the I/O devices,(A.3). Thus the traverse movement, the data sampling, and the data processing and output could be coordinated automatically through the HP9825.

In conjunction with these systems a three-channel digital counter (A.12.3) was constructed to count motor steps and indicate the traverse position. For both manual and automatic operation, the counter received trigger pulses from the ST103 or SP153A controllers. These pulses were counted as the traverse moved from some zero position. The resulting count was displayed by a binary LED display which provided a precise representation of distance traversed in terms of the number of motor steps. The binary display served as a diagnostic tool to double check the corresponding analog outputs obtained by D-A converting each of the three channels. This analog d.c. voltage provided inputs to the data-acquition system as an indication of traverse position. For visual observation, these d.c. voltages were also displayed by three panel-mounted digital voltmeters. The details of the traverse control system is contained in Saric et al. (1982).

2.9 INSTRUMENTATION

The instrumentation involved in signal processing and data acquisition are discussed in this section. The instruments will be mentioned in terms of their function in the experiment. An actual description of the equipment itself is given in Appendix A.

Measurements of mean and fluctuating flow velocities were obtained almost exclusively by hot-wire anemometry. Up to four independent anemometer channels were used at a given time. Each channel consisted of a DISA 55D01 anemometer unit operated in the constant temperature mode, a DISA 55D10 linearizer, and a DISA 55D35 r.m.s. unit. The King's-Law linearization provided by the 55D10 linearizer proved to be quite sufficient for the velocity ranges between 5 m/s and 30 m/s encountered in these experiments. The appropriate linearization exponent was determined by calibration against a Dwyer 160-DF pitot-static tube located 300mm ahead of the leading edge of the model. Linearization of hot-wire probes was handled through the HP 3052A automatic data-acquisition system, as was much of the data gathering process. Since linearization was relatively simple and fast, daily temperature variations were handled by relinearization instead of temperature compensation.

Various analog signal processing arrangements were employed, depending of course on the type of measurement to be made. In general, the anemometer output was linearized by the DISA 55D10 linearizer but this unit introduced a significant level of 60 Hz line noise into the signal. If this 60 Hz noise was particularly undesirable for a given mea-

surement, the linearizer was bypassed, if possible. A simple arrangement for analog processing of the anemometer output is shown in Figure 2.18.

Because the a.c. portion of the anemometer output was usually very small, a Tektronix AM 502 differential amplifier was used at the anemometer or linearizer outputs. The differential amplifiers were also equipped with low-pass (L-P) and high-pass (H-P) filters. The L-P filter was used to eliminate the high-frequency noise characteristic of the constant-temperature anemometer. A Spectral Dynamics SD-121 band-pass (B-P) filter was used when it was necessary to obtain a discrete frequency component of the anemometer output. The SD-121 was a tracking filter and as such was tuned to a given frequency by a reference signal usually supplied by the same oscillator which drove the vibrating ribbon. The same oscillator usually supplied a reference signal to the Spectral Dynamics SD-110-1 phase meter, which then produced a d.c. voltage proportional to the phase difference between the input signal and the reference signal. Measurements of the phase of a T-S wave versus X then provided the wavelength of the disturbance. All of the data was ultimately reduced to digital form. Digital plotting of the data proved advantageous over analog output because of the added capability to average slightly unsteady signals to obtain more repeatable results.

The heart of the digital processing system was the automatic data-acquisition system which could handle up to 40 input channels. The

components included the HP3495A scanner, the HP3455A voltmeter, the HP9872A four pen digital plotter, and the HP9825A calculator/controller. Measurements of d.c. as well as a.c. voltages could be made through the HP3455A voltmeter. The HP9825 calculator/controller was the controlling unit for the data acquisition system and also optionally for the spectrum analyzer, and for the traverse mechanism, as mentioned earlier.

2.10 EXTENSION ARM

Placement of the hot-wire probe beyond the influence of the traversing mechanism was accomplished with the hot-wire extension arm or sting. The hot-wire sting was mounted on the Y-traverse sliding block and extended 0.61 m ahead of the traversing mechanism as shown in Figure 2.15.

In order to obtain the needed rigidity and thin profile, the sting was constructed from a laminated composite. The sting was constructed at V.P.I. & S.U. and consisted basically of two parts; the root and the extension. The root of the sting, which attached to the Y-traversing mechanism, was a laminated Kevlar material, with an overall post-cure thickness of 4.76 mm. The extension arm which held the probe extension tube was a laminated graphite composite, which was laid up from 21 layers of pre-impregnated, mono-directional graphite material. To obtain maximum strength in bending as well as torsion, the plies were layered with the following filament orientation: 0, 90, +45, -45, 90,and

0 degrees. The resulting post-cure thickness of the graphite extension was 3.17 mm. The two parts of the sting, the root and the extension, were butted end-to-end and laminated between two aluminum facing sheets, which resulted in a total thickness at the root of 6.35 mm. The hot-wire probe was mounted at the end of a 4.76 mm o.d. stainless steel tube, which extended from a pen vise at the end of the sting.

The sting configuration described above proved to be quite effective. The degree of vibration encountered was found to be well within tolerable limits and interference with the hot-wire measurements was not a problem.

To monitor the hot-wire probe position and vibration relative to the surface of the plate, a Bentley Nevada inductance probe (A.16) was mounted at the end of the sting extension arm. Using this transducer, the distance from the plate as well as the vibration frequency spectra relative to the plate was monitored and compared with the spectra from the hot-wire anemometer. This was a diagnostic tool which allowed the vibrational components of the hot-wire signal to be observed. These measurements are described in Chapter 3.

2.11 TRANSITION EXTENSION TUBE

An extension-tube probe holder was constructed to facilitate transition Reynolds-number measurements which were conducted along X and at a fixed Y. This probe holder allowed the hot-wire probe to be held firmly at a fixed Y-distance in the boundary layer while being moved by the X-traverse. The extension tube, shown in Figure 2.19, was hinged at a point and the probe holder was spring loaded away from the plate. When brought into contact with the plate by movement of the Y-traverse the probe holder rotated until both support feet rested firmly on the surface of the plate.

2.12 FIXED PROBE MOUNT

Hot-wire measurements were also taken in the boundary layer using the fixed probe mount shown in Figure 2.20. This probe mount was taped directly to the surface of the plate and was used primarily as a diagnostic tool to allow comparison with signals obtained from a hot-wire probe mounted on the traverse sting. The fixed probe mount could also be used to determine the transition Reynolds number on the flat-plate model. Specific applications for this device are described in Chapter 3.

Chapter III

PROCEDURES AND RESULTS

3.1 MEAN-FLOW PROPERTIES

A number of preliminary measurements were necessary in order to determine the characteristics of the mean flow past the model. The primary requirement was that the freestream turbulence level be very low. Otherwise, freestream disturbances would cause premature transition of the laminar boundary layer to turbulence, thereby obscuring the evolution of the laminar boundary-layer disturbances or T-S waves which were being studied here. With the use of proper wind-tunnel design, the turbulence level may be reduced from typical values of 1% to 10% of the freestream velocity down to as low as 0.01% to 0.02% of Ue. Schubauer & Skramstad (1947) showed that in so doing, the transition Reynolds number, Rt, was increased to Rt = 3 x 10^6. The turbulence level in the V.P.I. & S.U. Stability Wind Tunnel is reduced by the settling chamber, the seven turbulence damping screens, and the 9:1 area contraction ratio. The streamwise velocity fluctuations in this facility are in the range $|u'|$ = 0.02% to 0.04% of Ue for a velocity range of 6 m/s to 30 m/s. These levels remain consistently low if precautions are made to periodically clean the screens of small debris which tend to enter the flow through the air-exchange tower.

3.1.1 Turbulence Levels

Measurements of the freestream turbulence were made using a DISA 55P05 boundary-layer type hot-wire probe. Two-wire turbulence probes which allow the elimination of electronic noise were tried but were not found to be necessary since the frequency of the electronic noise was much higher than the natural turbulence spectra. The signal processing for turbulence measurements is shown in Figure 3.1. As shown, the linearizer unit was bypassed and the signal was low-pass filtered at 1000 Hz so that electronic noise was reduced. Determination of the turbulence level was based on King's Law,

$$V^2 = V_0^2 + BU^n$$

which related the anemometer output voltage, V, to the velocity, U, being measured by the hot wire. Expressing V and U in terms of their steady and fluctuating parts,

$$U = \overline{U} + u' \qquad V = \overline{V} + v'$$

King's Law then provided the first order expression for the disturbances,

$$|u'| / U = 2m\overline{V}|v'| / (\overline{V}^2 - V_0^2).$$

Where the fluctuating components, u' and v' have been expressed in terms of their root mean square, and m = 1/n.

The turbulence level and corresponding spectrum for a freestream velocity of 15 m/s is shown in Figure 3.2. Variations in the freestream turbulence levels were not found in the spanwise direction. Moreover, the turbulence level and spectrum did not change with time and were

regular just a few seconds after tunnel start-up. Observation of the turbulence on the oscilloscope showed that there were no turbulent spots imbedded in the otherwise quiet flow. This was confirmed by streakline visualization in the freestream using the smoke-wire technique. Similarly, no irregularities such as of nonuniformities or unsteadiness were found in the mean flow, (Reynolds, 1979).

3.1.2 Pressure Gradient

The development of a Blasius boundary layer takes place under conditions of zero streamwise pressure gradient. As was mentioned in Chapter 2, the flat plate was mounted at a +0.25 degree angle of attack to make allowance for blockage effects. In this way, a slight area divergence was built into the test side of the plate to achieve zero pressure gradient. Since unavoidable pressure gradients existed at the leading edge, trailing edge, and past the traversing mechanism, the objective was to arrive as close as possible to zero pressure gradient over some test area of the plate.

Chordwise and spanwise pressure gradients were obtained for a range of chordwise traversing mechanism positions. The pressure levels from the 98 pressure ports were measured in a serial fashion via two Scanivalve pressure sampling valves (A.17) and a Setra Systems ±68.9 Pa differential pressure transducer (A.18). An example of these results for the suction model is shown in Figure 3.3 and Figure 3.4. In the chordwise case, the pressure drop past the traversing mechan-

ism, and the pressure rise at the trailing-edge flap were evident. Of particular importance was that the traverse extension arm positioned the hot-wire probe outside the local pressure gradient caused by the traverse mechanism. A nominal zero pressure gradient was obtained to within Cp = ± 0.20% in the chordwise direction and the spanwise direction.

The trailing-edge flap was adjusted to obtain an overall balance of blockage on the front and back sides of the plate. The flap adjustment resulted in an overall verticle shift in the Cp profile, but had very little effect on the pressure gradient. A simple calculation using Bernoulli's equation was employed to find the approximate mean pressure drop in the flow due to the presence of the plate. The trailing-edge flap was then adjusted to shift the Cp profile on the front of the plate to the desired level. Using this method, the flow was adjusted to the proper alignment with the leading edge and the blockage was balanced.

3.1.3 Transition Reynolds Number

With the zero pressure gradient established, the measurement of the transition Reynolds number, Rt, provided a direct indication of the overall flow quality. Two different methods were used to measure Rt, both employed a hot-wire anemometer to detect changes in the boundary-layer velocity profile.

The first method for measurement of Rt employed the traversing mechanism and the transition probe holder described in Chapter 2 and

shown in Figure 2.19. This probe holder positioned the hot wire at a constant Y-distance from the plate and allowed the traverse to move the probe in the X-direction. The freestream velocity was held constant and transition was determined from a plot of velocity vs Reynolds number at constant Y, as shown in Figure 3.5. Because of the transient nature of the transition process, multiple samples of the anemometer output were taken and averaged by the data acquisition system. Using this method transition was found to occur naturally at approximately Rt = 3.4×10^6. The actual transition location inferred from a given set of data could be determined in a number of ways, and the unsteady nature of the process left plenty of room for ambiguity. However, regardless of experimental method, the approximate location of transition was defined by fitting a straight line through each of the first two legs of the transition plot. The intersection of these two lines, as shown in Figure 3.5 then defined the transition Reynolds number.

The second method used a fixed hot-wire probe which was mounted rigidly on the surface of the flat plate, as discussed in Chapter 2 and shown in Figure 2.20. As the freestream velocity was increased, the onset of transition was defined as the sharp increase in the boundary-layer velocity. This procedure resulted in the data given in Figure 3.6. The beginning of the transition process from a laminar to a turbulent boundary layer occured at Rt = 3.5×10^6. In general, using either of the methods, transition due to the growth of natural laminar boundary-layer disturbances occured at Rt = 3.0×10^6 to 3.6×10^6.

The variations in Rt were generally due to different environmental conditions. These high values of Rt are comparable to values obtained at other low-turbulence wind tunnel facilities.

3.2 LINEAR STABILITY WITHOUT SUCTION

The spatial growth and decay of disturbances were measured in the boundary layer using the hot-wire anemometer. Disturbances were artificially introduced into the boundary layer by the vibrating ribbon which was discussed in Chapter 2. The objective of these measurements was to compare with the linearized theory, which assumes small disturbance amplitudes. Under these conditions, the Navier-Stokes equations reduce to the Orr-Sommerfeld equation. The disturbance behavior is then described by the solution of an eigenvalue problem. Characteristically, the behavior of the disturbance field is just the linear superposition of the behavior of each frequency component. The numerical solution of the Orr-Sommerfeld equation for the disturbance behavior as a function of Reynolds number and frequency is well known (e.g. Jordinson, 1970) and these results compare well with experiments in the moderate to high Reynolds number range (e.g. Saric & Nayfeh 1977;Wortmann 1955). Comparison of these results with the experiment described here provided verification of the basic flat plate experiment.

3.2.1 Effects of Traverse Position On The Flow Field

In spite of careful measurements of Cp and Rt it was obvious that the most sensitive diagnostic tool available for verification of the flow was the T-S wave behavior itself. A further check to determine if the local pressure gradient past the traversing mechanism was influencing the hot-wire measurement incorporated this fact. A hot-wire probe was located at a fixed position on the plate at a distance of 25 mm from mid-span of the plate. This probe was located at a Reynolds number such that disturbances at a non-dimensional frequency of F = 55 were locally amplified. The amplitude of the wave was then measured for various traversing mechanism positions. The objective was to determine if the disturbance amplitude was affected as the traverse moved forward to a position where the traverse mounted probe was at the same X-location as the fixed probe. The results showed no measurable effects due to the proximity of the traverse. Later, more detailed measurements confirmed that, indeed the traverse's local influence did not effect the hot-wire measurements, but that the traverse position influenced the overall blockage on the test side of the plate. This caused slight variations in the attachment line location at the leading edge, which resulted in slight changes in the pressure recovery in the leading-edge region. The effect of these variations was minimized by placing the vibrating ribbon aft, as far as possible from these regions where pressure variations existed. By so doing, the variations in the disturbance amplitude due to changes in the traverse position were reduced to ap-

proximately $\Delta|u'| = 5\%$, as shown in Figure 3.7. This depended of course on the frequency of the disturbance and the Reynolds number where the measurement was made. It must be kept in mind that these were variations in a disturbance whose amplitude was only 0.05% Ue to 0.07% Ue. The conclusion here was that traverse influence was small and could be reduced further only by mounting the traversing mechanism external to the flow.

3.2.2 Determination of Neutral Stability Points

Two-dimensional linear Tollmien-Schlichting waves propagating downstream in the boundary layer are known to have a behavior of decay and growth as a function of frequency and Reynolds number. A wave of a given frequency is amplified only within a certain range of Reynolds numbers, outside of which the wave decays. This behavior was illustrated in Figure 1.2. At the interface between these regions of growth and decay are locations of neutral stability, noted in Figure 1.2 by R_I and R_{II}. The locus of these points as a function of frequency forms the curve of neutral stability shown in Figure 1.3. It was the experimentally determined locations of neutral stability which served here as the primary source of comparison with previous experiment and theory.

The r.m.s. disturbance variation across the boundary layer, which characterizes a T-S wave was shown in Figure 1.1. The two-dimensional wave has u' and v' components parallel and normal to the plate res-

pectively. However, v' measurements were not possible due to the insensitivity of the hot-wire to this component of the flow. The u' disturbance amplitude has a 180 degree phase shift at approximately η = 4.0, but the |u'| profile is positive due to the r.m.s. nature of the measurement.

For a given freestream velocity, Ue, and a dimensionless frequency, F, the streamwise disturbance behavior was determined. Historically, various experimental methods have been used to measure the streamwise behavior of the disturbance amplitude, A(X) = |u'|/Ue. Schubauer & Skramstad (1947) measured the streamwise variation at a constant Y-distance from the plate, and Ross et al. (1970) kept the boundary-layer similarity variable, η , constant as they varied X. However, the nonparallel nature of the boundary layer and resulting variation of the disturbance profile shape with X cause errors in constant Y or constant η measurements which had to be corrected empirically. Saric & Nayfeh (1977) suggested that errors due to these nonparallel effects could be minimized by following the maximum of |u'| as the streamwise location was varied. This method which required searching for the maximum of |u'| at each streamwise station was more time consuming but inherently more precise. It was used by Kachanov et al. (1975), Strazisar & Reshotko (1978), and Saric & Reynolds (1980) and was used here to determine the growth and decay of boundary layer disturbances.

Disturbances were introduced into the boundary layer at a given frequency supplied by a sweep oscillator (A.7). The oscillator signal

was amplified by a power amplifier (A.10), which was adjusted to produce the desired disturbance amplitude. The r.m.s. disturbance amplitude in this experiment was plotted versus Y on the analog plotter. Linear stability measurements were performed with |u'| less than 0.1% of the freestream velocity, Ue. A detailed description of this instrumentation is given in Appendix A.

A typical disturbance frequency spectrum measured by the hot-wire anemometer for T-S waves introduced at F = 55 is shown in Figure 3.8. Spectra were plotted as the square root of the power spectrum so as to produce the r.m.s. disturbance spectrum. Corresponding to the measurement of Figure 3.8, the traversing mechanism extension arm vibration is shown in Figure 3.9. The vibrations relative to the flat plate were monitored by the inductive proximity probe mounted on the extension arm. From Figure 3.8 and 3.9 the vibrational contribution to the hot-wire signal was determined. These components of the hot-wire signal were therefore not hydrodynamic in nature, but contributed to noise in the measurement. The vibration spectra pointed out which T-S wave frequencies should be avoided, and which frequency bands would provide the best signal-to-noise ratio. The actual magnitude of the extension-arm vibration was determined by a digital voltmeter reading of the peak-to-peak a.c. voltage from the proximity-probe output. This amplitude was found to be approximately 0.05 mm at a freestream velocity of 15 m/s. These measurements indicate that the hot-wire probe vibration was very small, generally less than 1% of the boundary-layer thickness.

Vibration of this size had a negligible effect on the measurements of the disturbance amplitudes.

A narrow band-pass tracking filter facilitated measurement of only the disturbance introduced at the ribbon frequency. The tracking filter with a 1 Hz band width was tuned to the desired frequency using the same oscillator that drove the vibrating ribbon. The filter could also be switched out to pass the entire unfiltered disturbance signal. A measure of the r.m.s. disturbance amplitude was obtained using a DISA 55D35 r.m.s. unit (A.1). A qualitative evaluation was gained by monitoring the signal on a Tektronix 5113 oscilloscope (A.13). Using the oscilloscope, the filtered or unfiltered disturbance signal was compared with the ribbon input from the oscillator and the traverse vibration from the proximity probe. This was a valuable diagnostic tool for monitoring the different parameters influencing the measurements. A quantitative measure of these components was then obtained using the spectrum analyzer and data-acquisition system.

With the tracking filter in the filter mode, the r.m.s. disturbance profile near the maximum was determined by a series of measurements across the boundary layer. The plot of $|u'|$ vs Y on the analog X-Y plotter showed the position of $\max|u'|$. At this position, the disturbance amplitude was obtained using the r.m.s. meter or the spectrum analyzer. The output of the spectrum analyzer was in terms of the square root of the auto-spectrum, so that the r.m.s. of a particular frequency component was obtained directly. These measurements of

max|u'| were continued in the streamwise direction until a neutral point was found, i.e. d|u'|/dX=0. For decaying waves this corresponded to a minimum (Branch I point) and for amplified waves this corresponded to a maximum (Branch II point). The results of the measurements of max|u'| are shown in Figure 3.10. The Reynolds number at the neutral point was determined based on integration of the mean boundary-layer velocity profile and the assumption of a Blasius boundary layer. That is, with the assumption if a Blasius boundary layer, the reference length, δ_r was determined from the experimental value of the displacement thickness, δ^*,

$$\delta^* = \int_0^\infty (1 - \frac{u}{U_e})dY = 1.721\sqrt{\frac{\nu X}{U_e}} = 1.721\ \delta_r$$

The Reynolds number based on the reference length then resulted,

$$R = \frac{U_e \delta_r}{\nu} = \left(\frac{U_e X}{\nu}\right)^{1/2}$$

Determination of the neutral stability points based on measurements at max|u'| show very good agreement with the theory as well as with the experimental data of previous investigators. The scatter in the various experimental data at the higher frequencies was evidence of the greater nonparallel effects there as well as the difficulty in finding d|u'|/dX = 0 of these weakly amplified waves.

3.3 NONLINEAR STABILITY WITHOUT SUCTION

The pioneering experiments of Klebanoff, Tidstrom, & Sargent (1962) showed that the breakdown of T-S waves is accompanied by the appearance of three-dimensionality and nonlinear behavior. Kachanov, Koslov, & Levchenko (1977) conducted a series of stability experiments that showed the behavior of a single, initially two-dimensional wave as transition was approached. They identified four distinct regions of different behavior of the components of the T-S wave and showed the importance of the interaction of the different spectral modes. They also observed that in addition to the higher harmonics of a fundamental wave, a subharmonic wave with one-half the frequency of the fundamental wave appeared downstream. Later Kachanov, Kozlov & Levchenko (1980) observed that the nonlinear development of waves in the transition region depended on the initial disturbances. Kachanov et al. (1980) introduced two T-S waves into the boundary layer on a flat plate by using two vibrating ribbons. They observed significant amplification of a T-S wave at the difference frequency. In an effort to predict the appearance of the subharmonic wave seen by Kachanov et al. (1977), Nayfeh & Bozatli (1979) proposed a parametric resonance model for the excitation of the subharmonic wave. They showed however that an unusually high amplitude was required for this mechanism to be operative.

The present experiments investigated the behavior of two T-S waves in a Blasius boundary layer when the waves displayed weak nonlinear behavior. The initial amplitudes and the two-dimensionality of the two

disturbances were carefully controlled and their subsequent growth and interaction were observed.

3.3.1 Description of The Experiment

These experiments were motivated by the need for information leading to an understanding of the evolution of nonlinearly interacting T-S waves before the occurance of transition. When conditions exist for large amplification of a difference-frequency component, it is possible to have transition caused by the nonlinear interaction of two waves that, by themselves, would not lead to transition. Thus certain types of high frequency disturbances can generate the highly amplified, low-frequency disturbances that lead to transition.

The objectives of these experiments were first to add to the results of Kachanov et al. (1977,1980), second to provide appropriate initial conditions for comparison with the analytical models of Nayfeh & Bozatli (1979,1980), and third to examine the role of the initial amplitudes in the excitation of the difference harmonic.

These experiments were conducted with the same physical configuration as described previously. The tunnel was operated at a freestream speed of 6.7 m/s, and two-frequency disturbances were introduced into the flat plate boundary layer using a single vibrating ribbon. The streamwise behavior of these waves was determined by hot-wire measurements at the maximum of the disturbance profile. Measurements of the initially two-dimensional disturbances were conducted at midspan of the flat plate using the two-dimensional traversing mechanism.

The vibrating ribbon was located a distance X = 48.3 cm from the leading edge and it vibrated over a span of 35 cm. In order to study the nonlinear interactions of T-S waves, the ribbon was excited by two frequencies simultaneously. An additional signal generator was added to the vibrating ribbon system by means of a specially designed signal mixer. A schematic of the signal mixer is shown in Figure 3.11.

Since the initial conditions for the nonlinear wave interaction were crucial, it was necessary to understand the ribbon behavior. The frequency response of the ribbon was determined using the sting-mounted proximity probe directly over the ribbon. Plots of amplitude vs. frequency were obtained at several input voltages and these resembled those of a linear oscillator except that the natural frequency was amplitude dependent, as shown in Figure 3.12. The reduction in natural frequency observed for larger ribbon amplitude is due to a combination of the presence of pressure drag on the vibrating ribbon (which gave rise to a first-order damping term of the form $c\dot{x}|\dot{x}|$) and the slight increase in the temperature of the ribbon.

Frequency spectra of typical oscillator outputs showed the presence of harmonics on the order of 1% of the fundamental. Since the ribbon excitation was generally in the frequency range of 10 Hz to 100 Hz, the harmonic of this excitation was near the natural frequency of the ribbon. Therefore, fourth-order low-pass filters were used to minimize the unwanted harmonics to a level well below 0.1% of the fundamental. Even with this precaution, the ribbon did amplify the harmonics and

difference harmonics to some extent. The instrumentation configured to drive the ribbon and monitor its response is shown in Figure 3.13. This arrangement was essentially a two-channel configuration of the previous single-frequency experiments.

The signal processing for this experiment is flow charted in Figure 3.14, which shows the two-channel arrangement needed to isolate the two fundamental-frequency components of the signal. The two-frequency waves introduced into the boundary layer were at the nondimensional frequencies F_1 and F_2, where for all tests $F_1 = 105$ or in dimensional terms, $f_1 = 55$ Hz. Since multiple frequency disturbances were being measured, it was advantageous to use the HP 5420A digital signal analyzer to process the anemometer output. This was especially true since the r.m.s. amplitude of each frequency component was available through one measurement. Spectra of the boundary-layer disturbances were obtained with the hot wire located at a distance from the plate corresponding to the maximum r.m.s. amplitude of the $F_1 = 105$ component. This component of the signal was isolated using the tracking filter tuned to F_1. For all of the spectra, a 128 Hz band width was used with a $\Delta f = 0.25$ Hz for the high-resolution auto spectrum. Frequent checks were made outside this band to insure that nothing was being missed.

The Reynolds-number range over which measurements were obtained was chosen so that the fundamental frequency component, F_1, was crossing Branch II of the neutral stability curve. Numerous tests were then conducted at various values of F_2. Thus a large amount of data was

accumulated describing the behavior of F_1 and its harmonic $2F_1$. These results will be discussed next. The subharmonic excitation and amplification will then be considered. Lastly, data is presented for three types of interactions which produced the difference frequency amplification.

3.3.2 Harmonic Interaction

The data for F_1 and $2F_1$, accumulated from nine separate tests with two different amplitude ranges is shown in Figure 3.15. This figure shows first the consistency of the measurements throughout the test series. The most striking feature was the behavior of the component $2F_1 = 210$, which the linear theory predicted to be strongly damped in this range of Reynolds numbers. Figure 3.15 shows that the behavior of $2F_1$ was strongly coupled to that of F_1 even for disturbance levels as low as $|u'| \cong 0.1\%Ue$.

Based on the measurements of Figure 3.15, consistent values of the growth rates for F_1 and $2F_1$ were determined, and are shown in Figures 3.16 and 3.17. Growth rates were calculated using the central difference formula shown below, keeping in mind the usual scatter in this calculation.

$$\sigma = \frac{1}{|u'|}\frac{d|u'|}{dX} \simeq \frac{|u'(R+\Delta R)| - |u'(R-\Delta R)|}{4\Delta R|u'(R)|}$$

The growth rate of F_1 was found to follow closely that predicted by linear theory, while the $2F_1$ component displayed a growth rate $\sigma \cong 2\sigma_{F_1}$, agreeing closely with that predicted by Nayfeh & Bozatli (1980). Thus the $2F_1$ component behaved like the square of the F_1 component and any initial amplitude of the $2F_1$ component directly behind the ribbon decayed to zero before the measurement.

3.3.3 Subharmonic Interactions

The behavior of the $F_1/2$ component was monitored during all the experiments involving single as well as multiple frequency disturbances from the ribbon. These large amplitude T-S waves were followed to transition and at no time was the subharmonic component observed to appear. Nonlinear interaction involving the subharmonic wave was observed by introducing the fundamental and the subharmonic, $F_1/2$, with the vibrating ribbon. Generation of the harmonics $3F_1/2$ etc. were then observed when the subharmonic was present at 0.08%Ue, however this interaction disappeared when only the fundamental, F_1, was introduced. These interactions were believed to be of the type discussed in the previous section.

3.3.4 Three and Four-Wave Interactions

The generation and subsequent behavior of the different frequencies, $F_1 - F_2$ and $2F_1 - F_2$, is of special interest in the measurement of nonlinear T-S waves and their effects on transition. It is through this

type of interaction that a highly amplified low frequency wave may be created from two fundamental waves which would otherwise decay before transition occured. To investigate the dependence of these interactions on the initial conditions, three test cases were considered. Each of the three cases involved a different choice of the second fundamental frequency, F_2, whereas F_1 was always set to 105. The three test cases were performed between R = 550 and R = 850, and are shown superposed on the neutral stability curve for linear waves in Figure 3.18.

In Figure 3.18 the solid curve represents the nonparallel theory and the dashed line shows the parallel theory. Each of the three test cases were also performed at two disturbance amplitude ranges. The high and low amplitude ranges were determined by adjusting the ribbon input voltage so that the desired initial amplitude of F_1 was obtained at R = 550. The ribbon was located at approximately R = 450 and the first measurements were taken at R = 495. The two inputs to the signal mixer were maintained at the same voltage level. Tests were also conducted with the relative magnitudes of the F_1 and F_2 components different by the ratios of 2:1 and 1:2. The qualitative nature of the results remained the same and they are not reported here.

For test case I, disturbances were introduced at F_2 = 170, producing a difference frequency which according to linear theory, is amplified through the range of Reynolds numbers observed. The behavior observed is shown in Figure 3.19. The measurements shown are taken at the position of the profile maximum of the component at F_1. Other

components at $2F_1 - 2F_2$, $F_1 - 2F_2$, etc. were also measured and documented but, for clarity, are not shown in the figure. If ϵ is a small dimensionless parameter characterizing the disturbance amplitude, the component at $F_1 - F_2$ appears in the amplitude equations at $O(\epsilon^2)$ due to a quadratic interaction. The component at $2F_1 - F_2$ appears at $O(\epsilon^3)$ due to a cubic interaction. However, in the experiment these components are observed to appear at amplitudes of the same order of magnitude.

For test case II, disturbances were introduced at $F_1 = 105$ and $F_2 = 143$, thus generating a difference frequency which linear theory predicts will decay and then grow. The results of this test are shown in Figure 3.20. As with case I, an interchange of amplitude between the fundamental F_1 and the difference frequencies was observed.

Spanwise measurements were also taken at the high-amplitude range setting to determine the two-dimensionality of the initial disturbances at $R = 550$. These measurements were taken for $Z/\delta_r \pm 20$ with steps of $\Delta Z/\delta_r = 0.5$. The initial disturbances were found to be two-dimensional. Using a somewhat coarser step size, spanwise measurements were obtained over the entire ribbon span. This too showed the disturbances to be two-dimensional, except for a decrease in disturbance amplitude near the fixed ends of the ribbon. The same measurements were repeated at $R = 675$ and an increased spanwise variation was observed, indicating the generation of three-dimensional waves.

The two spectra in Figure 3.21, from the high-amplitude case II, are typical of the behavior observed just before the breakdown to broadband excitation. Between R = 675 and R = 725 significant three dimensionality occured in the disturbance motion. While the exact structure of this three dimensionality could not be measured with the single hot-wire probe, the disturbance spectra in this region were obtained by ensemble averaging. This showed that the three-dimensional behavior was accompanied by the presence of a low-frequency component at 5 Hz as well as 5 Hz difference peaks around the major components. These points are labeled with an s. These additional peaks continued to grow until the entire spectrum consisted of peaks, all of the same order-of-magnitude, separated by 5 Hz. Behavior of this type was reported by Kachanov et al. (1980). Referring to Figure 3.21, a portion of this effect may be attributed to a difference-frequency interaction between (b) & (c) and (g) & (h) or due to components at $3F_1$ - $2F_2$ and $4F_1$ - $2F_2$. However these types of interactions are necessarily very small in this Reynolds-number range. A strong dependence of the difference-frequency behavior on initial amplitude was observed when each case was repeated at a lower initial disturbance level. Under these conditions the nonlinear interaction of the difference-frequency components is almost absent, as shown in Figure 3.22.

A third test case was considered, this time introducing F_2 at a lower frequency than F_1. The interactions observed here were qualitatively the same as those seen in the previous high amplitude cases, except

that the component $F_1 - 2F_2$ now appears with $F_1 - F_2$. Results obtained in this test case are displayed in Figure 3.23.

3.4 LINEAR STABILITY WITH SUCTION

3.4.1 Description Of The Experiment

As stated earlier, the objective of these experiments was to conduct detailed mean-low and disturbance measurements in the boundary layer under different discrete suction strip configurations and suction intensities. These results would then provide modeling information and/or verification of theories to predict and optimize suction effects. In particular, the investigation included: (1) detailed mean-flow measurements to find the extent and nature of upstream and downstream suction influence, (2) discrete suction-strip configurations compared with continuous suction, and (3) certain strip configurations shifted in Reynolds number to investigate and optimize suction location. The experimental results were then compared with the recent theory of Reed & Nayfeh (1981). Ultimately these results should indicate important controlling parameters and trends for investigation of the more complex three-dimensional flows.

These experiments were conducted on the flat-plate suction model described in Chapter 2. Suction was provided via two porous Dynapore suction panels which were located in two of the four available positions on the flat-plate model. Referring to Figure 2.3, the suction-panels were placed in locations #1 and #2 for these experiments. Using these

porous panels, suction could be applied either continuously over two 24 cm chordwise lengths by opening all 15 of the available strips on each panel, or for discrete suction, seven strips on each panel were established. The available strips were chosen in an alternating pattern starting with the central strip on each panel. This provided the possible suction-strip locations shown in Figure 3.24.

As described in Chapter 2, the suction flow rate through the set of two panels was kept constant by a sonic choking nozzle which controlled the total volume flow rate into the evacuated plenum tank. In these tests, the choking-nozzle throat diameter was 2.54 mm, which allowed a 60.5 liters/min flow from the panels. This provided a possible range of suction velocities of v_0 = 0.02% Ue for spacially continuous suction to v_0 = 0.55% Ue for suction through a single suction strip. The available suction flow was divided proportionally between the panels, depending on the number of porous strips opened on each panel.

In establishing appropriate test conditions for the experiments, a number of factors were considered. While suction may have dramatic effects at the low Reynolds number side of the stability curve, in particular with regard to the critical Reynolds number it was recognized that high-frequency, low-Reynolds number measurements did not have practical importance. Therefore the experiments were conducted at the relatively low nondimensional frequencies, F = 20 and F = 25, where $F = 2\pi\nu f/Ue^2 \times 10^6$. Disturbances in this frequency range exhibit growth over a range of Reynolds numbers from approximately R_I = 900 to R_{II} =

2,300. For the seven test cases considered, suction was distributed in this region of growth as shown in Figure 3.25. In these tests, the single frequency waves were introduced by the vibrating ribbon at X = 120 cm. The measurements at F = 25 were conducted at two unit Reynolds numbers, where the unit Reynolds number was defined as Ru = $\sqrt{Ue/\nu}$. This resulted in an effective shift in the suction locations relative to the neutral stability curve.

The mean-flow and disturbance measurements resulting from these experiments are discussed in the last two sections of this chapter. In these measurements, the hot wire was traversed using the two-dimensional traversing mechanism which was operated automatically in the Y-direction. Mean-flow and disturbance measurements were conducted across the boundary layer with and without suction. A typical measurement is shown in Figure 3.26, where the mean velocity, u, the disturbance velocity, $|u'|$, and the relative phase, ϕ, were measured simultaneously. The measurement at each point here consisted of the average of eight samples. In addition, the disturbance frequency spectra were obtained for each of the profiles. A flow chart showing the arrangement of electronics used to obtain these measurements is shown in Figure 3.27, where the major change from previous experiments was automatic control of the Y-traverse motion.

3.4.2 Verification Of Spanwise Suction Uniformity

The spanwise uniformity of the suction velocity on the model was examined in order to verify the two-dimensionality of the suction flow. One of the primary considerations in the design of the suction system was to provide uniform and steady suction flow from the model. These measurements were then a test of the whole operating system; the suction delivery piping and manifolds, the overall porous-panel construction, and of course, the Dynapore material itself.

Because the two-dimensional traversing mechanism did not provide spanwise movement, the spanwise suction uniformity was measured using two fixed probes of the type shown in Figure 2.20. The fixed probe was located in the boundary layer downstream of porous panel #1 and near the maximum of the disturbance profile shape, at approximately η = 1. The stationary probes were placed at four spanwise locations over the range Z = ±7.5 cm where Z = 0 was the midspan of the plate. Mean-flow and disturbance measurements were then obtained with and without suction at the various spanwise locations. These results were then inspected with regard to uniformity of the suction influence over the span of positions considered.

Disturbances were introduced at a nondimensional frequency F = 25 by the vibrating ribbon. The tunnel was operated at a mean-flow velocity corresponding to a unit Reynolds number of Ru = 961. This placed the probes at R = 1409 and the midchord of porous panel #1 at R = 1339, both in the region of amplification for F = 25. Porous panel #1

was operated with all the suction strips opened so that continuous suction was provided over a chordwise length of 24 cm. The suction velocity at the wall was v_0 = 0.02%Ue.

The results of the mean-flow measurements are shown in Figure 3.28. The feature of importance in this figure was the change in velocity due to suction at each spanwise location. The variations in the absolute magnitude of the mean velocity were due to slight changes in probe height at each of the spanwise locations. An average change in the mean velocity of $\overline{\Delta u}$ = 0.011 Ue was observed and the standard deviation of this measurement was $(\overline{\Delta u} - \Delta u)$ = 0.003Ue.

The results of the disturbance measurements are shown in Figure 3.29. Again we see variations in disturbance amplitude due to slight changes in probe height, as well as due to spanwise variations in ribbon amplitude. From the plot we see that the disturbance amplitude was approximately 1% Ue without suction. Compared to the other stability experiments described here, these amplitudes were unusually high, and the corresponding higher ribbon amplitudes may have exhibited a greater spanwise variation than usual. However the changes in the disturbance amplitude at each spanwise location due to suction were indicative of the degree of suction uniformity. The average change in disturbance amplitude due to suction over the range of spanwise measurements was $\overline{\Delta|u'|}$ = 0.328% Ue and the standard deviation was $\overline{\Delta(|u'| - |u'|)}$ = 0.032% Ue.

3.4.3 Mean-Flow Measurements

The streamwise behavior of the mean velocity was measured in terms of the displacement thickness, δ^*, and the momentum thickness, θ, defined as,

$$\delta^* = \int_0^\infty (1 - \frac{u}{U_e})dY \qquad \theta = \int_0^\infty \frac{u}{U_e}(1 - \frac{u}{U_e})dY$$

Measurements of the boundary-layer mean velocity profile were integrated using the trapezoidal rule. Because of the nature of the δ^* and θ integrations, the most critical factor in this calculation was the accurate location of the plate surface relative to the hot wire, that is the coordinate Y for $u(Y_0) = 0$. Very slight errors in the determination of Y contribute significantly to errors in δ^* and θ. This was especially critical since changes in the displacement thickness due to suction were very small, usually less than 0.1 mm. Therefore efforts were made to determine Y_0 as accurately as possible.

Measurements were obtained in the boundary layer down to approximately u/Ue = 0.05, at which point the Y-traverse position was set to approximately zero volts, as shown in Figure 3.30. The data were then shifted in the Y-direction appropriately so that u = 0 at Y = 0. The location of the wall was found by extrapolation of the mean velocity profile. This was carried out independently for the profiles with suction and without suction. Various methods were used to obtain a reliable curve fit of the velocity profiles near the wall. These methods were

based on an assumed fourth order polynomial form for the velocity profile in terms of the similarity variable $\eta = y/\delta_r$. Upon substitution of this into the Blasius equation,

$$f''' + \tfrac{1}{2}ff'' = 0$$

where $f' = u/Ue$, and subject to the boundary conditions at the wall,

$$u(0) = 0,\ u''(0) = 0,\ \text{and}\ u'''(0) = 0$$

the form of the polynomial was found to be,

$$u = a\eta^4 + b\eta + c.$$

The constant, c, was included to accomodate the raw data profiles with $u \neq 0$ at $Y = 0$. As a first approximation to this, a linear curve fit was tried. However, this was found to be more sensitive to data scatter than the fourth order polynomial which could include data over a wider range of η. Therefore a fourth-order least-squares fit was used to extrapolate the velocity profile to the wall. Application of the curve-fitting routine to the Blasius solution showed that the fit could include points out to $\eta = 1.25$ without detrimental effects to the fit near the wall. This is shown in Figure 3.31 for the Blasius profile. The amount of shift to be applied to the experimental data was determined by solving for the zero of the approximating polynomial near the wall using Newton iteration. The least-squares curve fit was then reapplied to the shifted data, and this process was repeated until the required shift was less than 0.001 mm.

The effects of suction on the mean boundary-layer flow were expressed in terms of the shape factor, $H = \delta^*/\theta$. The application of the extrapolation scheme to the Blasius solution yielded the established shape factor for a Blasius boundary layer, $H = 2.59$. A typical mean-velocity profile measurement is shown superposed on the Blasius profile in Figure 3.32. This comparison showed good qualitative agreement between the measurement and the theory, and in addition found $H = 2.53$. In the experiment, the shape factor was generally in the range $H = 2.53 \pm .03$, somewhat lower than the Blasius case, suggesting the possibility of a very slight negative pressure gradient.

With the precautions mentioned above, the effects of suction on the mean flow could be observed when suction was applied through a single suction strip. As outlined in Figure 3.33, a number of tests were conducted with the one suction strip configuration. In these cases the suction velocities were high enough, approximately 0.5% Ue, to produce changes in the boundary-layer flow which could be resolved with the methods just described.

In test case III, listed in Figure 3.33, suction was applied through a single 1.59 cm wide strip located at position #4 on panel #1 (Figure 3.24). Suction was supplied at a normal velocity at the wall of $v_0 = 0.57\%$ Ue. The wind-tunnel flow velocity was 15 m/s which resulted in a unit Reynolds number of $Ru = 961/m^{1/2}$. The response of the boundary layer in terms of the shape factor is shown in Figure 3.34. Here a maximum decrease in the shape factor of approximately 7% was ob-

served. This decrease in the shape factor corresponded to a more full appearance of the velocity profile when compared to the no suction case. This filling out of the velocity profile is similar to the effect of a negative or favorable pressure gradient, except in the case of suction there is a very slight change in the boundary-layer profile. This is shown in Figure 3.35 for the region of maximum influence at R = 1375. To be noted from Figure 3.34 is that the region of maximum influence, that is the position of minimum H, occured downstream approximately 15δ from the suction strip. A quite significant influence was observed upstream of the suction strip, in this case approximately 20δ upstream. On the other hand, the boundary layer recovered rather quickly to the Blasius profile. In test-case III as well as the other single-strip test cases, the boundary layer recovered to within 1% of the no suction shape factor by 65δ downstream of the suction strip.

For suction through one or two suction strips, the changes in the mean flow were small but well defined as observed in Figure 3.34. However when suction was distributed through a larger number of strips the changes in the mean flow, measured in terms of δ^*, θ, or H, were so small as to be within the scatter of the data.

3.4.4 Disturbance Behavior

The behavior of linearly growing T-S waves under the influence of suction will be described here. Since traversing the hot wire in the Y-direction across the boundary layer was controlled automatically by

the data-acquisition system, it became feasible to obtain complete profiles of the disturbance amplitude at each streamwise station. With the tedium of such measurements handled by the computer, it was then possible to obtain much more detailed information of the disturbance amplitude and phase distribution in the boundary layer. Because of this capability, the disturbance amplitude at a given streamwise station was expressed in terms of the integral of $|u'|$ across the boundary layer. This integration was carried out only to the point of phase reversal since by continuity this area must equal the area above the point of phase reversal. As a result, only one-half the total area was tabulated. Integration of the profile provided a more complete evaluation of the disturbance amplitude for a number of reasons. The nonparallel effects in the boundary layer did not lead to the errors possible with a single point measurement. In addition, the experimental errors inherent in a single-point measurement were reduced by integration of the disturbance profile. Finally, profile integration allowed profile shape changes due to suction to be included in the measurement.

The experimental results obtained with various suction configurations were compared with the recent theory of Reed & Nayfeh (1981). The theory involves the use of a three-layer, or triple-deck model of the boundary-layer flow with suction strips. The resulting linearized equations used the dimensionless suction level at each strip as the small parameter. Closed-form solutions describing the boundary-layer flow were then obtained. The solutions consisted of a mean flow, Blasius

flow, and linearly superposed corrections due to each strip. Upstream influence was accounted for in this theory. Using the linearized triple-deck closed-form solutions for the streamwise velocity components, stability calculations were performed to obtain the disturbance behavior. A suction optimization scheme was also proposed and this will be compared with experimental results.

In all the plots of the streamwise disturbance amplitude behavior, the amplitudes have been normalized to the initial or lowest Reynolds-number measurement. In all cases, the initial disturbance amplitude at the maximum of the disturbance profile (near $\eta = 1$) was $|u'| \cong 0.05\%$ Ue. The particulars concerning the experimental setup and electronics were described at the beginning of this chapter and remain the same in the data described here.

A number of experiments were conducted with discrete suction through one suction strip as shown in Figure 3.33. In these cases, each suction strip was isolated allowing its influence to be observed without influence from other suction strips. In addition, the relatively high suction velocities in these cases allowed a clearer definition of the effects.

The mean-flow behavior for the single-suction strip configuration of test case III was discussed in the preceeding section, and the corresponding disturbance behavior is shown in Figure 3.36. Good agreement exists with the Blasius theory for the data taken without suction, a trait common in all the data. In this test case, suction through the

single strip of v = 0.57% Ue was intense enough to stop the disturbance growth and cause decay over a region beginning ahead of the suction strip and extending approximately twenty boundary-layer thicknesses downstream of the suction strip. The theory predicted, in this case, a slightly greater downstream influence than the disturbance actually displayed. Of particular interest is that the theory predicted the upstream influence rather closely. The extent of upstream and downstream suction influence displayed by the disturbance data correlated well with the range of influence displayed by the mean-flow data.

The various single suction strip configurations also provided information concerning the effect of suction placement. Test cases I and II, again listed in Figure 3.33, are considered in this regard. These tests were conducted at a slightly higher unit Reynolds number, Ru = 987, than the test described previously. Disturbances were introduced at a nondimensional frequency of F = 20 by the vibrating ribbon. The results of test case II, for which the suction intensity and dimensional location remained the same as for case III, is shown in Figure 3.37. The resulting data are also qualitatively the same as that of test case III. In addition, some variation in the disturbance amplitude near the suction strip was evident in the no-suction case. These variations were evident to a lesser degree when the data were plotted in terms of the maximum of the $|u'|$ profile. This suggested that the slight variations in the integrated $|u'|$ profile were evidence of profile distortion near the suction strip without suction. This behavior was only evident in

the single suction-strip cases I and II. For test case I all of the experimental conditions remained the same except that suction was provided through a single porous strip located on panel II at position #4. This downstream shift of the suction location moved the suction nearer to the location of maximum growth rate predicted by linear theory. The suction-panel locations for cases I and II are shown relative to the neutral stability curve in Figure 3.25. The results of test case I are plotted in Figure 3.38. As with case II and III the suction influence in case I extended approximately 20 δ upstream. In case I, observation of the downstream influence was difficult because of the limited extent of downstream measurements. However, the downstream influence does seem to be slightly less than that observed in case II. This might be expected due to the higher local growth rates in case I.

Comparison of the results of cases I and II reveals a very similar behavior despite the large change in the local Reynolds number. The maximum local reduction in the disturbance amplitude in these two cases is roughly the same. However, a more complete understanding of the relative merit of these two cases must consider the final disturbance amplitude at some downstream location, given an initial amplitude at one upstream initial position common to both cases. To accomplish this, results of test case I were renormalized so that the Blasius curves coincided. Now the results of the two test cases based on disturbances originating from the same point may be observed, and this is shown in Figure 3.39. Here the differences in the two cases are evident; the

advantage of providing early suction is obvious. Further consideration concerning optimization of suction placement will be discussed in the description of test cases V and VI.

The effect of multiple suction-strip configurations was studied in test cases IV through VII. In the first of these, case IV, suction was applied through six suction strips; three on panel #1 at positions #1, #4, and #7, and three on panel #2 at the same positions. As with all the tests, the volume flow rate remained constant, providing in this case, suction velocities of approximately v_0 = 0.1% Ue. The resulting disturbance behavior is shown in Figure 3.40. A much reduced upstream influence was observed ahead of the leading suction strips, with theory and experiment agreeing very well over panel #1. The agreement was not as good however downstream of panel #1 where the theory predicted a slightly greater downstream influence.

The number of suction strips were increased again in test case V where seven strips were opened on panel #1 and the same three strips on panel #2 remained opened. The porous strips on panel #1 were located at positions #1 through #7. The resulting suction velocities were then v_0 = 0.042% Ue on panel #1 and v_0 = 0.11% on panel #2. In this case the flow rate was still equally divided between panels #1 and #2, as it was for test IV. As can be seen in Figure 3.41, the results changed only slightly from the six strip case. There was almost no change in the theoretical prediction, but the slightly lower disturbance amplitudes measured after panel #1 brought the theory and experiment

into closer agreement in that region. The disturbance amplitude immediately downstream of panel #2 in the 7/3 configuration was reduced by approximately 20% from the corresponding amplitude in the 3/3 suction configuration.

Test case VII considered continuous suction on both panels. All fifteen suction strips were opened on both panels, and the resulting suction velocity was v_0 = .02% Ue. Otherwise the experiment remained the same, and the results which followed are shown in Figure 3.42. The same general behavior was found in this case as was found in the previous multiple suction strip configurations. Again the theory changed very little from the previous suction cases. The disturbance amplitudes immediatly downstream of panel #2 in this case lie between the corresponding amplitudes for the 3/3 and 7/3 configurations.

Superposing the results of test cases III, IV, V, and VII allowed the distinguishing features of each to be observed, and this is shown in Figure 3.43. Though the character varied in each of the test cases, the resultant amplitude in the most downstream measurement varied no more than 20% from that of test case III. In each of the three multiple strip configurations, including continuous suction, the suction flow was divided equally between panels #1 and #2, where in case III the suction flow was concentrated through one strip on panel #1.

The optimization scheme proposed by Reed & Nayfeh (1981) suggested the preferrable location of suction strips for a given suction mass flow rate. The scheme minimized the total growth, $n = \ln(A/A_0)$, of a

wave from Branch I to Branch II of the neutral stability curve. The results showed it to be preferrable to concentrate suction in the initial region of growth near Branch I, and not at the region where the wave is most highly amplified. It was also suggested that any remaining suction be placed in the amplified region near Branch II.

The optimization scheme was tested directly by repeating the experiment V at the same dimensionless frequency, and the same suction mass flow rate, but at a reduced unit Reynolds number, thereby moving suction toward Branch I. These two experiments are shown relative to the neutral stability curve in Figure 3.25. The results of the lower Reynolds number test are shown in Figure 3.44, where again the disturbance amplitudes have been normalized as before.

Comparison of Figures 3.41 and 3.44 show a definite difference in character, but about the same total growth. However if the high Reynolds-number test results are renormalized to bring the Blasius (without suction) curves in alignment, a very dramatic difference is observed, and this is shown in Figure 3.45. The effective Reynolds number shift in the suction strip locations is shown on the horizontal axes of the figure. Agreement between theory and experiment is quite good here, with theory accurately predicting the 55% reduction in disturbance amplitude from the aft suction case to the forward suction case found in the experiment.

Chapter IV

CONCLUSIONS

4.1 LINEAR DISTURBANCES

Experiments to investigate laminar boundary-layer stability and the effects of laminar flow control have been developed at V.P.I. & S.U. This program was initiated with the investigation of the linear stability of the Blasius boundary layer. These initial experiments on a flat-plate model served to develop the experimental apparatus and measurement techniques for the later experimental programs. The later programs included the experiments on nonlinear two- and three-wave interactions in the boundary layer, and studies of laminar flow control using boundary-layer suction.

The experiments were performed in the V.P.I. & S.U. Stability Wind Tunnel, which is normally used for aerodynamic loading and stability experiments. It was therefore necessary to establish the feasibility of conducting boundary layer stability experiments in this facility. This investigation showed the facility to be very suitable for boundary-layer stability measurements. With some care in maintaining clean turbulence-damping screens, the freestream turbulence levels were consistently found to be very low and were comparable with other facilities used for this type of work. Measurements to determine the flow uniformity and steadiness in the freestream and in the boundary layer revealed no un-

usual or undesirable features in the flow. Flow visualization using smoke streak lines from a smoke-wire apparatus confirmed these measurements visually. Confirmation of the wind-tunnel flow quality was provided by a determination of the transition Reynolds number, which was found to be $Rt = 3.4 \times 10^6$. These characteristics of the flow allowed the observation of T-S waves, which were introduced in a controlled fashion, to be observed with and without suction up to X-Reynolds numbers of 2.7×10^6.

Two flat-plate models were developed to facilitate boundary-layer experiments with and without suction. The models were equipped with the necessary measuring devices to provide accurate diagnostic information in the form of static-pressure measurements and flow visualization. An elliptical leading edge was fitted to the models which proved relatively insensitive to leading-edge separation, and at the same time minimized the pressure rise in the leading edge region. The resulting laminar boundary layer was very uniform across the span of the plate.

A two-dimensional traversing mechanism was developed based on stepping motor drives and this mechanism provided accurate positioning of the hot-wire probe in the boundary layer along the midspan and normal to the plate. A three-dimensional traverse was also developed, but was used only to verify spanwise flow uniformity. This traverse was not ideally suited for chordwise flat-plate measurements because of the possibility of undesirable upstream influence. However, the test-section configuration of the flat-plate experiment with the two-dimensional traverse was shown to exhibit zero pressure gradient and mea-

surements of the velocity profiles in the boundary layer indicated similarity with respect to the boundary-layer variable, . The local pressure gradient past the traverse was shown not to influence the measurements of the hot-wire probe mounted on the traverse extension arm. However, the overall flow blockage due to the traverse could not be avoided. The variations in this blockage as the traverse was moved fore and aft in the test section resulted in slight changes in the flow at the leading edge. It was suspected that slight changes in the local Reynolds number based on the displacement thickness occured as a result of pressure changes at the leading edge as the traverse moved. While the mean-flow effects were very small, the resulting errors in the disturbances, which were highly amplified, were a maximum of approximately 5% to 10%. The net effect of these errors was that disturbances measured at the higher X-distances, appeared to be 5% to 10% higher than they should be. In the following discussion, the effect of these errors on the results will be mentioned where necessary. The variations in blockage with traverse position could be balanced if an automatically varied trailing-edge flap deflection were possible. However this would be difficult to impliment and a much preferrable solution would be to mount the traversing mechanism external to the test section, with only the extension arm entering the flow. This option was not physically possible with the present test section.

The counter/controller developed for the traversing mechanism provided accurate and consistant indication of traverse position. Interfacing of the counter/controller with the data-acquisition system computer

provided the remaining link needed to obtain detailed measurements across the boundary layer in a reasonable amount of time. With a little more effort, the traverse could be fully interfaced to the data-acquisition system so that preprogrammed motion and data sampling could be coordinated in all traverse directions.

Tollmien-Schlichting waves were generated in the boundary layer by using a vibrating ribbon and the linear stability of these waves was investigated. Neutral stability points were found at several dimensionless frequencies and these agreed well with the linear theory.

4.2 NONLINEAR DISTURBANCES

In the nonlinear experiments, it was demonstrated that it is possible to excite one vibrating ribbon with two frequencies. In fact, for two frequency excitations a single vibrating ribbon was found to be desirable because discrete disturbances could be introduced at one location with relative ease. It was found that special care must be taken in the use of the vibrating ribbon, especially in the nonlinear experiments where larger ribbon displacements are likely to occur. Laboratory measurements of the spanwise variation in the ribbon vibration amplitude and phase insured the proper frequency and mode shape. Midspan measurements of ribbon motion during the wind-tunnel experiment guaranteed the correct frequency content.

Although predicted to be damped by linear theory, disturbances generated through nonlinear interaction at $2F_1$ were found to grow and decay as F_1 grows and decays, even for F_1 amplitudes of 0.1% Ue.

The growth rate of these T-S waves at $2F_1$ was found to be $\sigma \cong 2\sigma_{F_1}$ following that predicted by Nayfeh & Bozatli (1980).

Nonlinear interaction generating a subharmonic wave at $F_1/2$ was not found to be present up to transition, except when $F_1/2$ was introduced by the ribbon. The behavior observed when $F_1/2$ was introduced was the nonlinear behavior of F_1 and its harmonic, discussed in subsection 3.3.2 and Nayfeh & Bozatli (1980), and not the linear problem of Nayfeh & Bozatli, (1979).

The higher order interactions at $O(\epsilon^3)$ of $2F_1 - F_2$ were observed to be of the same magnitude as the three-wave interactions at $O(\epsilon^2)$ of $F_1 - F_2$. This behavior suggested that three-dimensionality was playing a role at this stage of the nonlinear development. Subsequent flow visualization showed that this was in fact the case (Weber et al. 1980). These higher order interactions were found to be very dependent on initial conditions.

As the disturbance amplitudes grew to be of the order of 1.0% Ue three-dimensionalities and multiple-frequency interactions appeared to dominate the breakdown process. These results are in substantial agreement with those of Kachanov et al. (1980) even though different quantities were measured.

4.3 LINEAR DISTURBANCES WITH SUCTION

Detailed mean-flow and disturbance measurements were conducted in the boundary layer over the flat-plate model with porous panels in order to assess the stabilizing effects of suction. Suction was provided at a constant mass flow rate through various suction-strip configurations, and in this way the relative merits if each were determined. Suction was maintained at a constant mass flow rate by the use of a sonic choking nozzle, which also had the desirable effect of greatly reducing the noise propagation through the suction system to the porous panels.

Suction flow through the surface of the model was made possible via suction panels which employed a woven stainless steel porous material called Dynapore. Measurements of the disturbance behavior over the Dynapore surface without suction showed a behavior agreeing closely in all cases with that expected for linearly growing waves. Therefore the Dynapore material and porous panels as a whole had no measureable effect on the stability behavior without suction. Furthermore, spanwise measurements with fixed probes showed the suction flow to be uniform in the spanwise direction.

Several experiments were conducted with suction through a single suction strip. Without the influence from other suction strips, these experiments showed details of the nature and extent of suction effects when suction is applied in a discrete fashion. Since suction was concentrated through a single strip in these tests, the local mean-flow effects in the boundary layer were of a size that they could be resolved.

The suction mean-flow effects were measured in terms of the shape factor $H = \delta^*/\theta$. For suction through a single porous strip with a suction velocity at the surface of v_0 = 0.57% Ue, the shape factor decreased by approximately 7%. This was found to occur about fifteen boundary-layer thicknesses downstream of the centerline of the porous strip. The upstream influence was quite significant, for example in this case the shape factor began to drop approximately twenty boundary-layer thicknesses ahead of the porous strip. The effects of suction on the mean flow were detected approximately sixty-five boundary-layer thicknesses downstream of the porous strip. These observations showed the overall range of suction influence and stress the importance of upstream effects in the theoretical developments.

In any practical application of suction, the use of continuous suction will probably not be feasible because of structural considerations. Therefore a number of discrete suction-strip configurations were tested and compared to continuous suction to determine which possible penalties, or benefits might be expected. In each case the experimental results were compared with the theoretical predictions of Reed & Nayfeh (1981). In the three multiple-strip suction configurations, the number of suction strips on each panel, denoted here by: (# strips opened on panel one) / (# strips opened on panel two), were: 3/3, 7/3, and 15/15, this last case being continuous suction over each panel. The general character of the disturbance behavior with suction was similar in each of the three multiple-strip configurations. Judging their overall

effectiveness in terms of the final disturbance amplitude leaving porous panel #2, the 7/3 configuration was found to be the most effective. In the 7/3 configuration the disturbance amplitude leaving panel #2 was reduced 20% from that of the 3/3 configuration. The continuous suction case was actually found to be slightly less effective than the 7/3 configuration. Fairly significant improvements were found however in going from the 3/3 configuration to the 7/3 configuration. Further comparison of the data showed that a 1/0 suction configuration was just as effective as the 3/3 configuration, but this raised the question of overall suction placement versus suction-strip spacing. For all of these cases the agreement between theory (Reed & Nayfeh, 1981) and the experimental results was very good. However, the theory suggested little difference in effectiveness between the three multiple suction-strip cases. The theory generally predicted the extent of downstream influence to be slightly greater than what the experiment showed. However there was general agreement within the bounds of the experimental error, considering there was a tendency for the total growth of the waves on the plate to appear 5% to 10% high because of traverse mechanism blockage effects.

The experimental and theoretical results showed that the choice of suction placement was much more important than obtaining optimum interstrip spacing. The optimization scheme developed by Reed & Nayfeh (1981) suggested that suction be concentrated not in the region of maximum growth rate, but further upstream in the weakly amplified region

near the Branch I neutral curve. The experimental results conducted to check this removed any doubt that in fact suction should optimally be placed near Branch I. Given that an upper ceiling is placed on the allowable suction velocity, the optimization scheme also suggested that any remaining suction flow not used near Branch I should be used in the region near Branch II. This was not checked in these experiments, and therefore remains to be verified.

The generally good agreement found here between experiment and the theory of Reed & Nayfeh (1981) provides some direction for further theory and experimental development. The theory is now capable of predicting suction effects and directing suction optimization for the flat-plate flow. With this as a foundation, the theory should be extended to three-dimensional geometries (Nayfeh & Reed, 1982). The results in the experiments described here suggest as well that further suction experiments be directed to the investigation of the three-dimensional flow. The first steps here may include experiments on the flat plate with pressure gradient and/or sweep. In addition, experiments may continue on the flat plate to investigate the effectiveness of new porous suction materials, especially the perforated titanium material which seems to be another viable surface material for the aircraft application.

REFERENCES

Bradshaw, P. 1965 The effect of wind tunnel screens on nominally two-dimensional boundary layers. J.Fluid Mech. 22, 679-688.

Corke, T., Koga, D., Drubka, R., and Nagib, H. 1974 A new technique for introducing controlled sheets of smoke streaklines in wind tunnels. Proc Int'l Cong. on Instr. in Aero. Sim. Fac. IEEE Pub. 77 CH 1251-8 , AES, 74-80.

Cousins, W. T., Saric, W. S., & Reynolds, G. A. 1978 Design of a three dimensional traverse mechanism for boundary layer stability studies. VPI & SU Rep. No. VPI-E-78-13.

Floryan, J. M., & Saric, W. S. 1980 Wavelength selection and total growth of Gortler vortices. AIAA Paper No. 80-1376.

Hahn, M. & Pfenninger, W., 1973 Prevention of transition over a backward step by suction, J. Aircraft 10, 618-622.

Jordinson, R., 1970 The flat plate boundary layer, Part 1. Numerical integration of the Orr-Sommerfeld equation, J. Fluid Mech. 43, 801-811.

Kachanov, Yu. S., Koslov, V. V., & Levchenko, V. Ya. 1975 Growth of small disturbances in a laminar boundary layer. (in Russian) Ucheniye Zapiski TSAGI 5, 137-140.

Kachanov, Yu. S., Kozlov, V. V., & Levchenko, V. Ya. 1977 Nonlinear development of waves in a boundary layer (in Russian) Mek. Zhid. i Gaza No. 3, 49-54.

Kachanov, Yu. S., Kozlov, V. V., & Levchenko, V. Ya. 1980 Experiments on nonlinear interaction of waves in a boundary layer. I.U.T.A.M. Symposium on Laminar-Turbulent Transition, Editors: R. Eppler, H. Fasel, Springer-Verlag, 135-144.

Klebanoff, P. S., Tidstrom, K. D., & Sargent, L. M. 1962 The three-dimensional nature of boundary-layer instability. J. Fluid Mech. 12, 1-34.

Kouvasznay, L.S.G., Komoda, H., & Vasudeva, B.R. 1962 Detailed flow field in transition. Proc. 1962 Heat Trans. & Fluid Mech. Inst. Stanford, 1-26.

Nayfeh, A. H. & Bozatli, A. N. 1979 Secondary instability in boundary-layer flows. Phys. Fluids 25, 805-813.

Nayfeh, A. H. & Bozatli, A. N. 1980 Nonlinear interaction of two waves in boundary layer flows. Phys. Fluids 23,448-458.

Nayfeh, A. H. & Reed, H. L. 1982 Stability of flow over axisymmetric bodies with porous suction strips. AIAA Paper No. 82-1025.

Pearce, W. E. 1978 Application of porous materials for laminar flow control. NASA CTOL Transport Technology Conference, Douglas Paper No. 6693.

Pfenninger, W., 1961 Boundary layer suction experiments with laminar flow at high Reynolds numbers in the inlet length of a tube by various suction methods, Boundary Layer and Flow Control, II. New York, Pergamon, pp. 961-980.

Pfenninger, W. & Groth, E., 1961 Low drag boundary layer suction experiments in flight on a wing glove of an F-94A airplane with suction through a large number of fine slots, Boundary Layer and Flow Control, Pergamon Press, pp. 981-999.

Pfenninger, W. 1977 USAF & Navy sponsored Northrop LFC research between 1949 and 1967. AGARD/VKI, Special Course On Concepts for Drag Reduction, Rhode-St-Genese, Belgium.

Prandtl, L., 1904 Fluid motion with very small friction. Proc. Third Intern. Math. Congress, Heidelberg, 484-491.

Reed, H. L., 1981 The Tollmien-Schlichting instability of laminar viscous flow. Ph.D. Dissertation, VPI & SU, Blacksburg, Virginia.

Reed, H. L. & Nayfeh, A. H., 1981 Stability of flow over plates with porous suction strips. AIAA Paper No. 81-1280.

Reynolds, G.A., 1979 Experiments on the stability of the Blasius boundary layer. M.S. Thesis, VPI & SU, Blacksburg, Virginia.

Reynolds, O. 1883 An experimental investigation of the circumstances which determine whether the motion of water shall be direct or sinous, and of the law of resistance in parallel channels. Phil. Trans. Roy. Soc. 174, 935-982.

Ross, J. A., Barns, F. H.,Burns, J. G., & Ross, M. A. S. 1970 The flat plate boundary layer, Part 3, Comparison of theory with experiment. J. Fluid Mech. 43, 819-832.

Saric, W. S. & Nayfeh, A. H. 1977 Nonparallel stability of boundary layers with pressure gradients and suction. AGARD Paper No. 6, Processing No. 224.

Saric, W. S., Weber, D. L., & Reynolds, G. A., 1979 Design and construction of a three-dimensional and two-dimensional traversing mechanism with a digital controller. VPI Report (in preparation).

Saric, W.S. and Reynolds, G.A. 1980 Experiments on the stability of nonlinear waves in a boundary layer. I.U.T.A.M. Symposium on Laminar-Turbulent Transition, Editors: R. Eppler, H. Fasel, Springer-Verlag, 125-134.

Saric, W.S., Reynolds, G.A., Weber, D.L., Konstadinopoulos,P., and Coctis, C.: 1982 Dynamic response of a vibrating ribbon for boundary-layer stability experiments, VPI & SU report no. VPI-E-79.29.

Schlichting, H. 1933 Zur Eutstehung der Turbulenz bei der Plattenstromung. Nachr. Wiss. Gottingen Math.-phys. Klasse, p. 181-208.

Schubauer, G. B. & Skramstad, H. K. 1947 Laminar boundary layer oscillations and transition on a flat plate. J. Res. Nat. Bur. Stand. 38, 251-292.

Strazisar, A. J. & Reshotko, E. 1978 Stability of heated laminar boundary layers in water with nonuniform surface temperature. Phys. of Fluids, 21, 727-735.

Tollmien, W. 1929 Uber die Entstehung der Turbulenz. Nachr. Ges. Wiss. Gottingen, Math.-phys. Klasse, 21-44.

Weber, D. L., Saric, W. S., Reynolds, G. A., Tice, G. L., & Woodbridge, R. D.
1980 Visualization of Tollmien-Schlichting waves. Bulletin of the American Physical Society 25, 1081.

Wortmann, F.X., 1955 Untersuchung instabiler Grenzschichtschwingungen in einem Wasserkanal mit der Tellurmethode, 50 Jahre Grenzschichtforchung, Braunschweig, F. Vieweg & Sohn, 460-470.

Appendix A

EQUIPMENT

A.1 HOT-WIRE ANEMOMETRY

Three independent anemometry channels were used. Each channel consisted of:

A.1.1 DISA 55D01 Constant Temperature Anemometer (CTA).

The anemometer was operated with a bridge ratio of 1:20, using a probe cable length of 5m. For high resolution measurement of low-level signals the hot wires and cables were balanced at a gain of 11 and operated at a gain of 7. The anemometer output voltage V was related to the air velocity U by: $V^2 = V_o^2 + BU$, where V , B, and n are functions of temperature.

A.1.2 DISA 55D10 Linearizer.

All anemometer outputs were processed through this unit to obtain a voltage signal which was linearly proportional to the velocity being measured. The unit was calibrated by inputing 1/n, obtained by a plot of Log U vs. Log $[(V/V_o)^2 - 1]$ from the anemometer. This procedure was handled through the data acquisition system.

A.1.3 DISA 55D35 RMS Voltmeter.

A true r.m.s. and squared r.m.s. was obtained in the range - 60 dB to + 50 dB over one volt. The integrator time constant was variable in the range 0.3 to 100 seconds.

A.2 HOT-WIRE PROBES

A.2.1 DISA 55P05 Boundary-Layer Probe

The sensor consisted of a 5 μm diameter Platinum-plated tungsten wire with an overall length of 3mm and a sensitive wire length of 1.25mm (L/D = 250). Sensor-support prong isolation was provided by a copper and gold plating at the wire ends to a diameter of approximately 30 μm.

A.2.2 DISA 55P71 Parallel Turbulence Probe

This was a two wire probe with parallel sensors. The probe sensors measured at essentially the same point and this allowed elimination of electronic noise from the two independent channels.

A.2.3 DISA 55A22 General Purpose Hot-Wire Probe.

This is the old style DISA probe and was used for fixed probe applications.

A.3 HP 3052 AUTOMATIC DATA ACQUISITION SYSTEM

This system provided high speed, 40 channel, data sampling capabilities in either the d.c. or r.m.s. mode. Data-processing capabilities are provided with output via paper tape, magnetic tape, or digital plotting. The system can also function as a controller through various means. The system consisted of:

A.3.1 HP 3455A High Accuracy/High Resolution DVM.

This is an integrating digital voltmeter which measures d.c. volts, a.c. volts (from 30Hz to 250 KHz), and resistance. It has 5 to 6 - digit accuracy. The voltmeter has auto-ranging capabilities for selection of the appropriate amplitude range.

A.3.2 HP 3495A Input Scanner.

The scanner switches analog input signals to an appropriate measuring device (voltmeter). It can also control external devices with relay actuator closures.

A.3.3 HP 9825A High Performance Calculator.

This desk top computer operates on HPL, a high-level, formula-oriented language. It serves as both a controller of external devices as well as a data processor with 24K bytes user read/write memory. The 9825A is the controller for the 3052.

A.3.4 HP98035A Real Time Clock

This unit provides real time referencing and time related control to the data acquisition system. The real time clock has six major functional groups: a clock circuit with rechargeable batteries, control circuitry, four timing/counting units, four input ports, four output ports, and an external interface cable. The timer has 1 sec resolution and the output ports provide logic level pulses of 4 sec duration.

A.3.5 HP 9872A Four-Pen Digital Plotter.

This is a microprocessor-based plotter which produces multicolor plots on any size chart up to 280 mm x 432 mm.

A.4 HP 5420A DIGITAL SIGNAL ANALYZER.

This is a two channel digital instrument which provides time and frequency domain analysis of analog signals in the range of dc to 25 kHz. Analog data is input through the HP 54410A analog/Digital Converter and anti- aliasing is provided by a HP 54470 Digital Filter.

A.5 ZONIC MULTICHANNEL FFT PROCESSOR.

A two channel spectrum analyzer, the Zonic provided high frequency analyzing capabilities up to 50 kHz.

A.6 HP 3960 INSTRUMENTATION TAPE RECORDER.

This unit is a portable, 4 channel, 3-speed tape recorder which used 6.35 mm magnetic tape. The recorder can be operated in either FM mode or direct-record mode. It was used in FM mode which provided a dc to 5 kHz frequency bandwidth.

A.7 SPECTRAL DYNAMICS SD104A-2 SWEEP OSCILLATOR.

A constant 1v amplitude wave from 0.02 Hz to 20 kHz, $\pm$ 0.2 dB was provided by this instrument. It was operated in the manual, constant frequency mode for these experiments but had linear and logarithmic frequency sweeping capabilities.

A.8 SD121 TRACKING FILTER

This tracking filter is a solid-state, frequency-fixed-bandwidth tracking filter. Fixed bandwidth of 1, 2, 5, 10, 20, 50, 100, and 200 Hz are available. The filter was operated with the 1 Hz bandwidth. A filtered signal output that is phase and amplitude coherent with the signal input at the tuning frequency, is provided.

A.9 SD110-1 PHASE METER

This instrument measures phase angle over a frequency range of 5 Hz to 1 MHz and dynamic range of 40 dB relative to 3 Vrms. The phase angle in degrees is continuously displayed on the front panel meter and is provided as a proportional d.c. voltage for recording purposes.

A.10 MC INTOSCH 100 AC POWER AMPLIFIER.

This unit provided a 100 watt output at 8 ohms to the vibrating ribbon. The frequency response was 10 Hz to 50 kHz, -0.5 dB at 100 watts.

A.11 SORENSEN NOBATRON DCR150-15A.

This was a dc power supply used to drive the electromagnets. It had a 15 amp maximum output.

A.12 STEPPING MOTOR CONTROL

A.12.1 SUPERIOR ELECTRIC ST103 TRANSLATOR

This stepping unit supplies the appropriate voltage switching sequence to drive the stepping motors. A number of modes for motor operation are available including: half-step/full-step, low-speed/ramp to high speed, and continuous run/single-step options.

A.12.2 SUPERIOR ELECTRIC SP153 INDEXER

The SP153 stepper has the same has the same capabilities as the ST103 and in addition allows preset selection of motor-step count. The preset number of motor steps is initiated either by a toggle switch on the panel front or by an externally supplied trigger pulse.

A.12.3 COUNTER/CONTROLLER

This unit was constructed to provide a control location for manual operation of both the ST103 and the SP153. Switching is provided for selection of the motor operation modes available with the ST103 and SP153. The counter portion of this unit receives the trigger pulses from the three motor stepping units and keeps a binary count of these pulses. The three pulse counts are displayed by binary LED display, as well as A-D converted for output to the data acquisition system as an indication of traverse position. These d.c. voltages are displayed by three panel-mounted digital volt meters.

A.12.4 CONTROLLER/TRAVERSE INTERFACE

This digital circuit was constructed to interface the HP 98035A clock to the SP153 indexer. The clock outputs a 4 sec pulse which the interface converts using a 555 timing chip, to a 15 msec pulse. This pulse is then recognized by the indexer and motor motion is initiated. When the motor motion is complete, a logic level 0 done signal is returned to the clock input via the interface circuit. Upon arrival of the done signal the clock timer is initiated so that a pre-programmed period elapses before data is taken. This is used as a precaution to avoid sampling data before the traverse vibration from the previous movement has decayed.

A.13 TEKTRONIX MODEL 5113 OSCILLOSCOPE.

This is an 8-channel scope with 2-channel storage capabilities.

A.14 HP 5300A/5302A FREQUENCY COUNTER.

This counter provided frequency measurements with a resolution of 0.1 Hz. for a ten second sample period.

A.15 BRUEL & KJAER 2427 AUTORANGING DIGITAL VOLTMETER.

This voltmeter provided a true r.m.s., average, or peak reading for input signals in the range 0.5 Hz to 500 kHz.

A.16 BENTLY NEVADA SERIES 190 PROXIMITOR PROBE.

This is an inductance type probe which has a linear measuring range of 0 - 1.1 mm with a nominal output of 0.0 to 14 vdc. The frequency response was d.c. to 10 kHz, ± 1%.

A.17 SCANIVALVE MODEL D.

This solinoid operated mechanism allowed serial sampling of 48 pressure inputs. The selected pressure input was then available for pressure transducer measurement.

A.18 SETRA SYSTEMS MODEL 239E DIFFERENTIAL PRESSURE TRANSDUCER.

This was a ± 0.01 psid transducer which provided a linear dc output of ± 2.5 volts.

A.19 J-TEC VF-563D GASEOUS FLOWMETER

This flowmeter measures the volumetric flow rate by means of vortex sensing. Vortices shed from a small strut inside the flow tube are detected by an ultrasonic beam directed across the tube. This provides a frequency output which varies linearly with flow rate over the range 7 to 280 liters/min. Linearity is 3% of full scale. The output pulse rate is 16 Hz-min/liter.

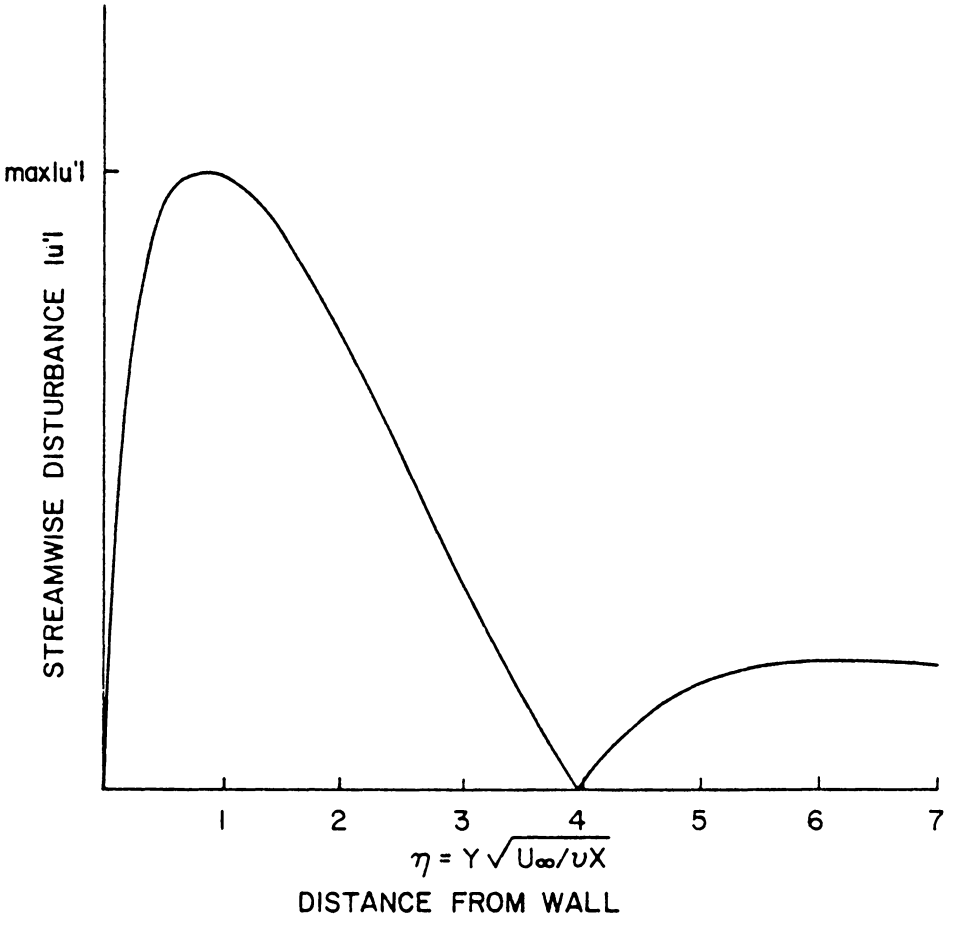

Figure 1.1 Solution of linear theory for the case of F = 25, R = 1376.

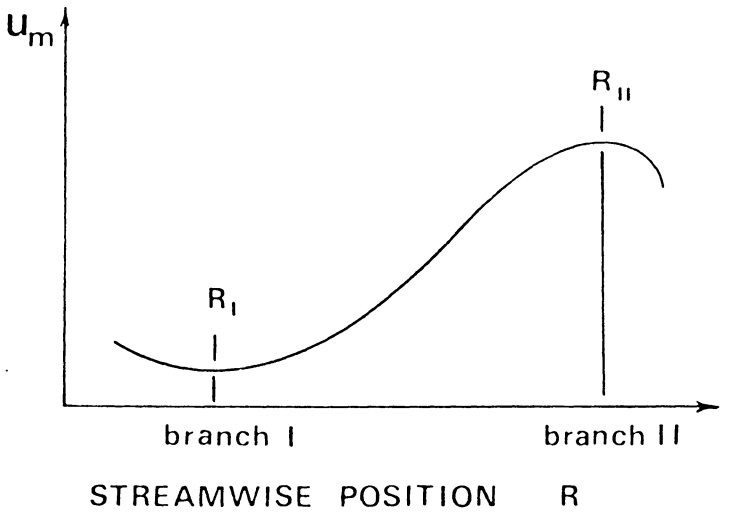

Figure 1.2 Representation of typical growth behavior expected for Tollmien-Schlichting waves. Neutral stability points are at R_I and R_{II} .

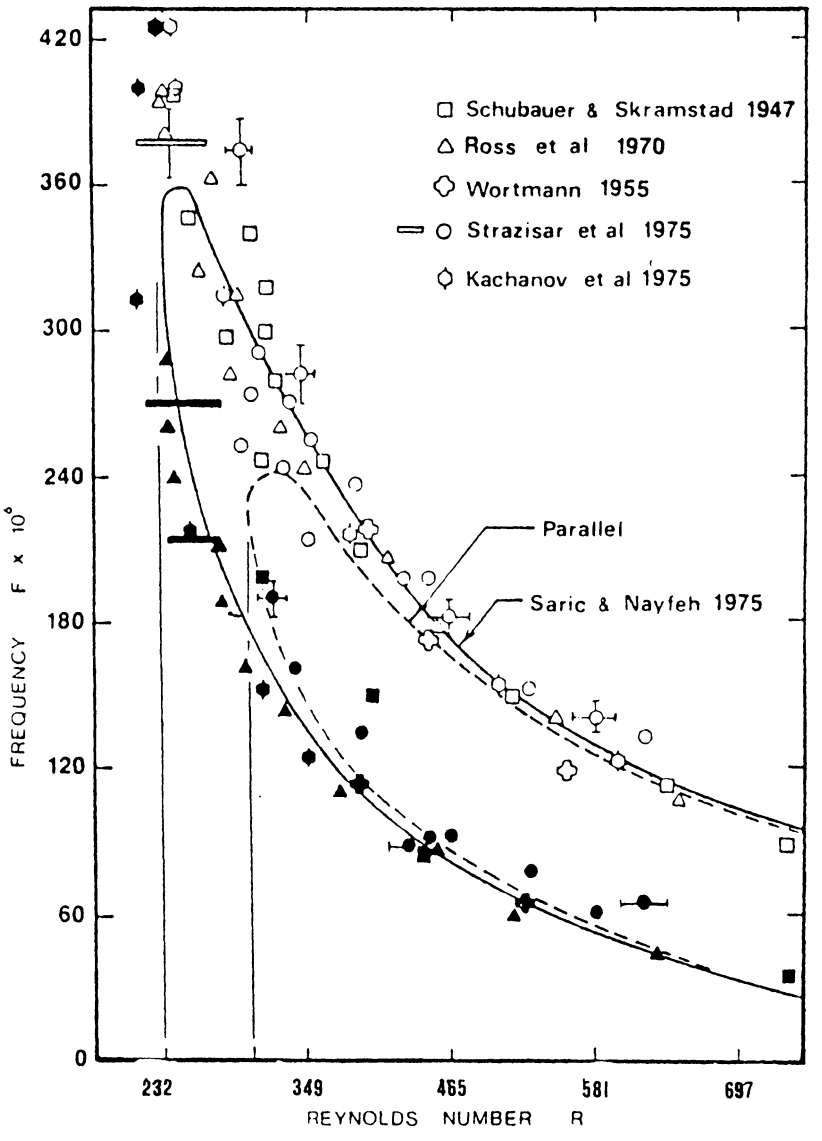

Figure 1.3 Neutral stability curve for Blasius boundary layer. Solid symbols are Branch I experimental points. Open symbols are Branch II. The critical Reynolds number based on the reference-length is 233 for nonparallel calculations, 302 for parallel calculations.

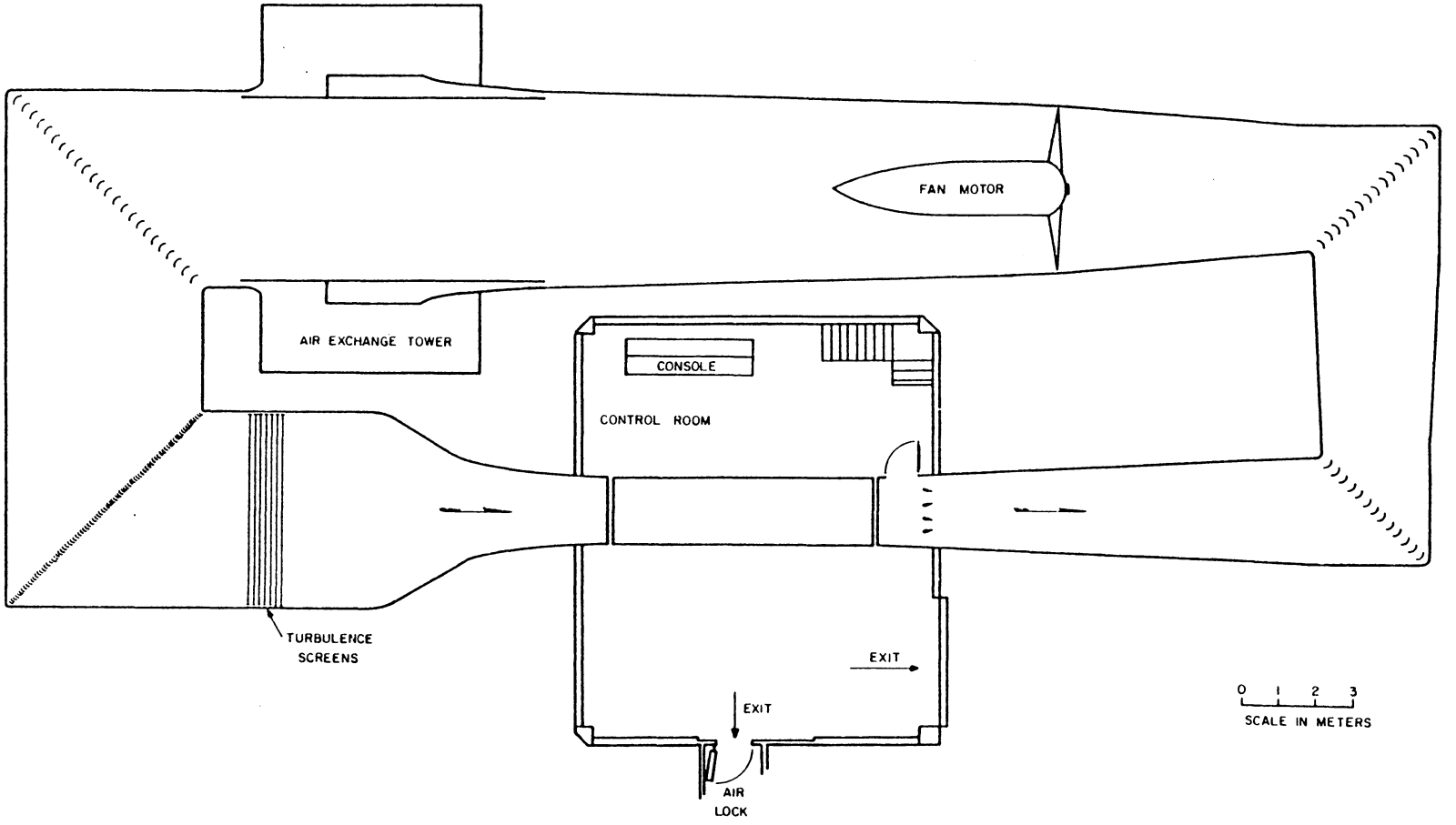

Figure 2.1 Cut-away view of V.P.I. & S.U. Stability Wind Tunnel showing turning vanes, turbulence screens, control room, and test section.

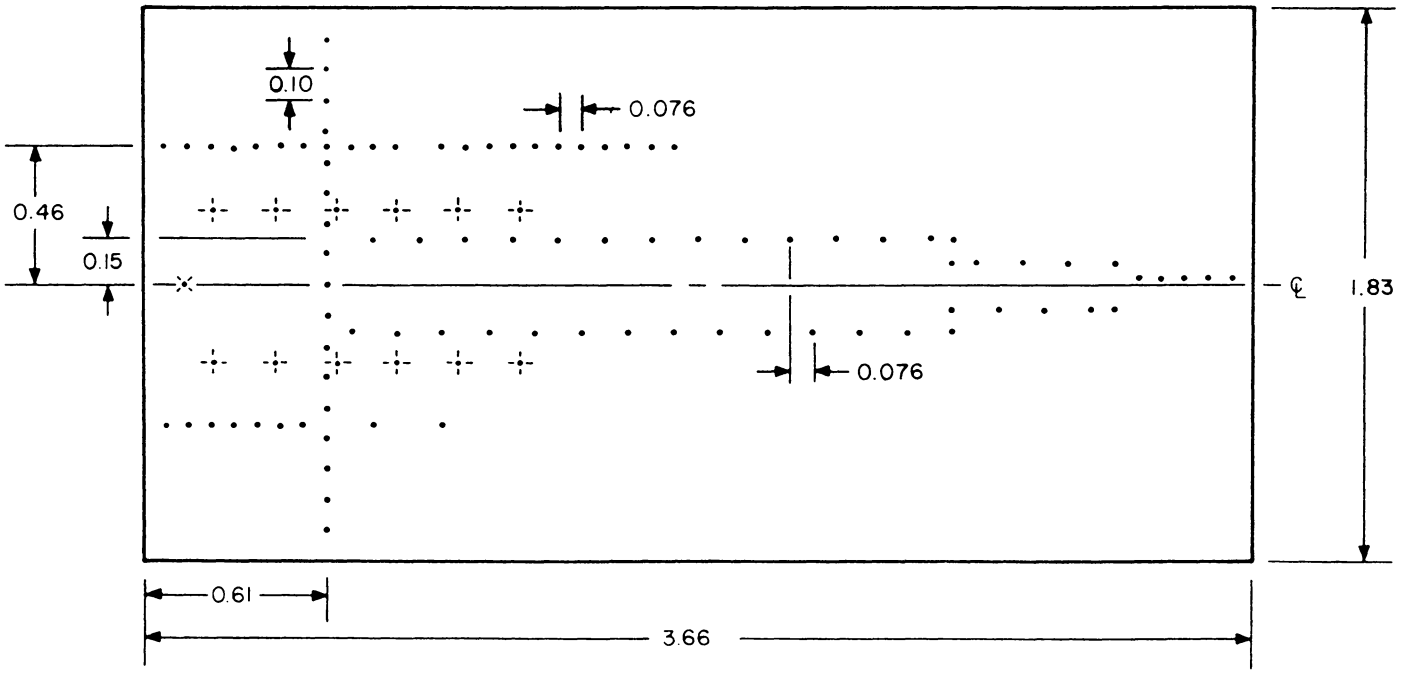

Figure 2.2 Flat plate model without suction, showing pressure ports • , smoke-wire locations -⊹- , and proximity probe location ✕ .

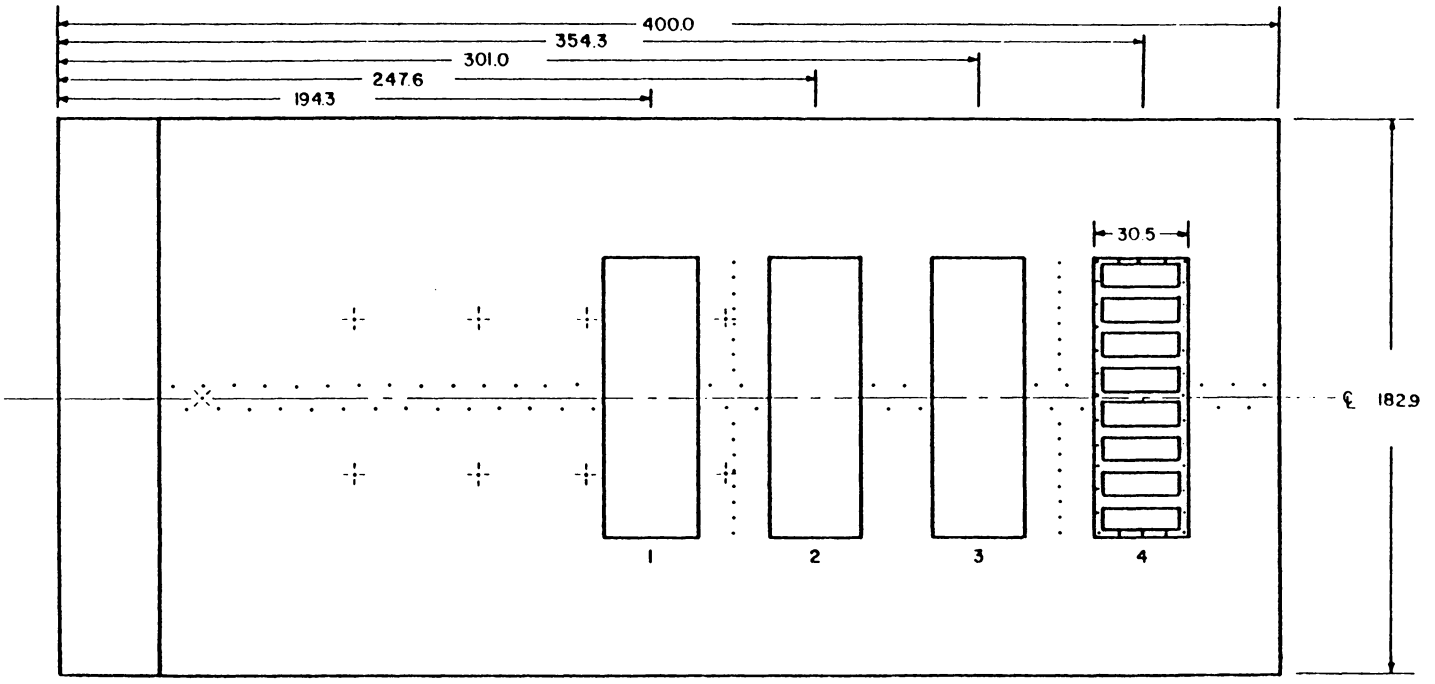

Figure 2.3 Flat-plate suction model showing porous panel locations as well as pressure ports • , inductance probe ✕ , and smoke wire locations ⊹ .

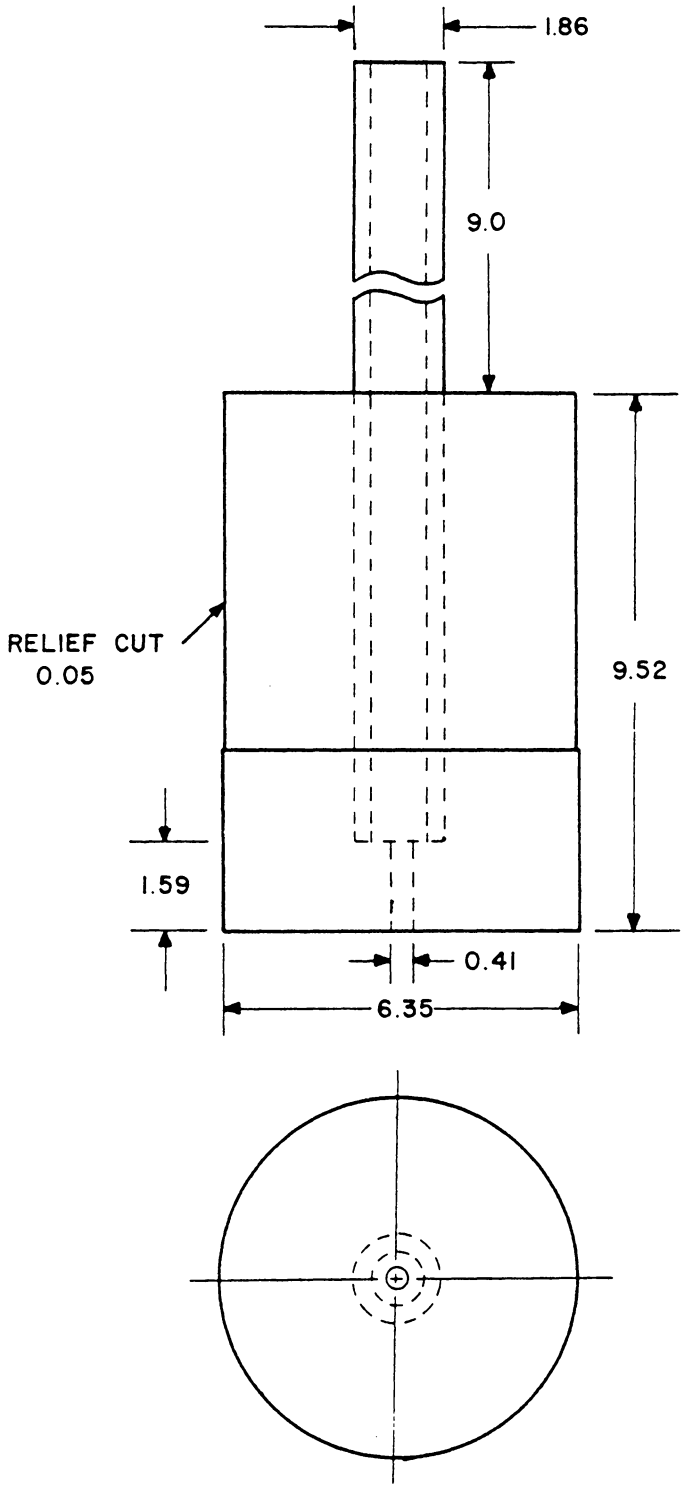

Figure 2.4 Static-pressure-port insert. All dimensions given in millimeters.

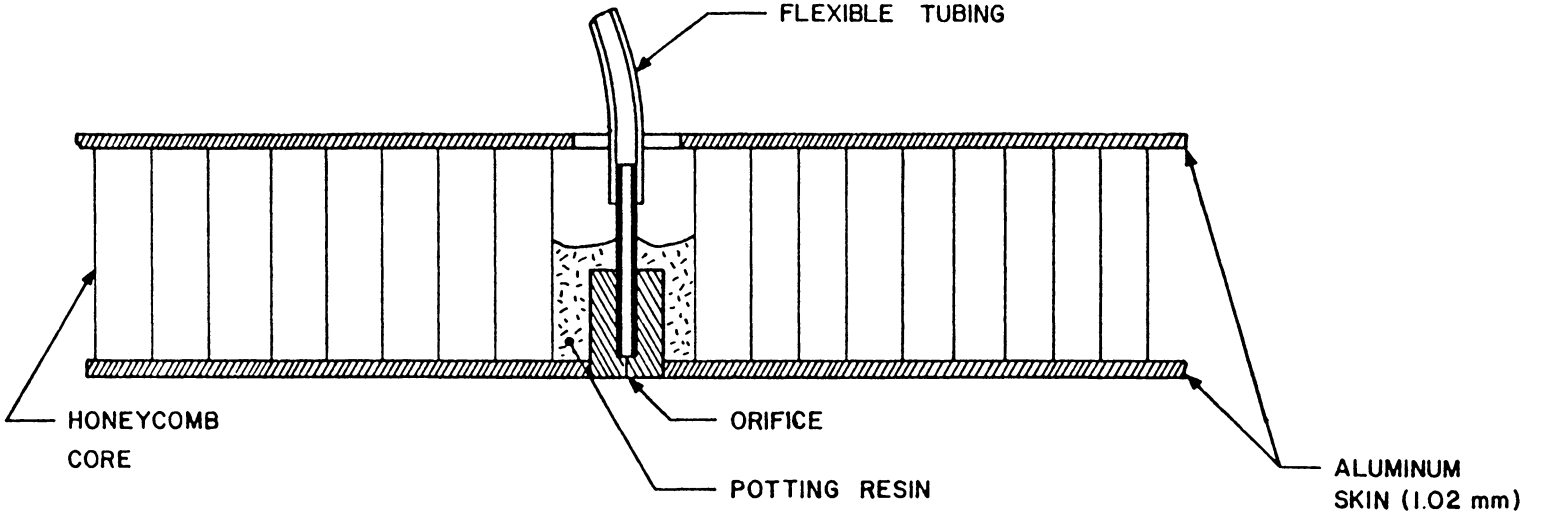

Figure 2.5 Static-pressure-port assembly and plate cross section.

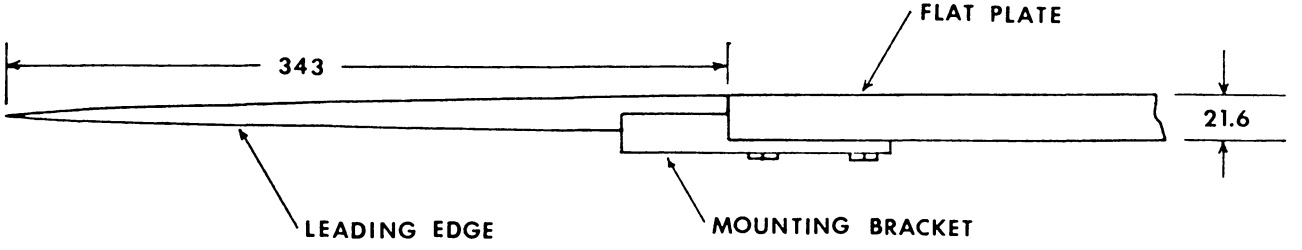

Figure 2.6 Leading edge/flat plate junction. All dimensions are given in millimeters.

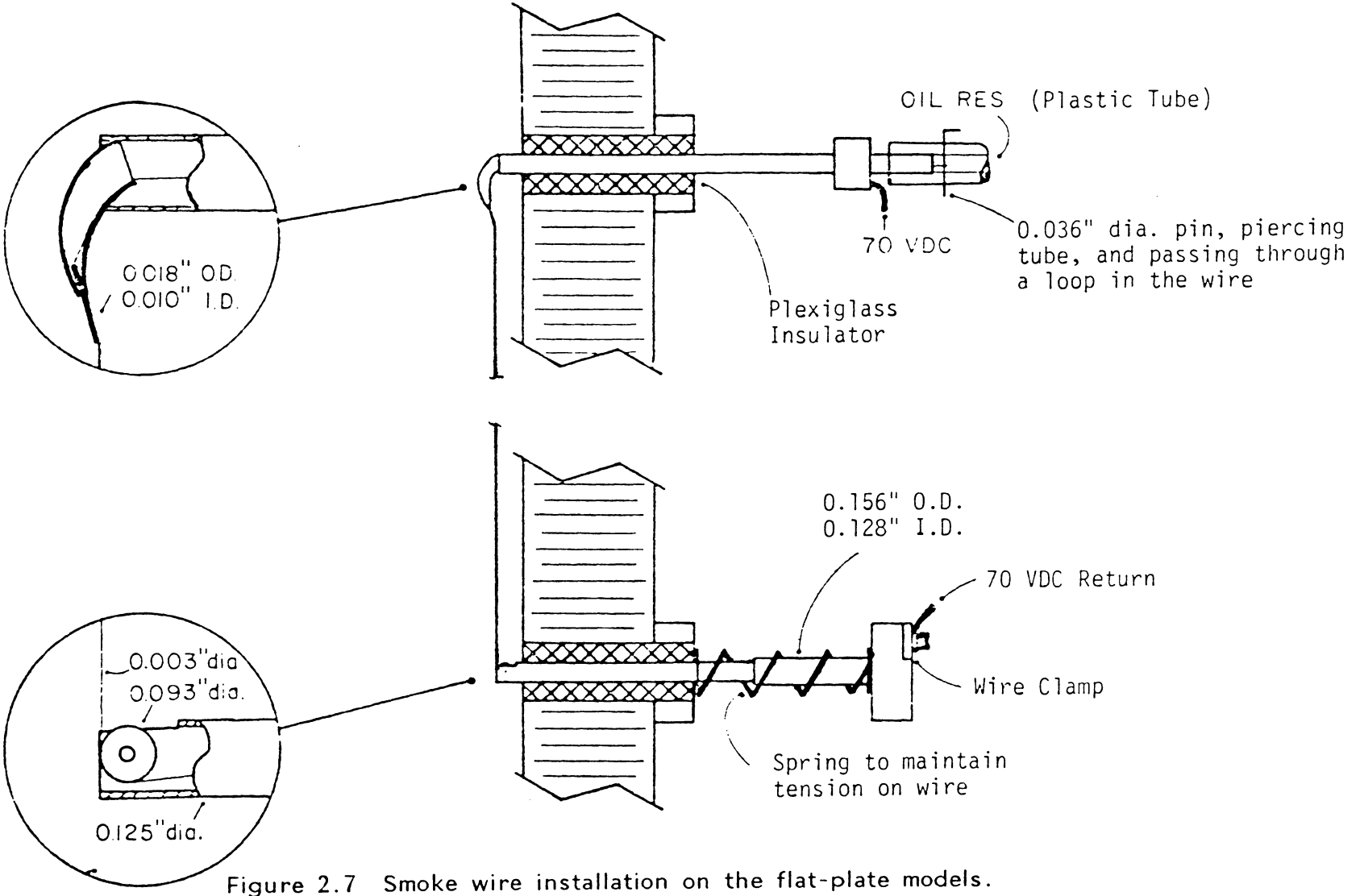

Figure 2.7 Smoke wire installation on the flat-plate models.
Span: 51 cm.
Wire: 0.076 mm (#40 AWG) stainless steel.

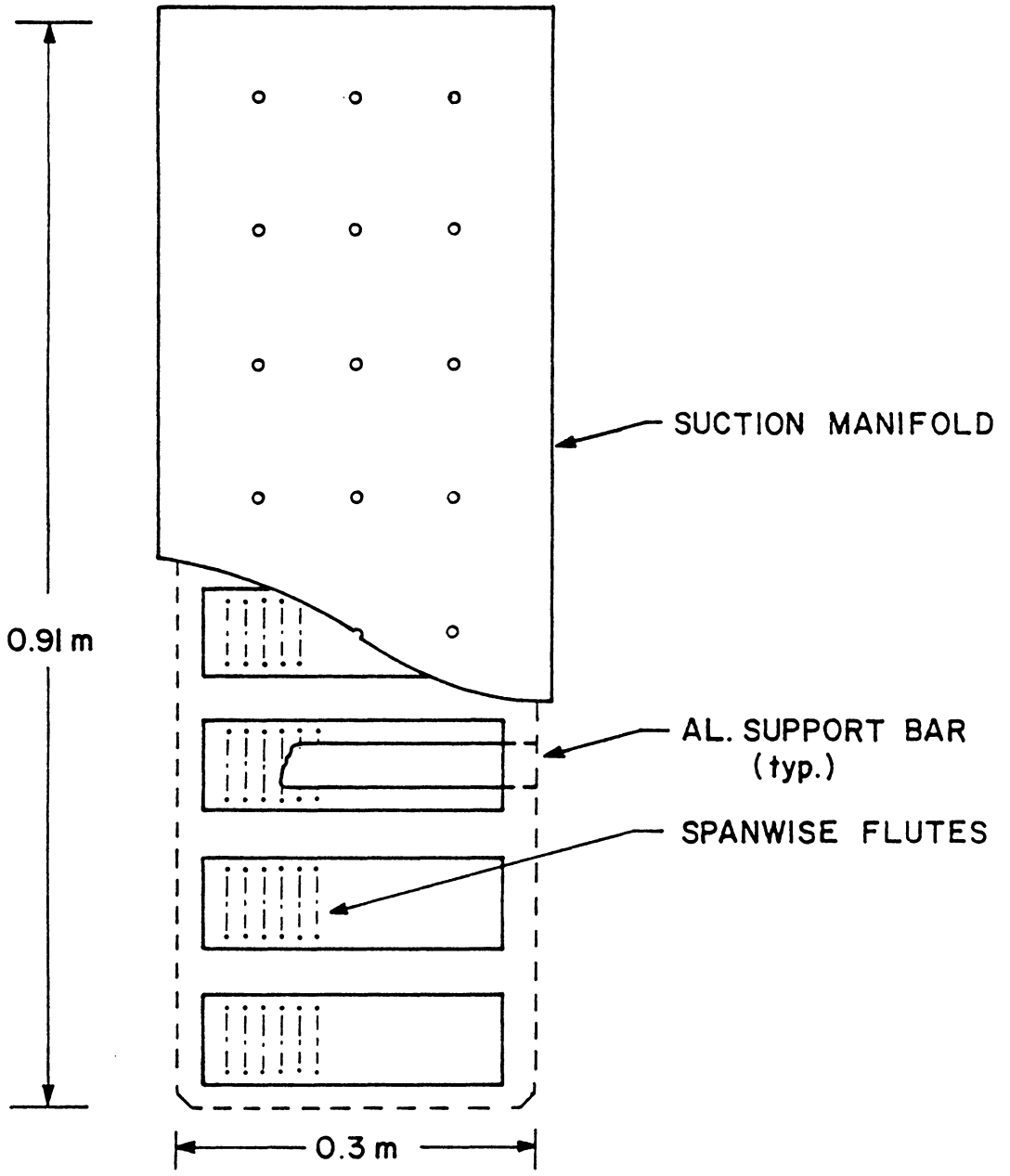

Figure 2.8 Cut-away view of porous panel installed in the model.

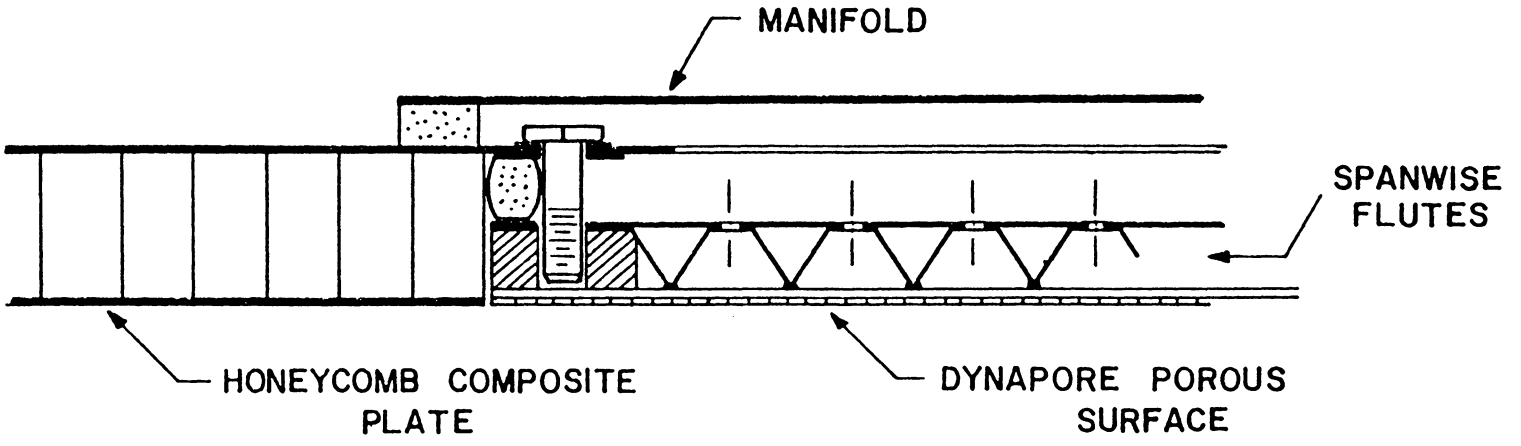

Figure 2.9 Cross section of porous-panel construction and assembly in the model.

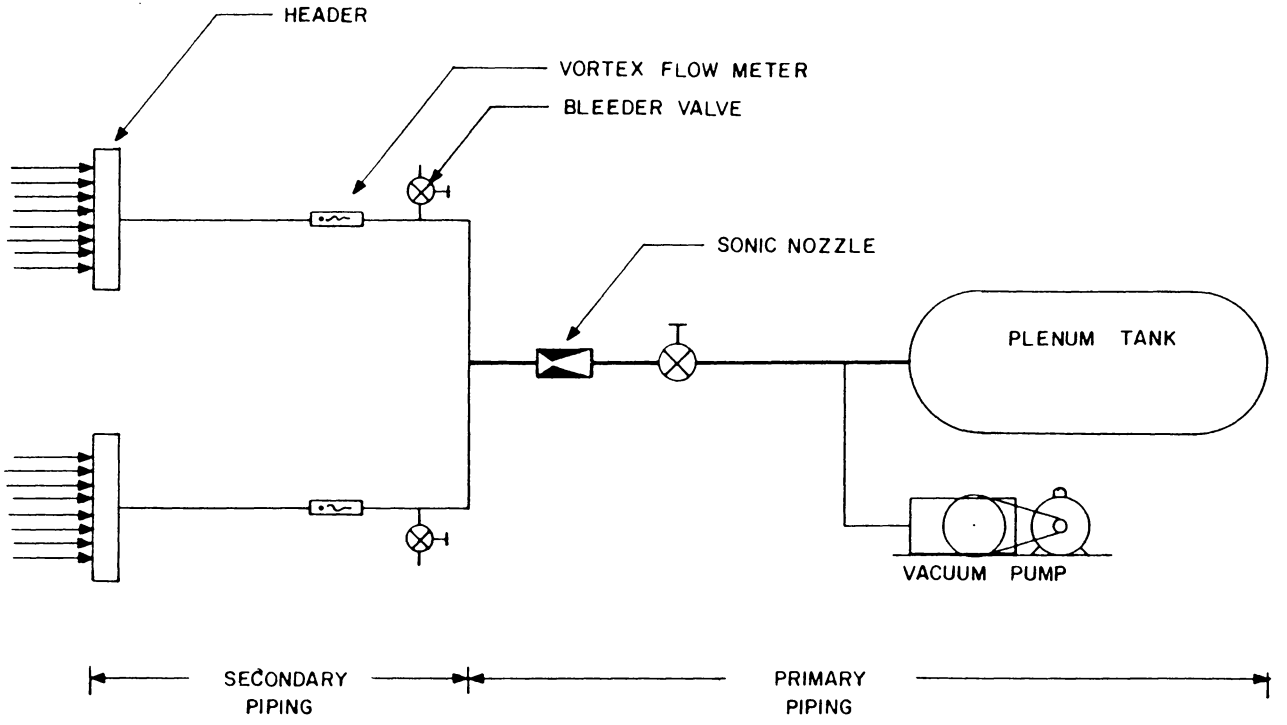

Figure 2.10 Suction system piping diagram.

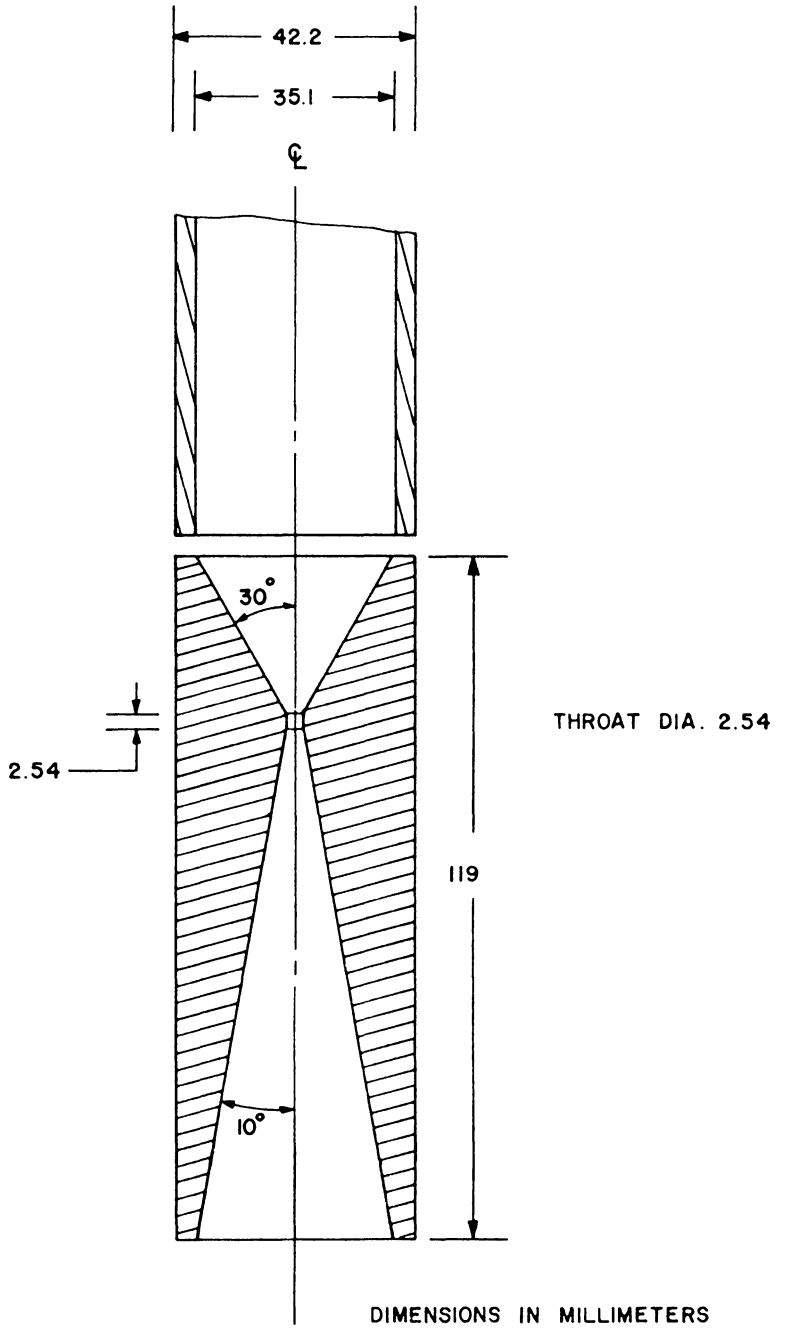

Figure 2.11 Suction choking-nozzle geometry.

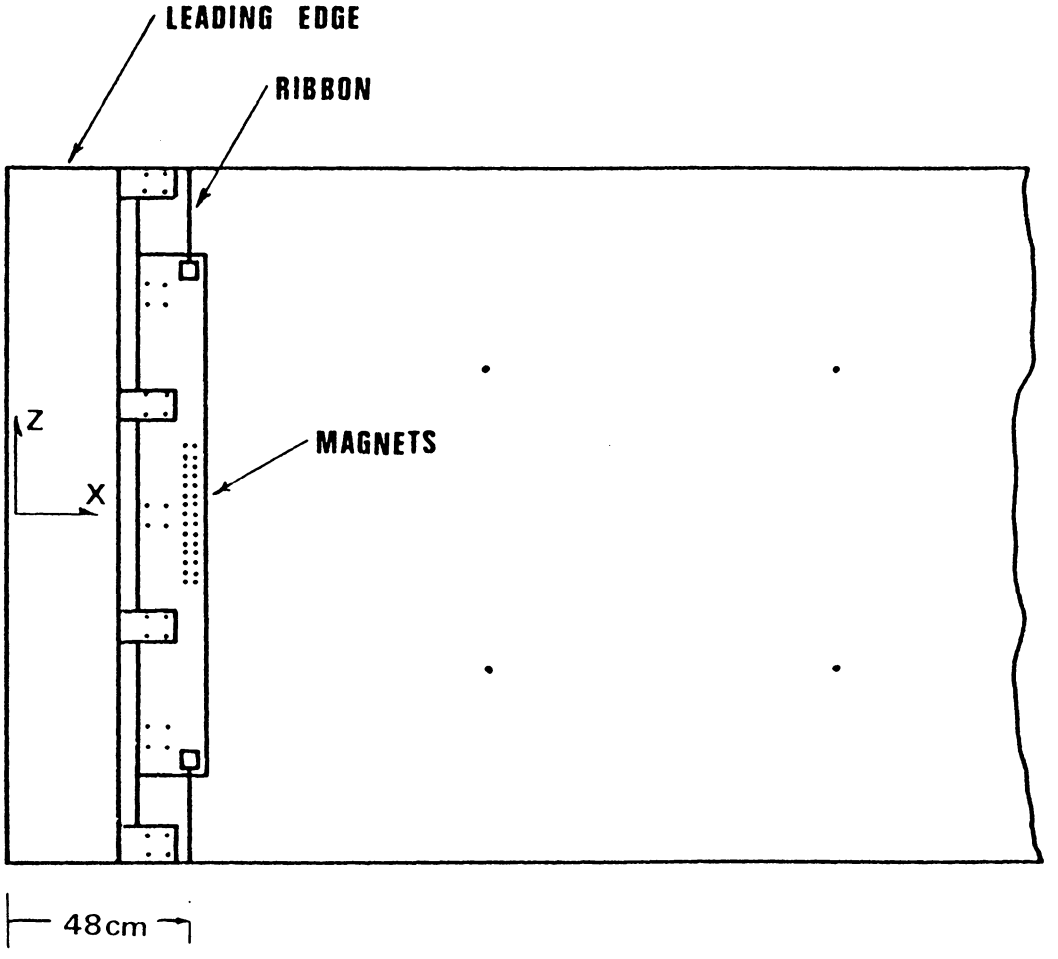

Figure 2.12 Electro-magnet configuration.

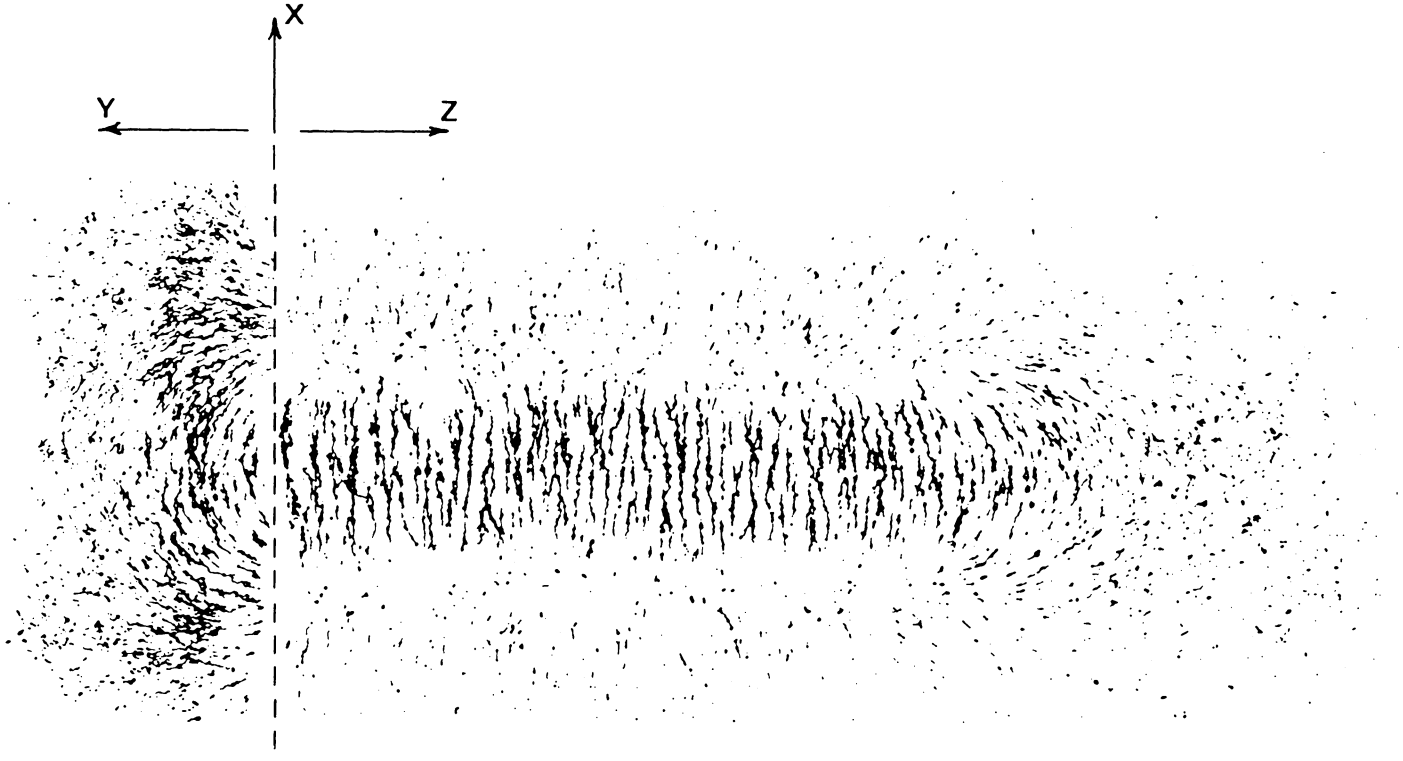

Figure 2.13 Magnetic-field visualization.

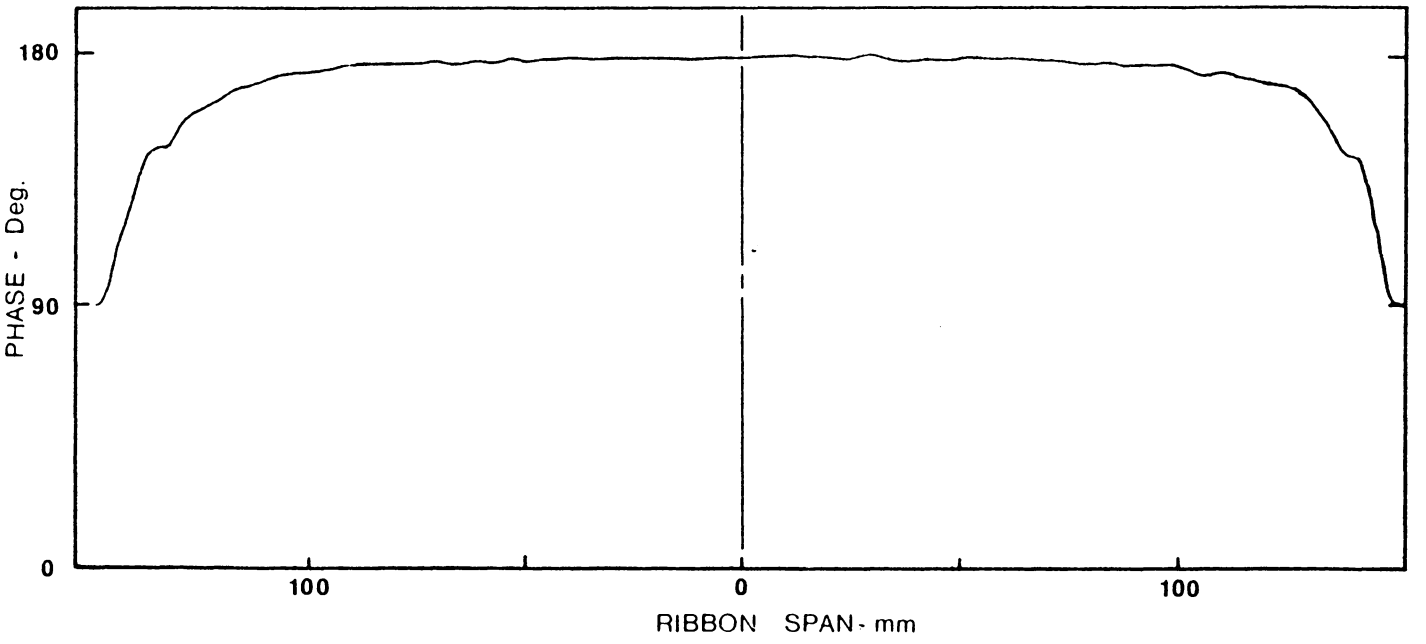

Figure 2.14 Spanwise phase distribution of the vibrating ribbon showing first-mode vibration.

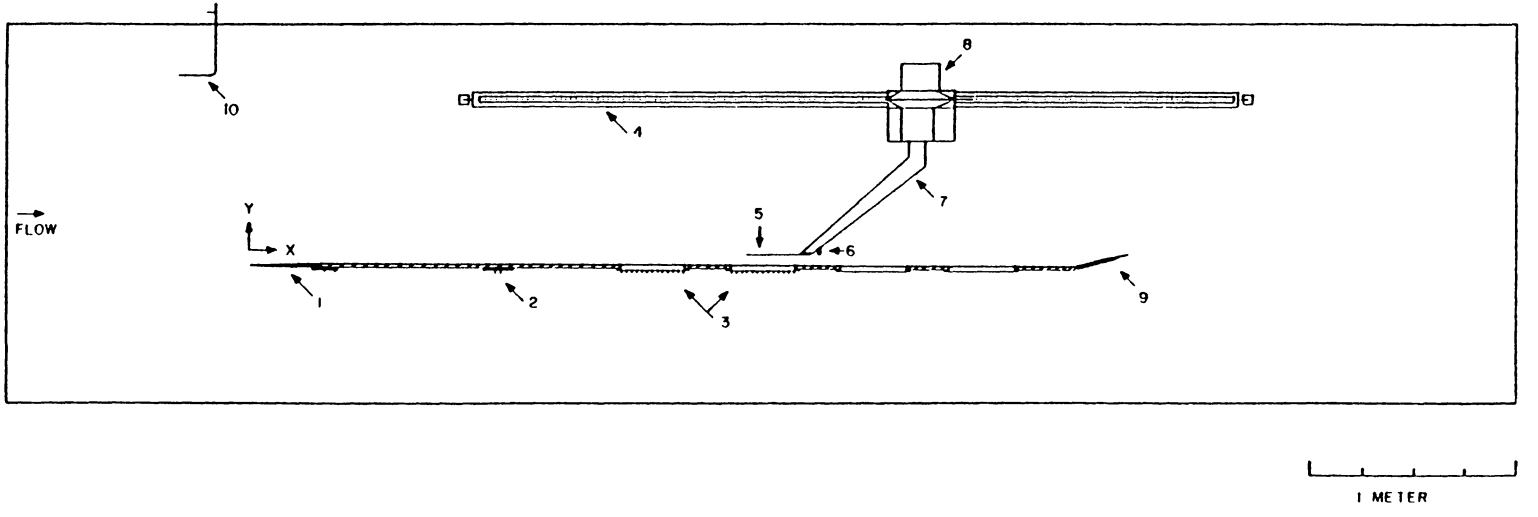

Figure 2.15 Test-section layout for flat-plate experiments using the 2-D traversing mechanism. The items noted are (1) Elliptical leading edge; (2) Electromagnets for the vibrating ribbon; (3) Tubing bundles; (4) Support rail and guide rod for X-traverse; (5) Hot-wire probe extension tube; (6) Proximity probe; (7) Hot-wire probe sting; (8) Fairing for Y-traverse stepping motor; (9) Trailing-edge flap; (10) Pitot tube.

TRAVERSE MECHANISM

	CHORDWISE (x-axis)	NORMAL (y-axis)	SPANWISE (z-axis)
Total Travel	4000. mm	100. mm	1000. mm
Minimum Step	0.6 mm	0.01 mm	0.3 mm
Noncumulative Error	0.03 mm/step	0.0004 mm/step	0.02 mm/step

BOUNDARY LAYER THICKNESS $\simeq$ 5 mm

PLATE LOCATION DETERMINED FROM PROXIMETER PROBE

Figure 2.16 Traverse mechanism specifications.

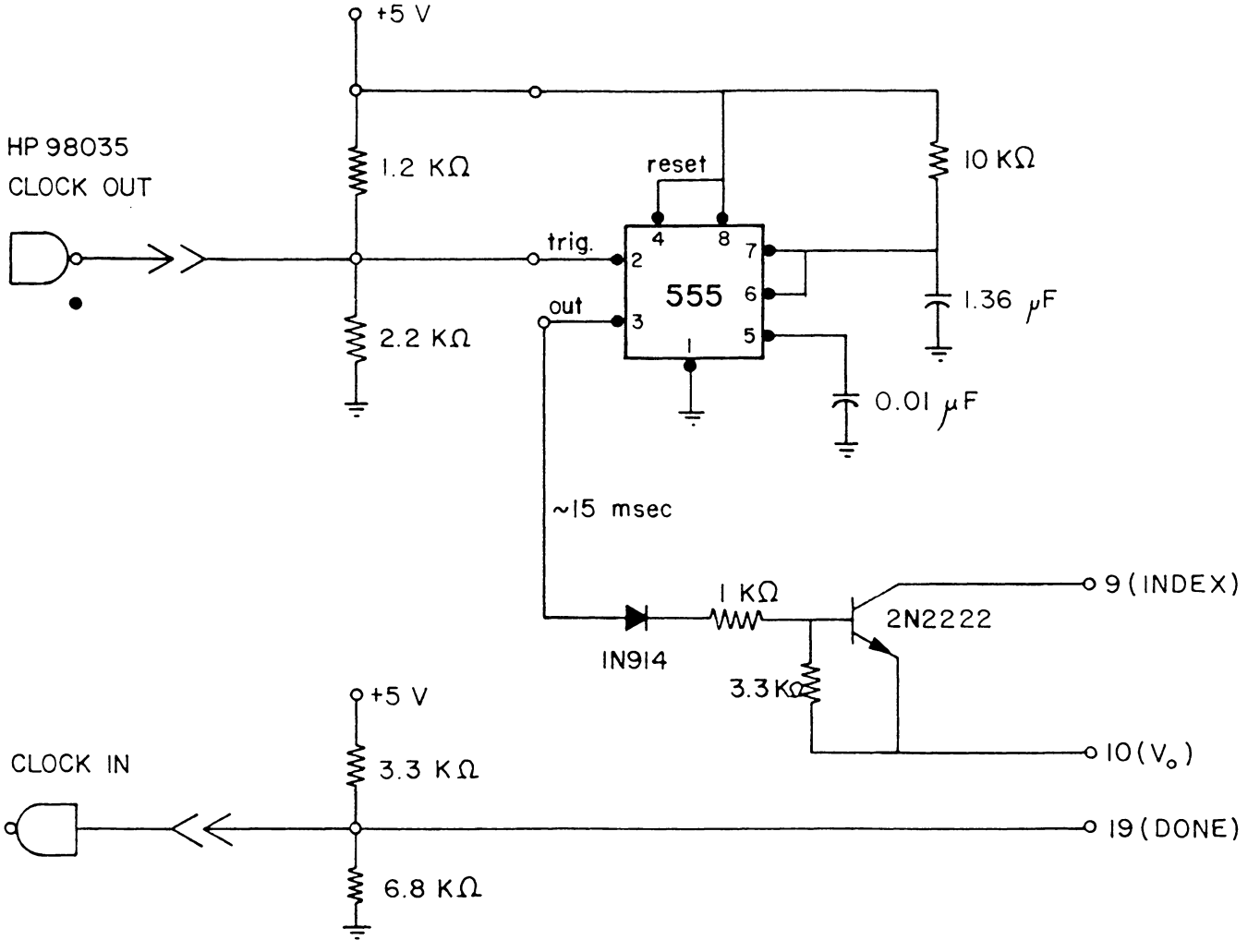

Figure 2.17 Traverse-controller interface circuit.

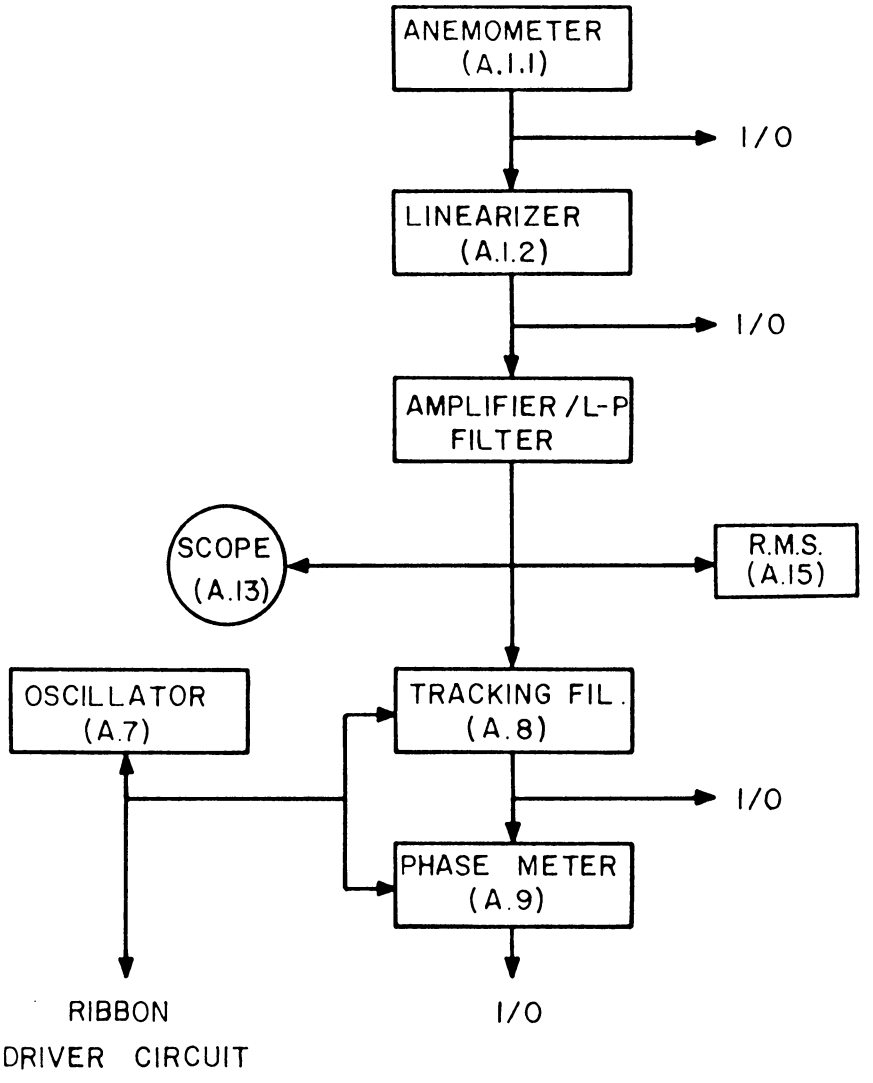

Figure 2.18 Analog signal processing of anemometer output.

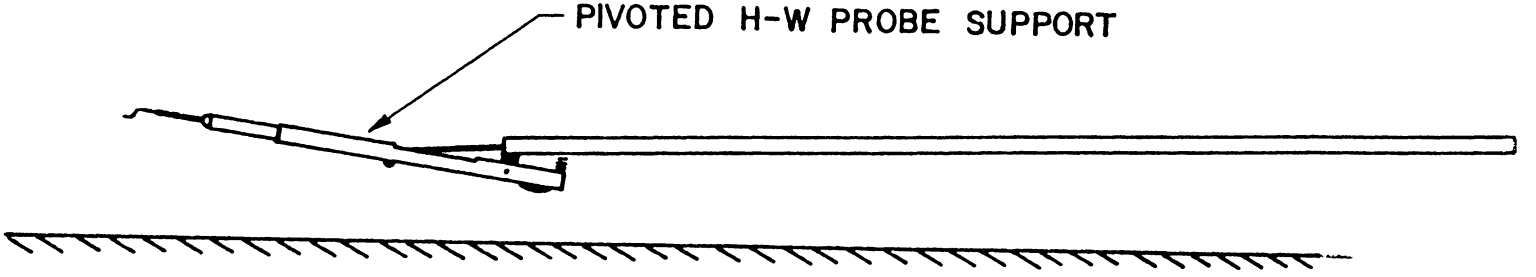

Figure 2.19 Hot-wire probe holder for measurement of transition Reynolds number.

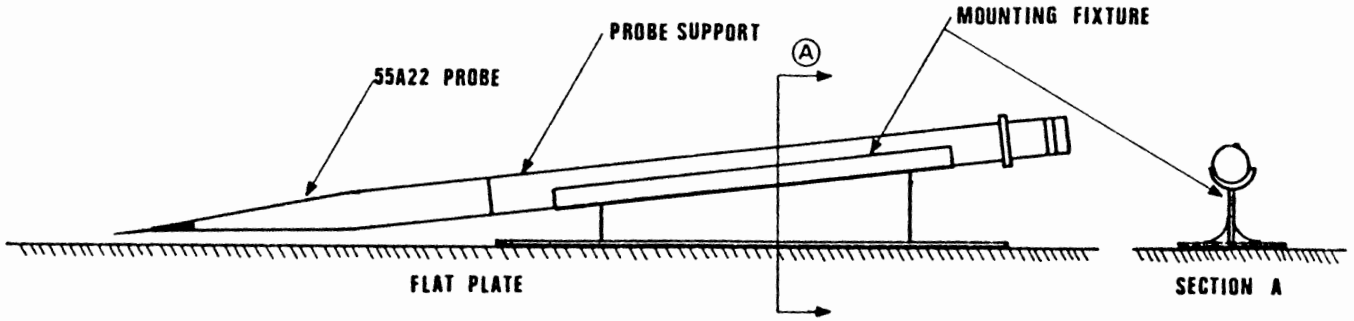

Figure 2.20 Fixed probe mount and DISA 55A22 probe.

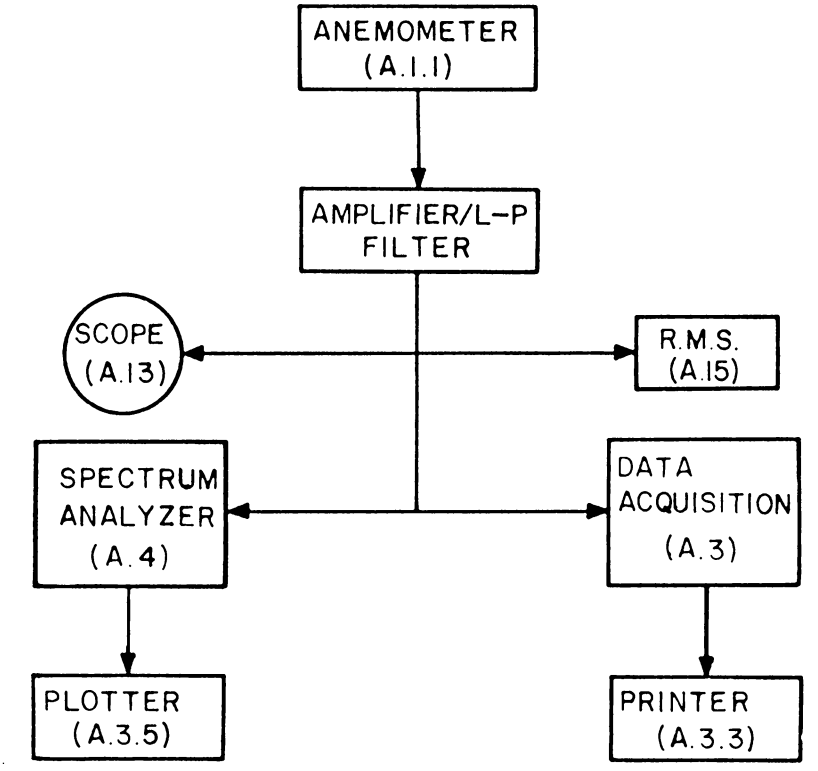

Figure 3.1 Signal processing for turbulence measurements.

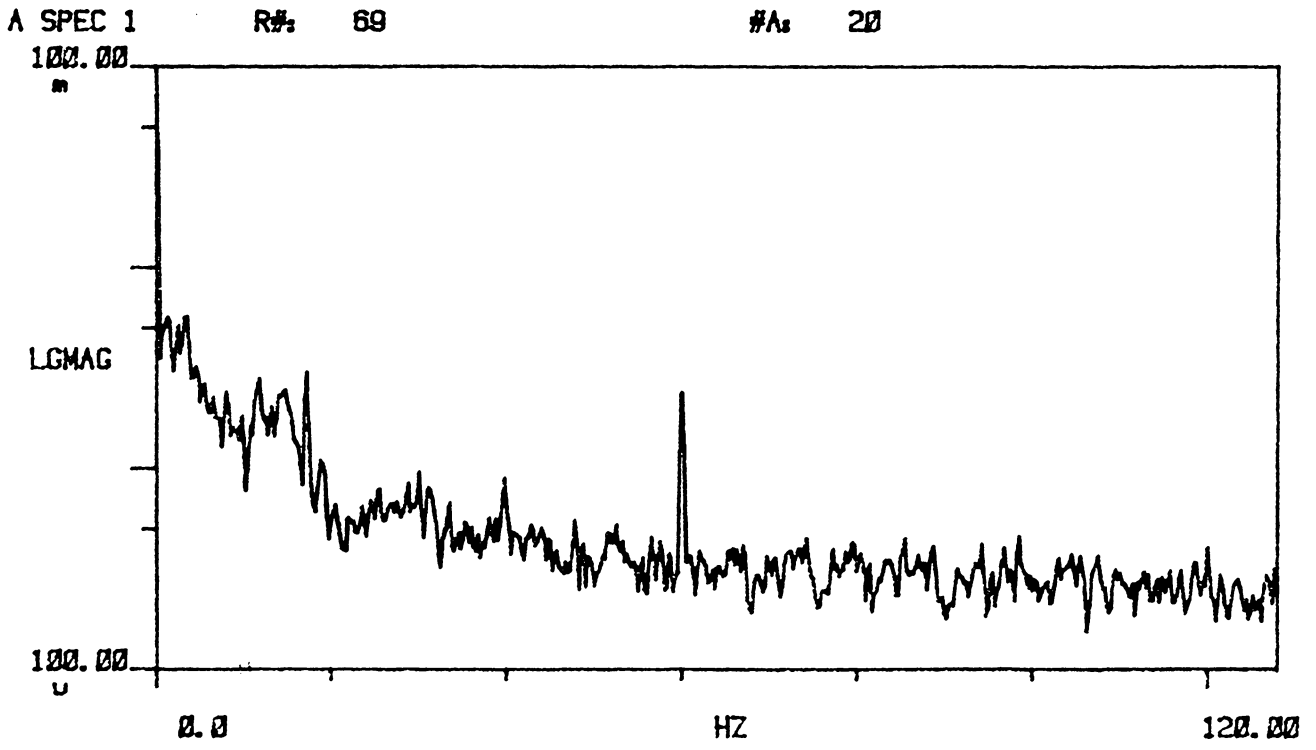

Figure 3.2 Turbulence spectrum at Ue = 15 m/s, where |u'|/Ue = 0.018%.

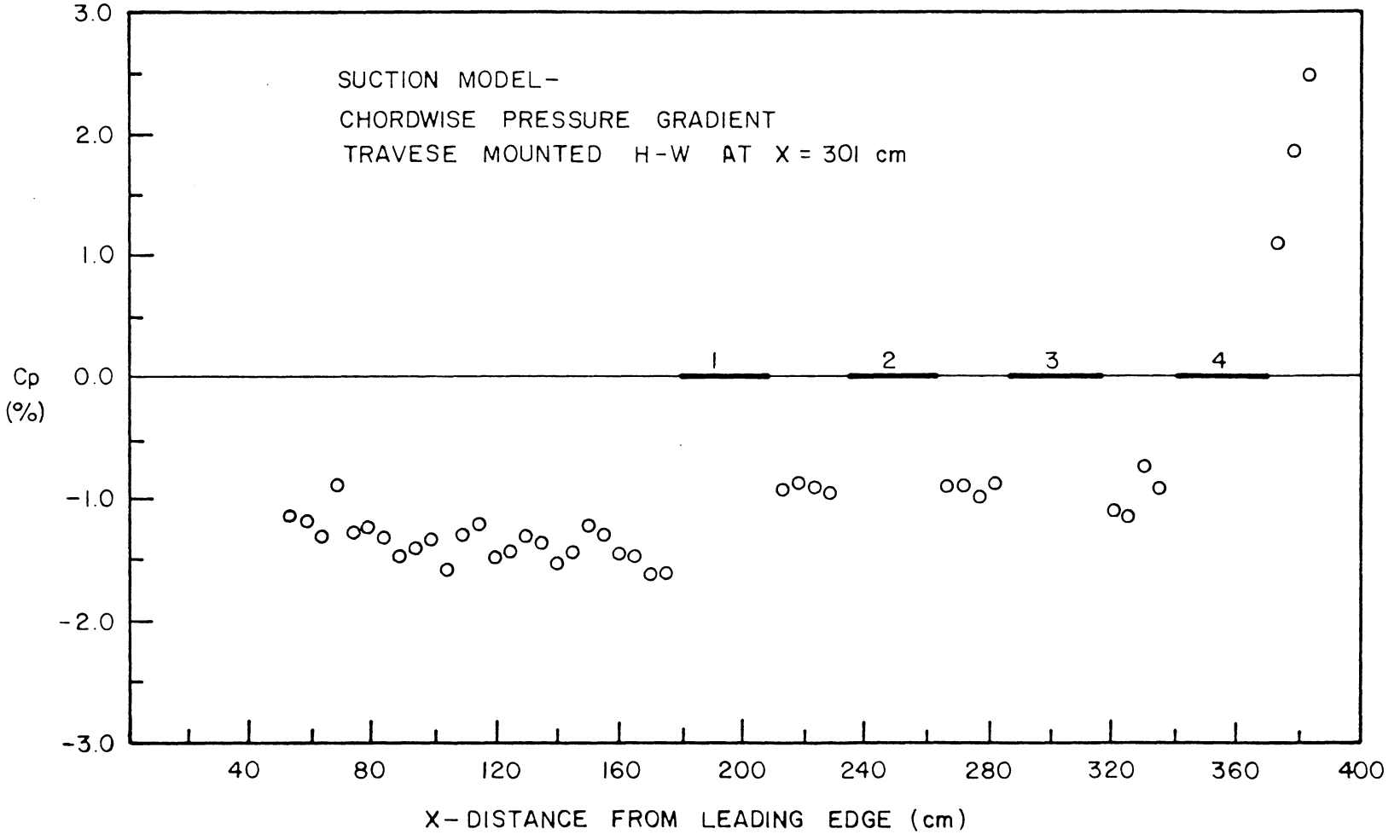

Figure 3.3 Chordwise pressure gradient showing zero pressure gradient at the hot-wire probe located at X = 301 cm. Reference static pressure is from the Pitot tube ahead of the plate.

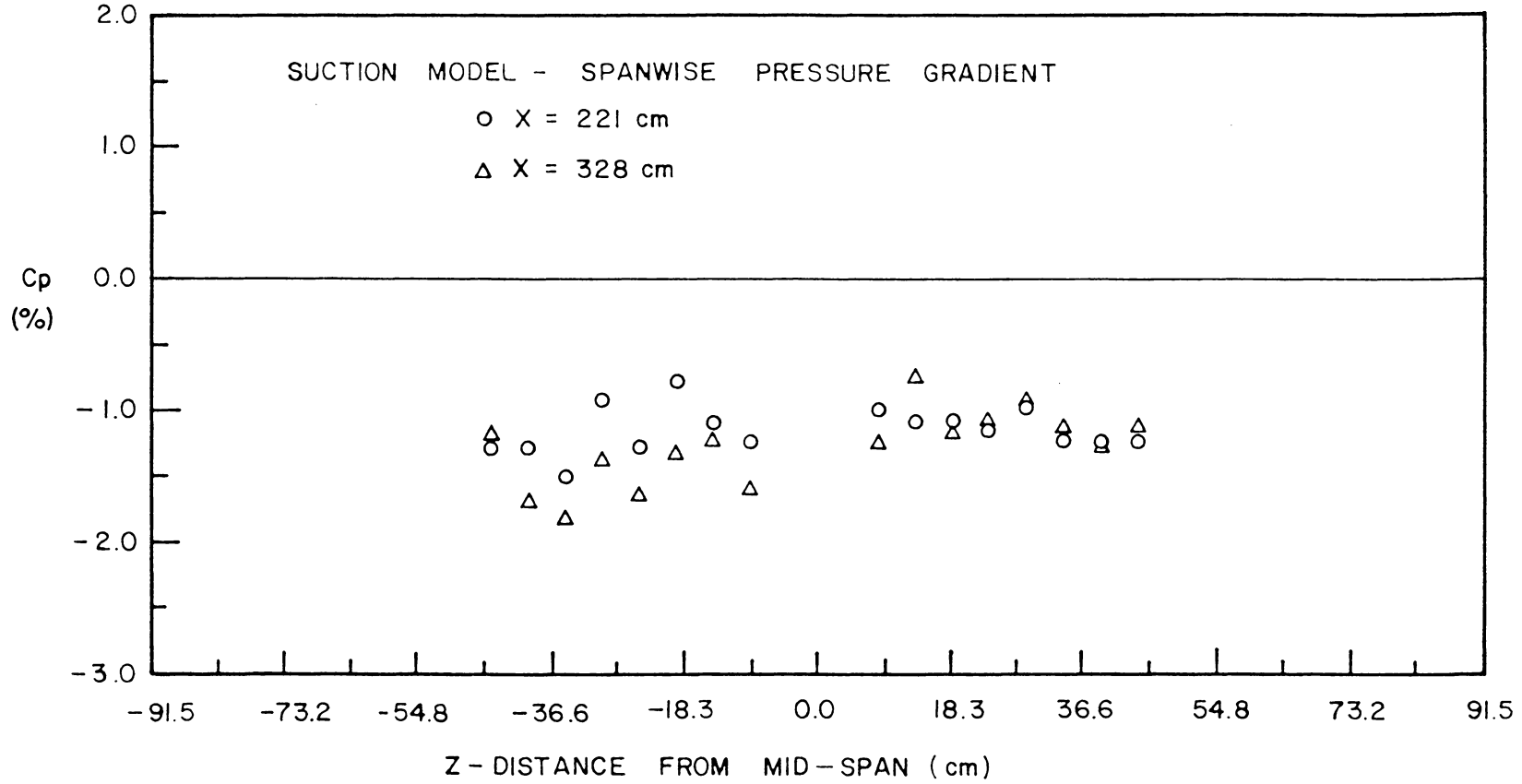

Figure 3.4 Spanwise pressure gradient with traverse mounted hot-wire probe located at X = 301 cm. Reference static pressure is from the Pitot tube ahead of the plate.

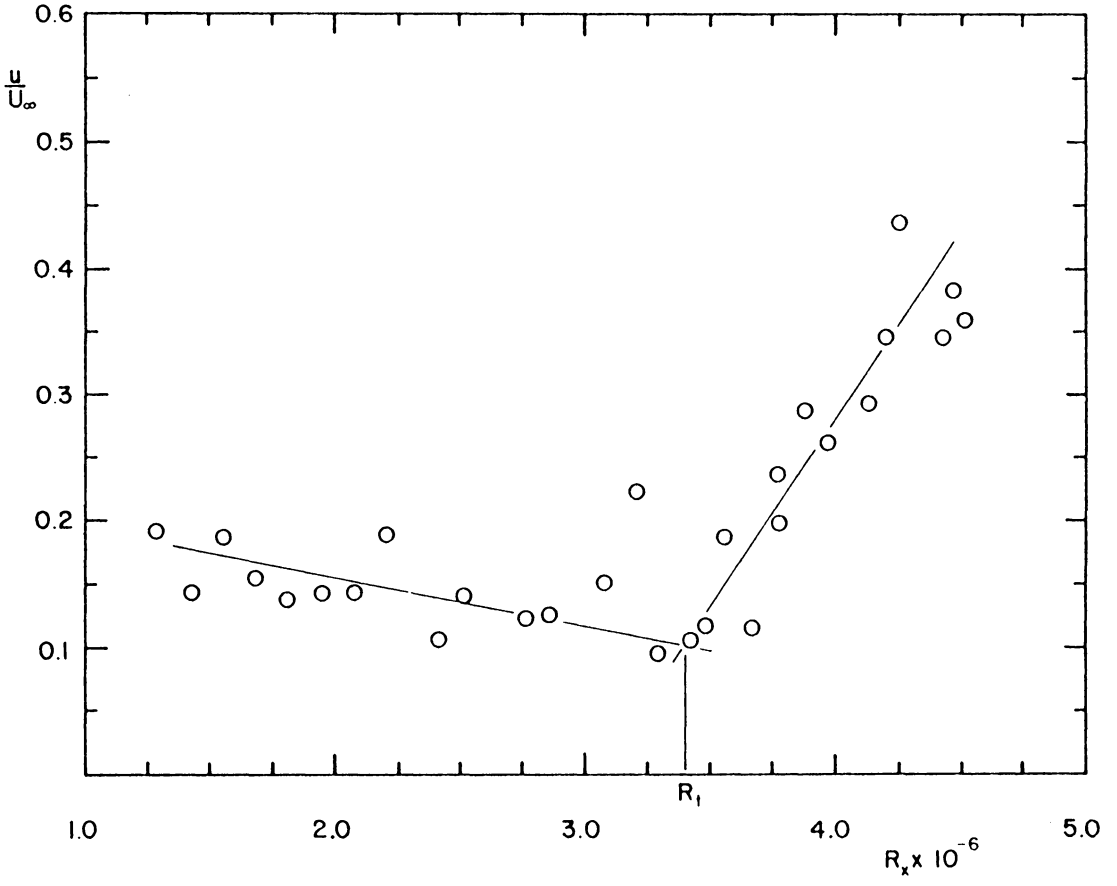

Figure 3.5 Transition Reynolds number obtained with moving the hot-wire probe. Rt = 3.4 x 10^6.

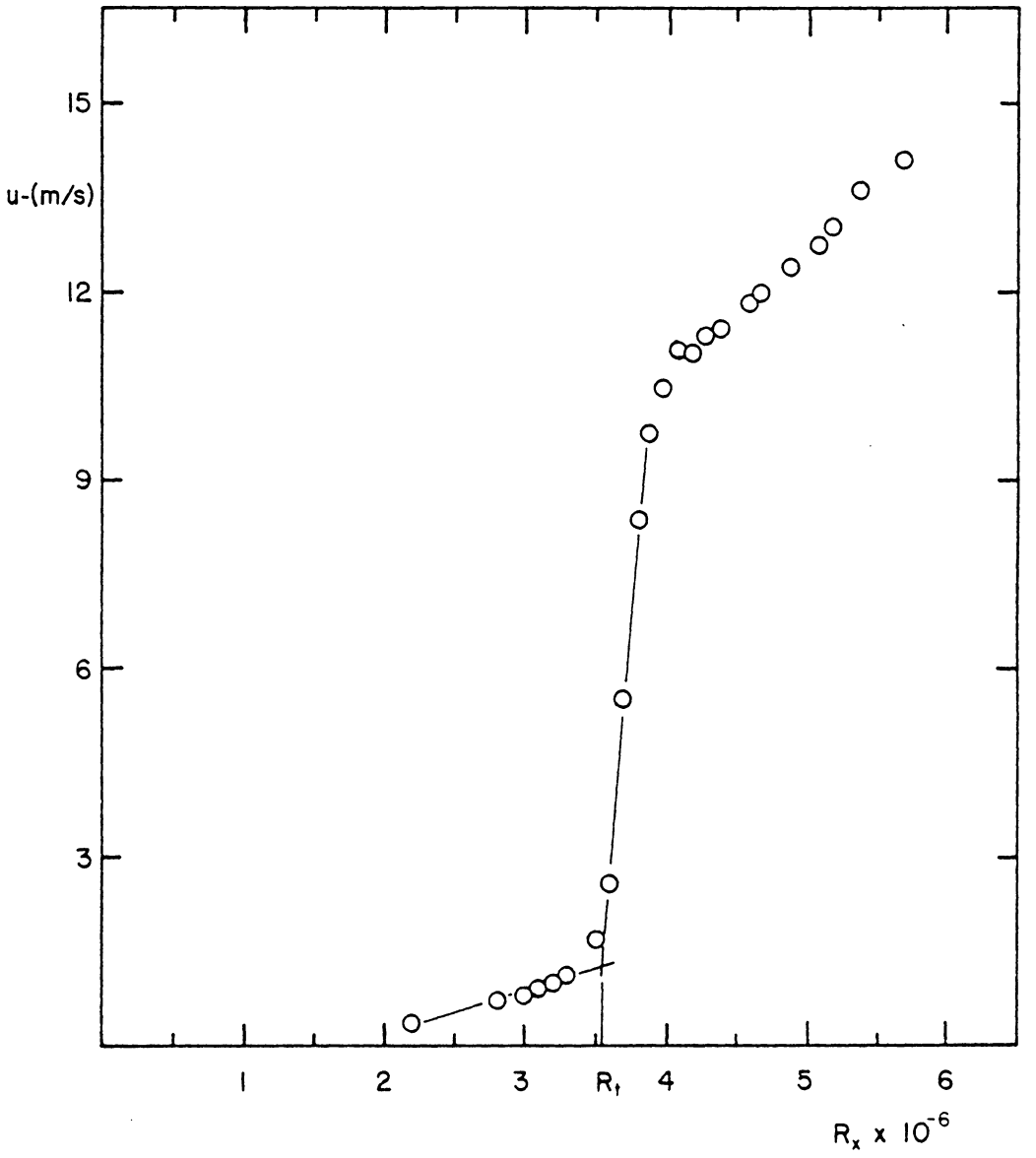

Figure 3.6 Transition Reynolds number obtained with the fixed hot-wire probe. Rt = 3.5 x 10^6.

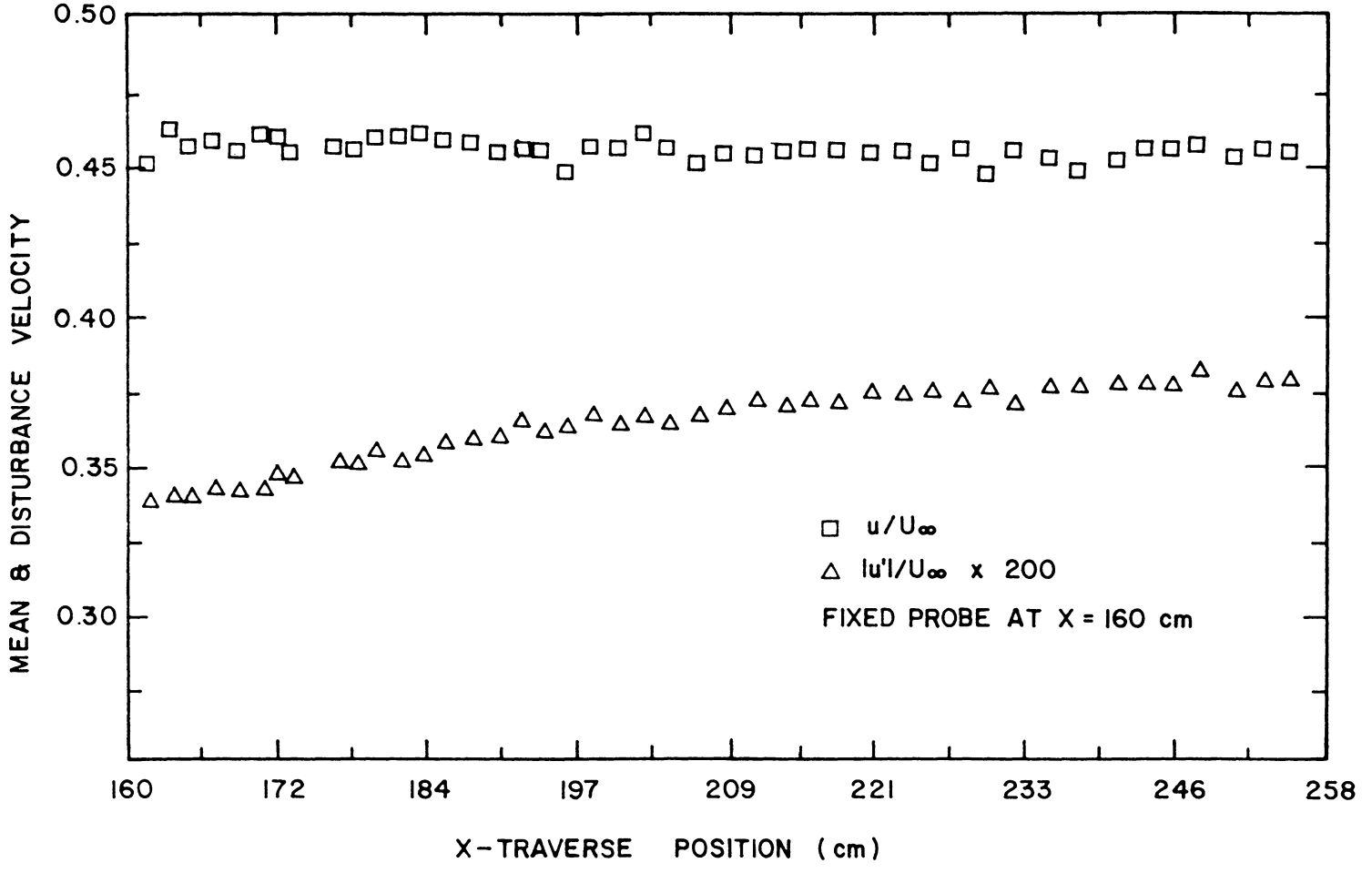

Figure 3.7 Disturbance amplitude and mean-flow variation measured by a fixed hot-wire probe in the boundary layer, due to movement of the traverse.

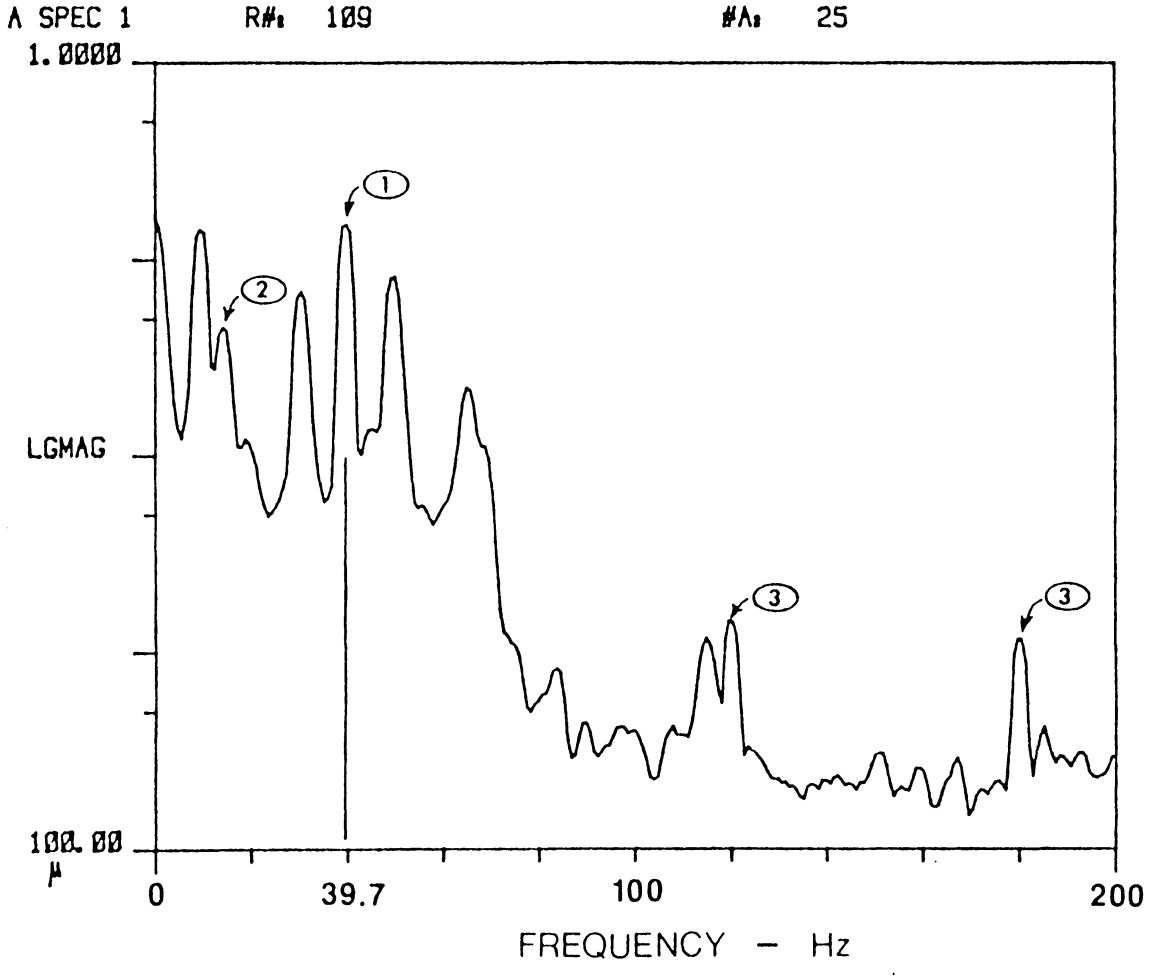

Figure 3.8 Hot-wire anemometer output spectrum showing
(1) T-S wave at 39.7 Hz and max|u'|/Ue = 0.04%.
(2) probe vibration at 14 Hz due to motor generator
(3) electronic noise at 120 Hz and 180 Hz.

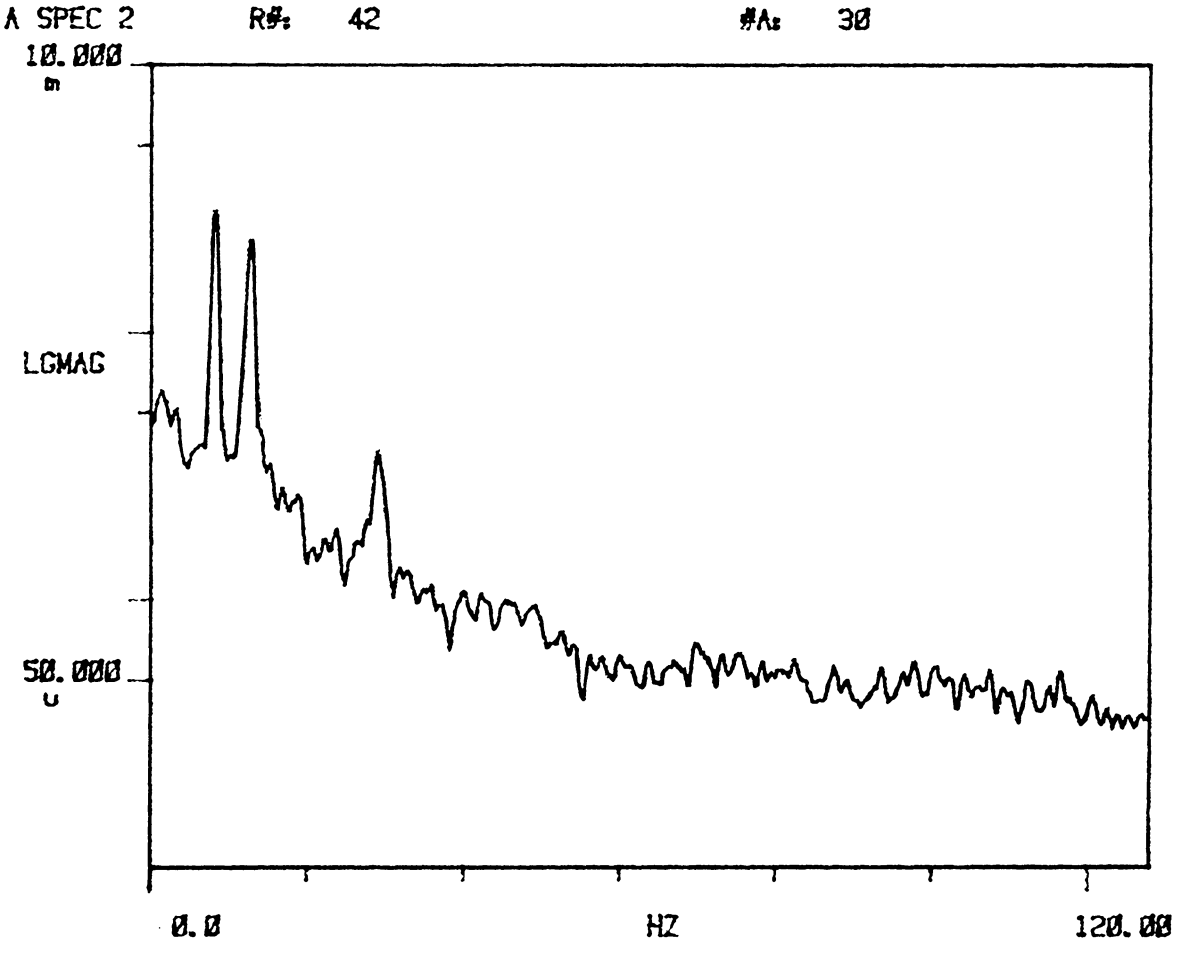

Figure 3.9 Extension arm vibration as measured by the traverse mounted inductance probe.

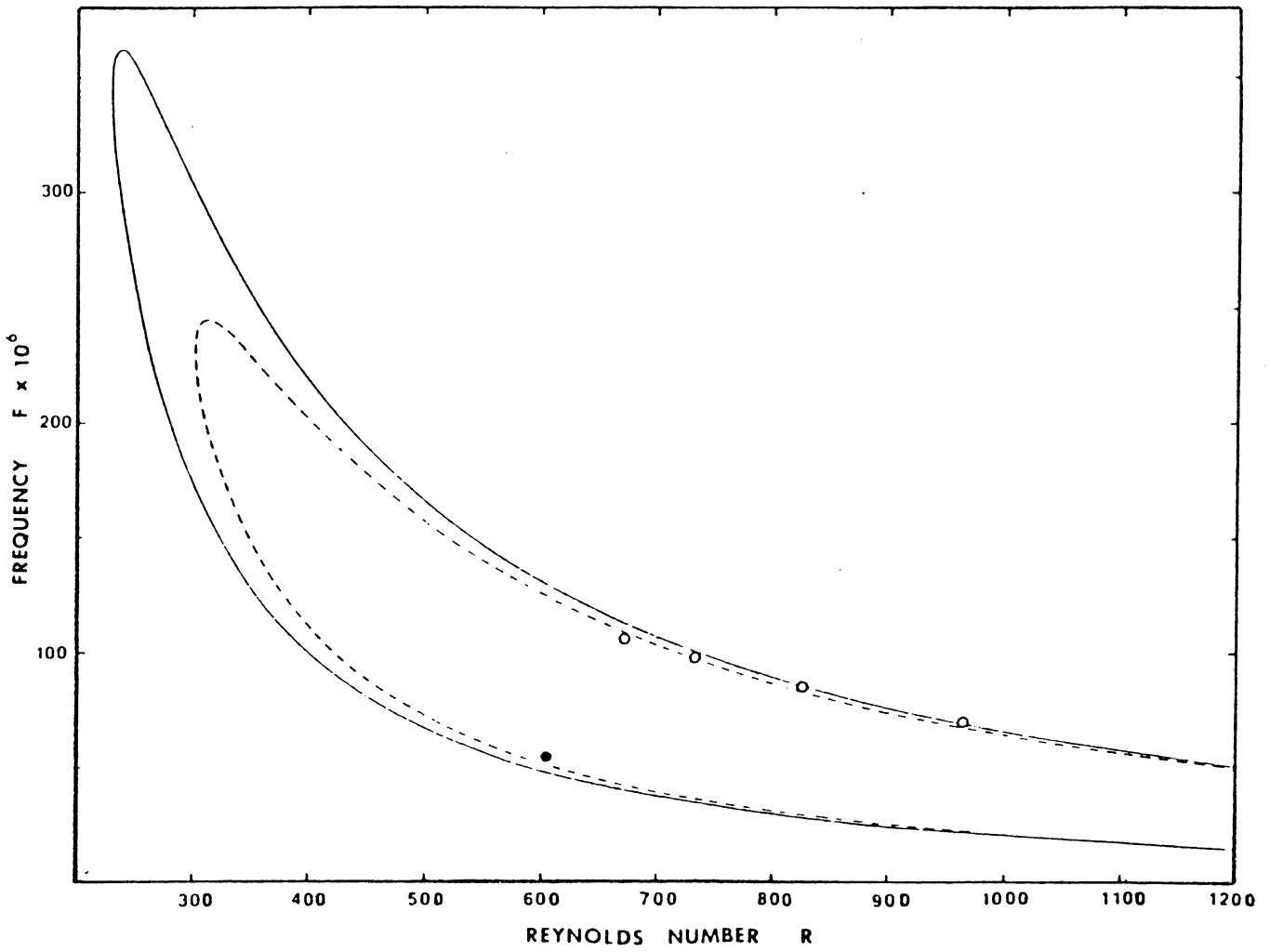

Figure 3.10 Neutral-stability curve showing the present results obtained by measurements of max|u'|. Solid symbols are Branch I and open symbols are Branch II.

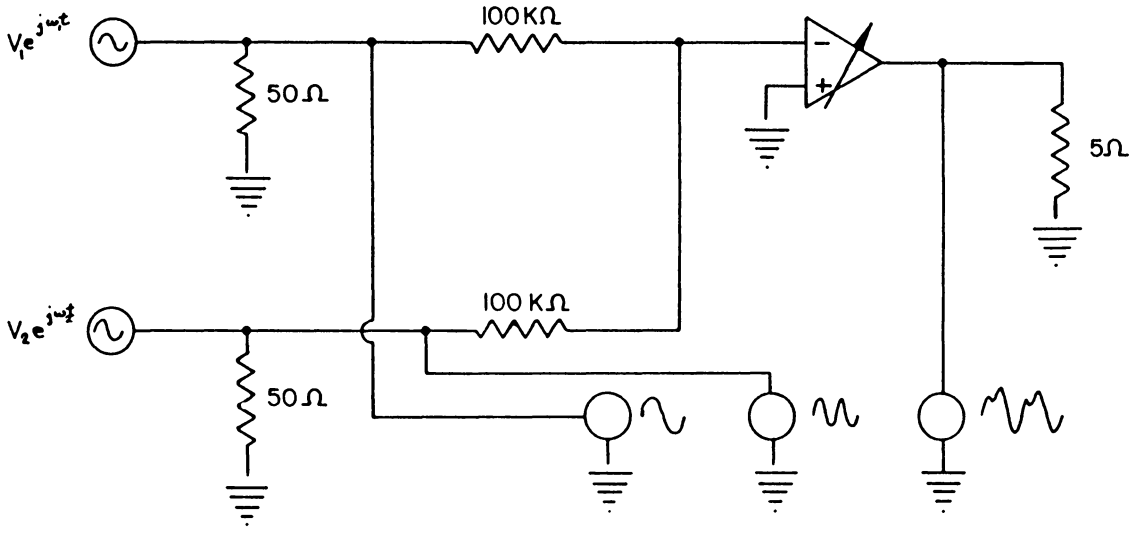

Figure 3.11 Two-frequency signal mixer used for multiple-frequency ribbon excitation.

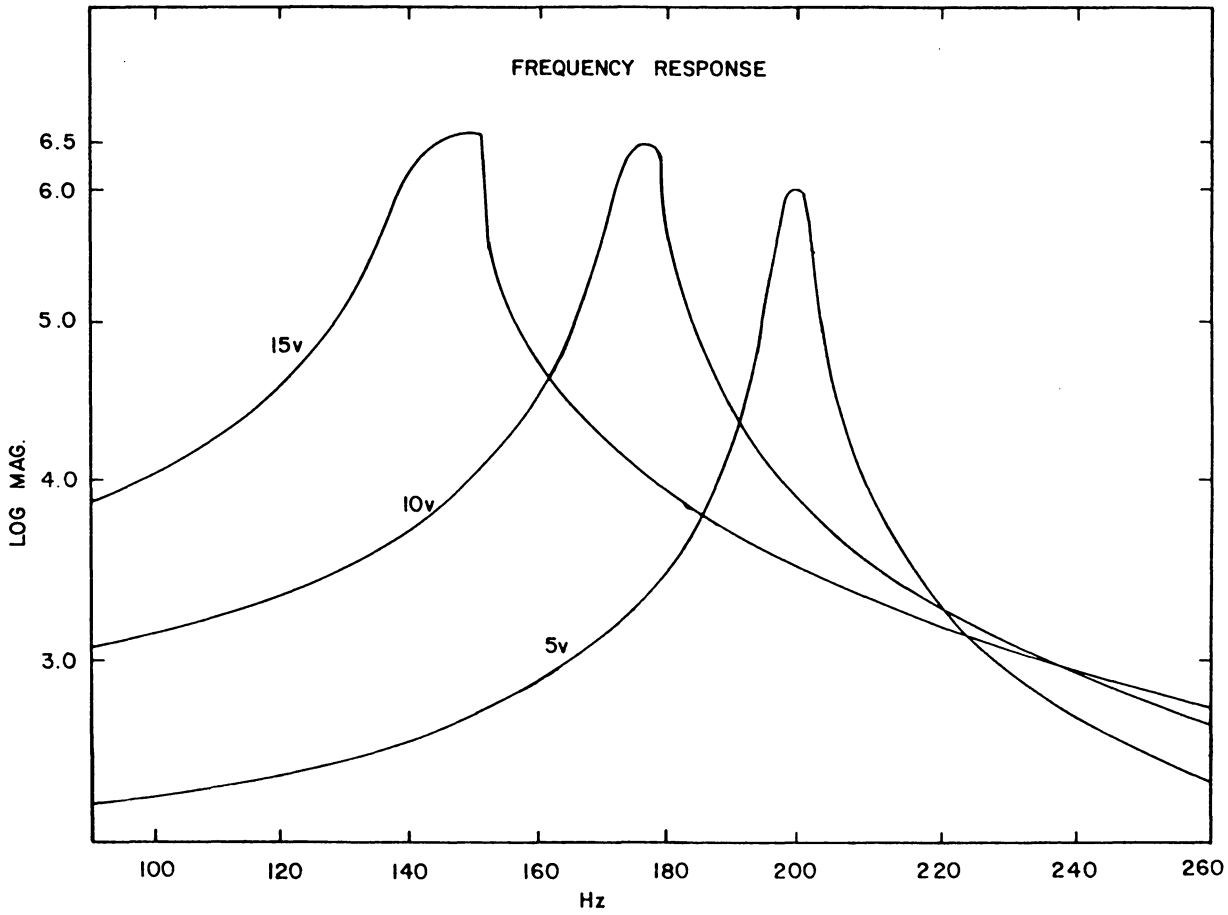

Figure 3.12 Ribbon frequency response at three input voltage levels.

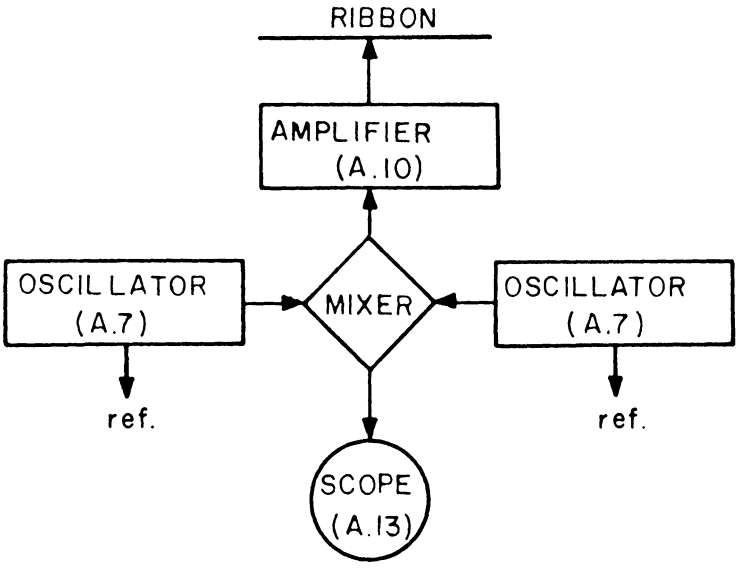

Figure 3.13 Ribbon inputs for two-frequency experiments.

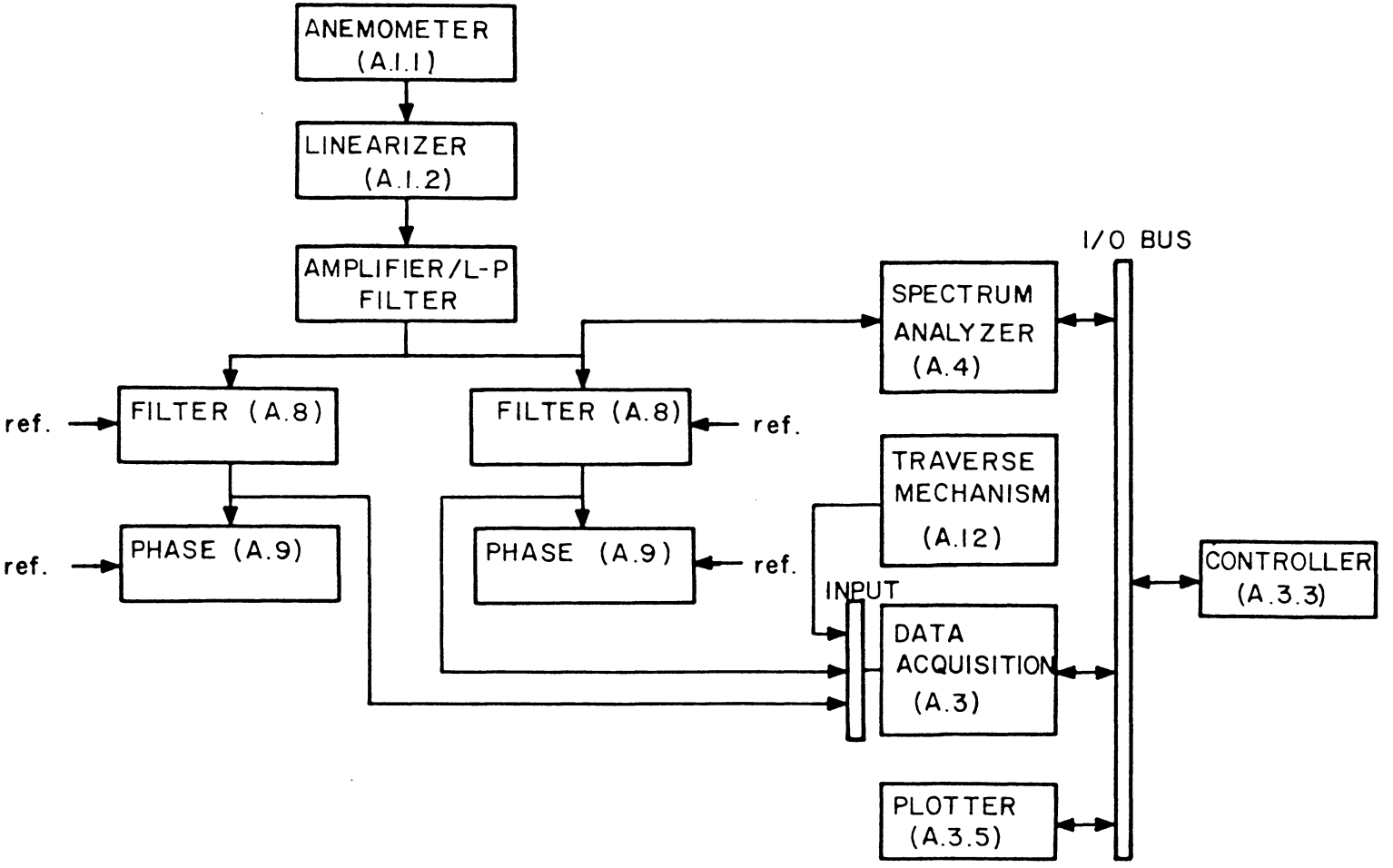

Figure 3.14 Anemometer signal processing for two-frequency measurements.

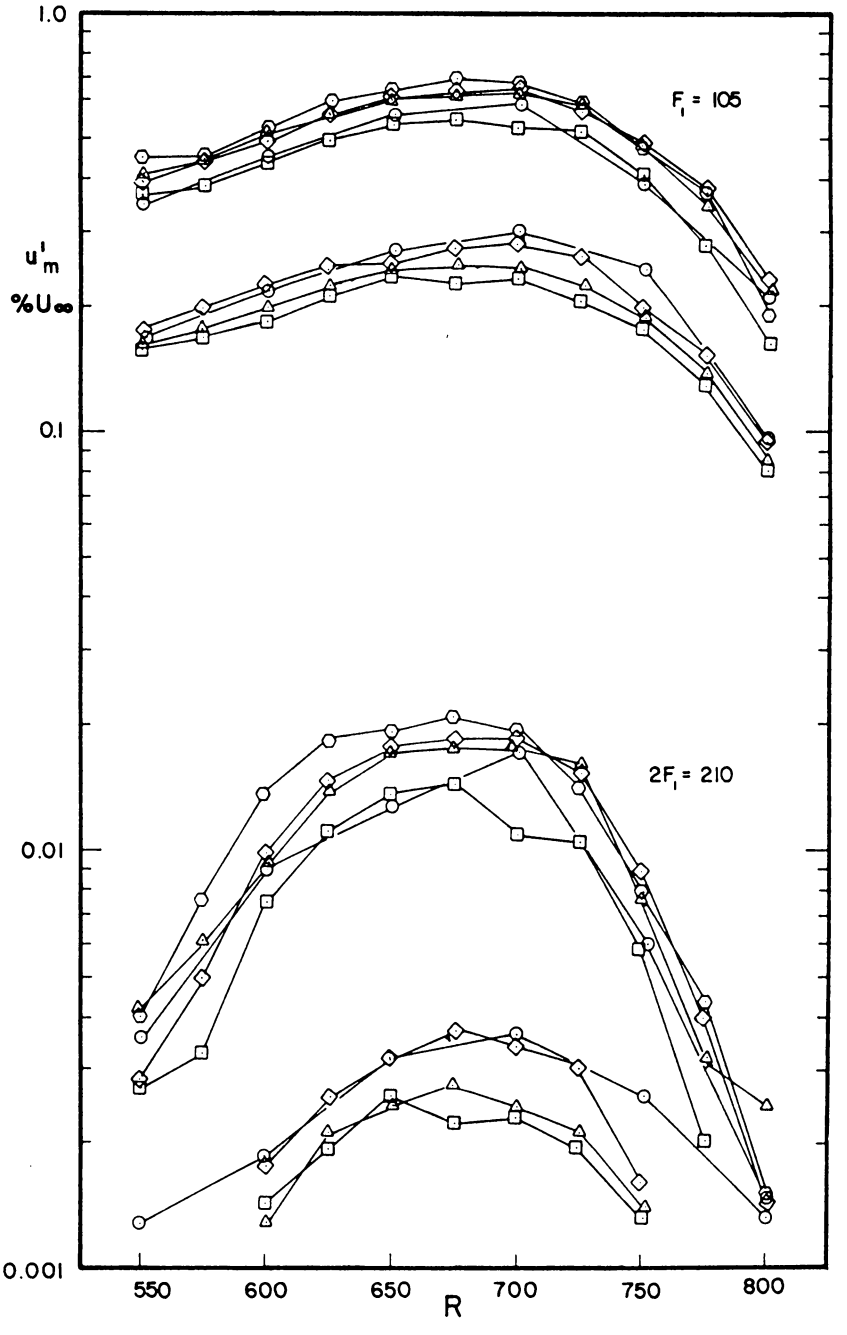

Figure 3.15 Behavior of F_1 and $2F_1$.

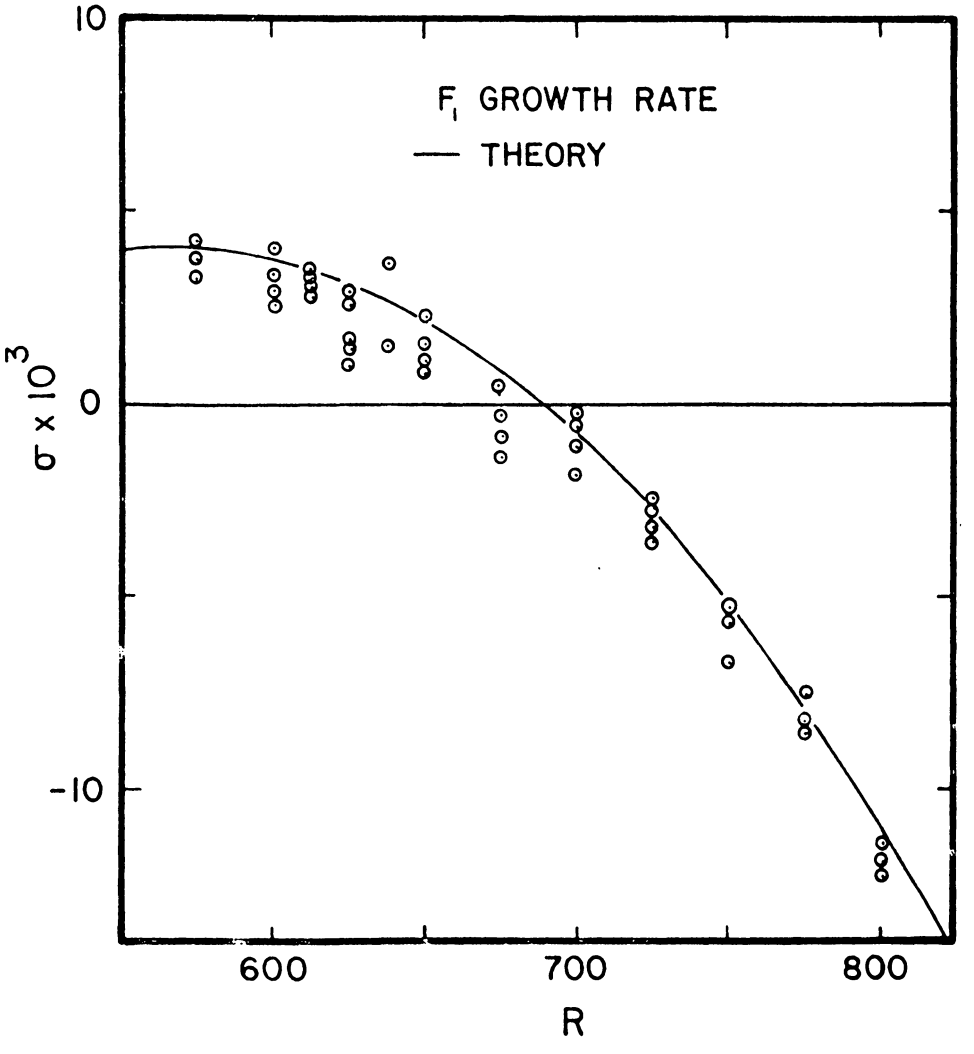

Figure 3.16 Growth rate of F_1.

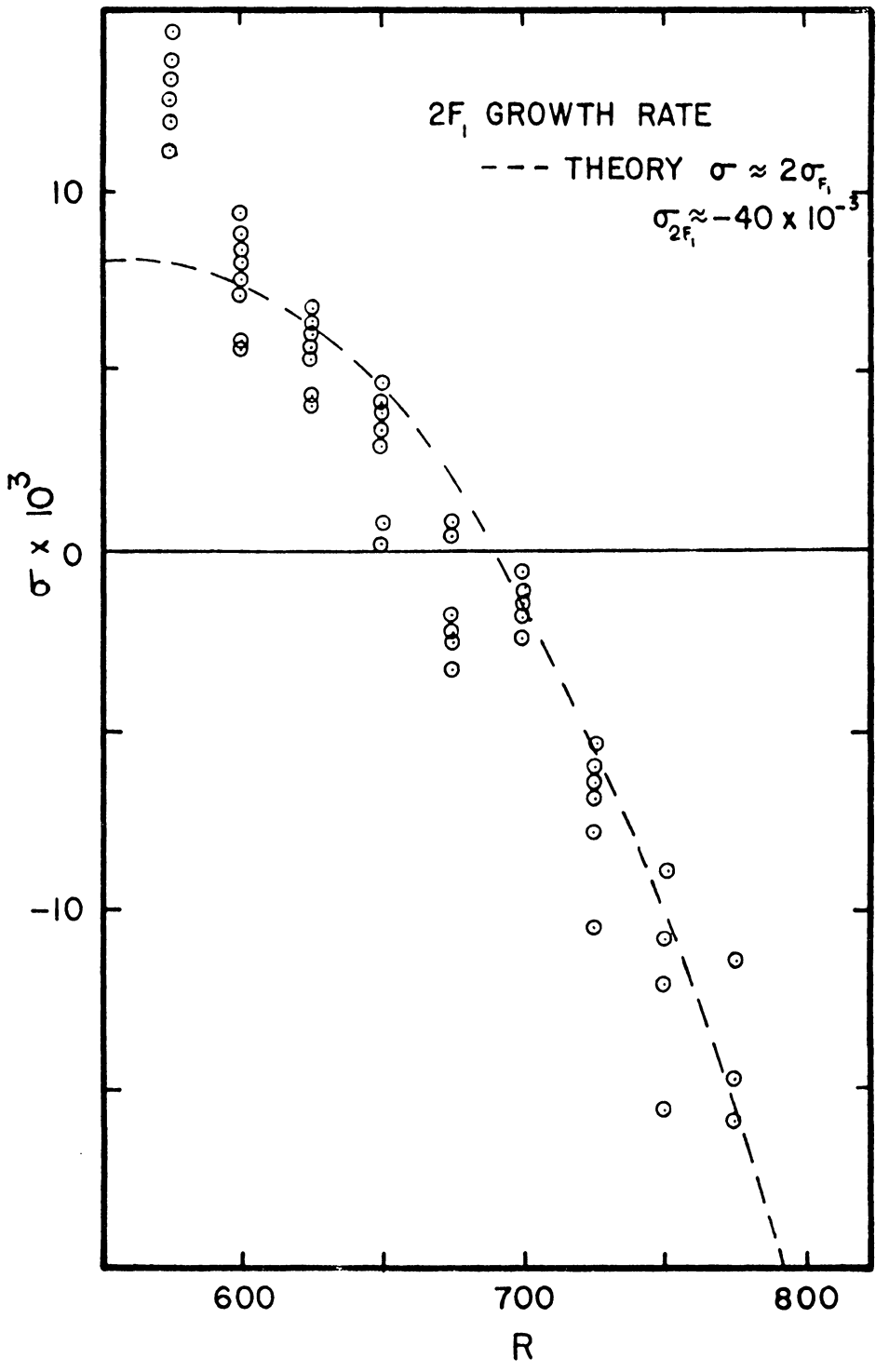

Figure 3.17 Growth rate of $2F_1$.

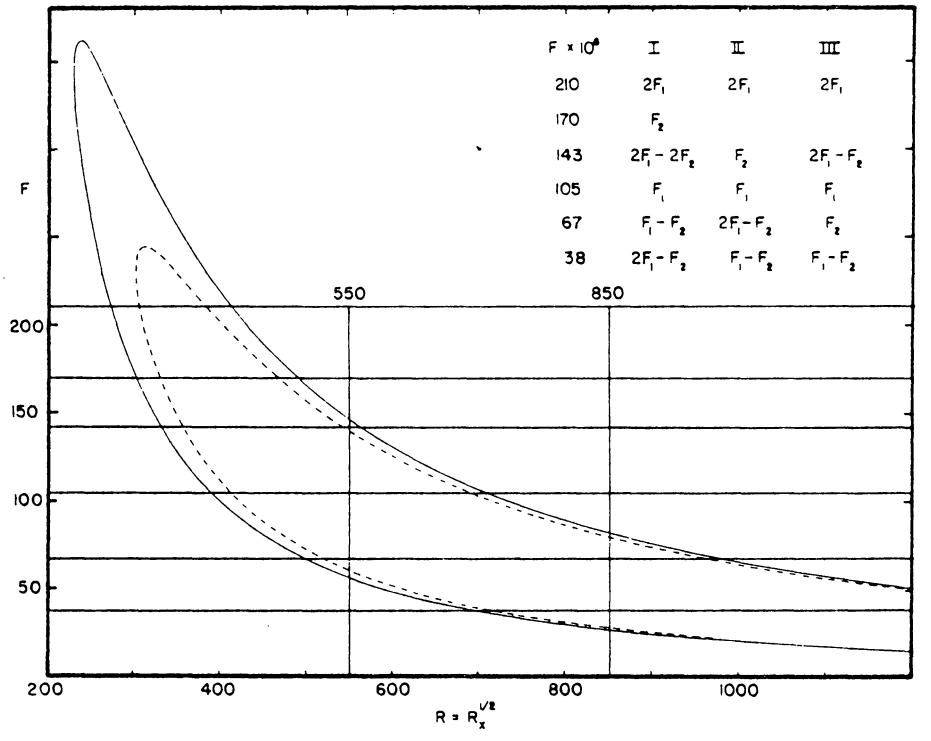

Figure 3.18 Three test cases for nonlinear experiments and the corresponding frequencies for each case.

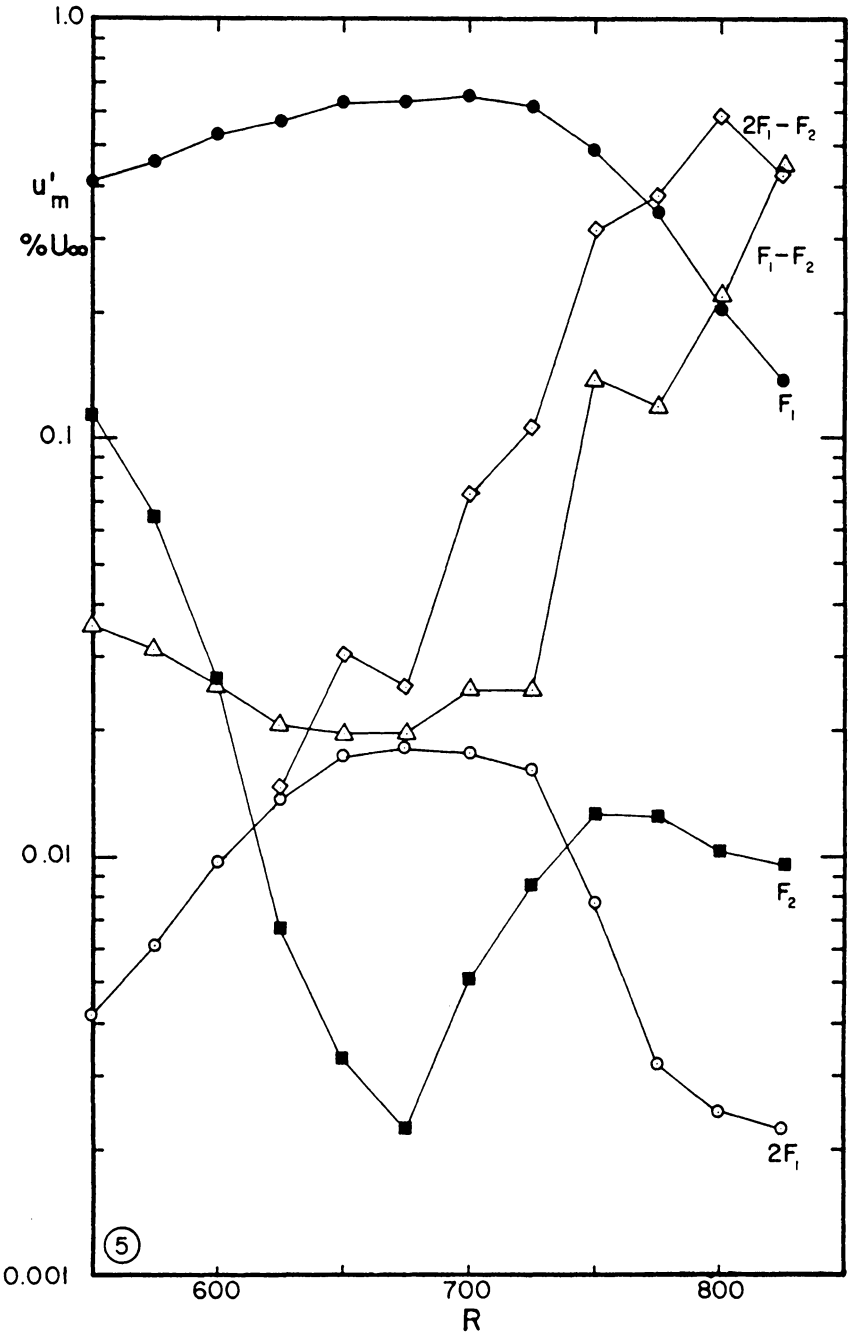

Figure 3.19 Results of nonlinear test case I - high amplitude.

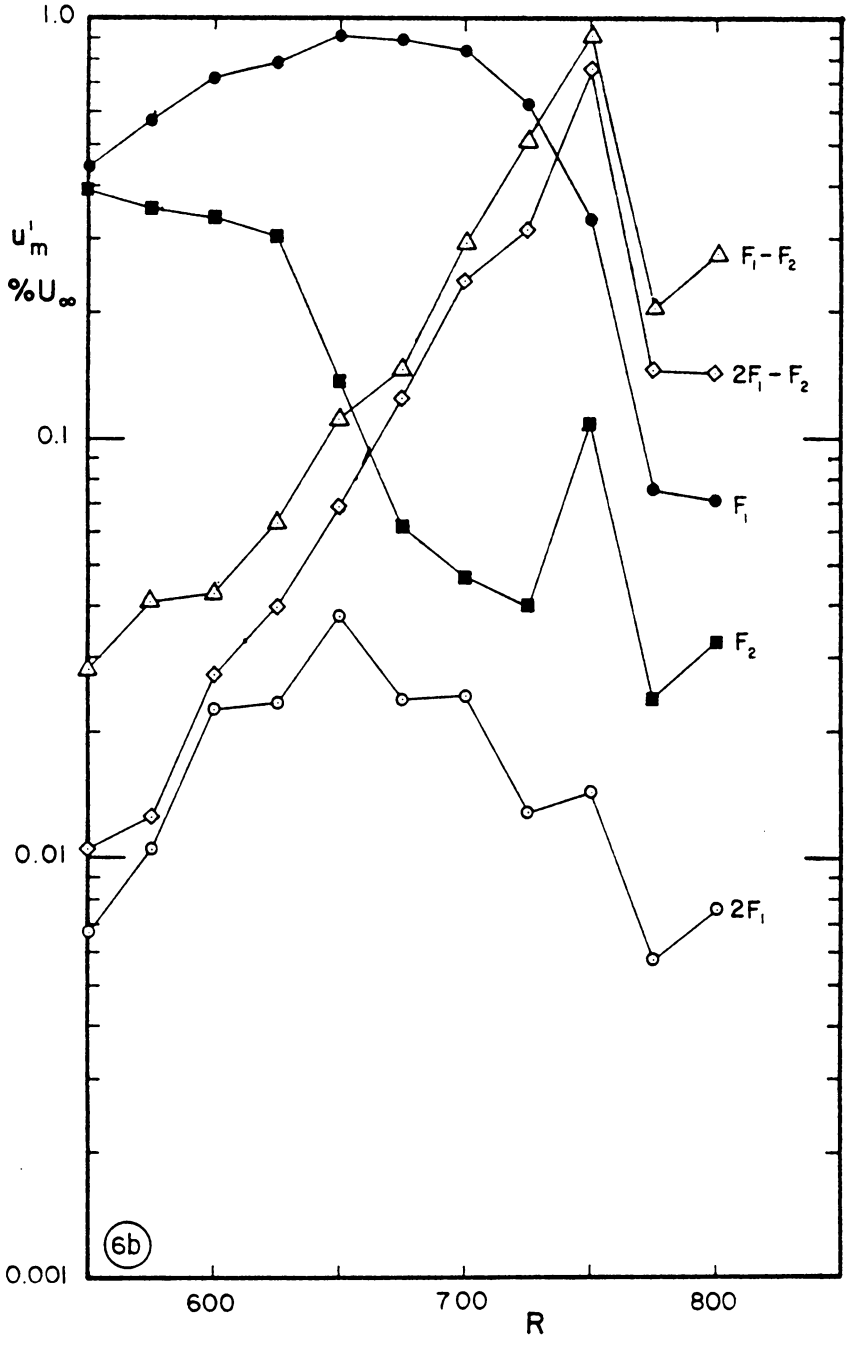

Figure 3.20 Results of nonlinear test case II - high amplitude.

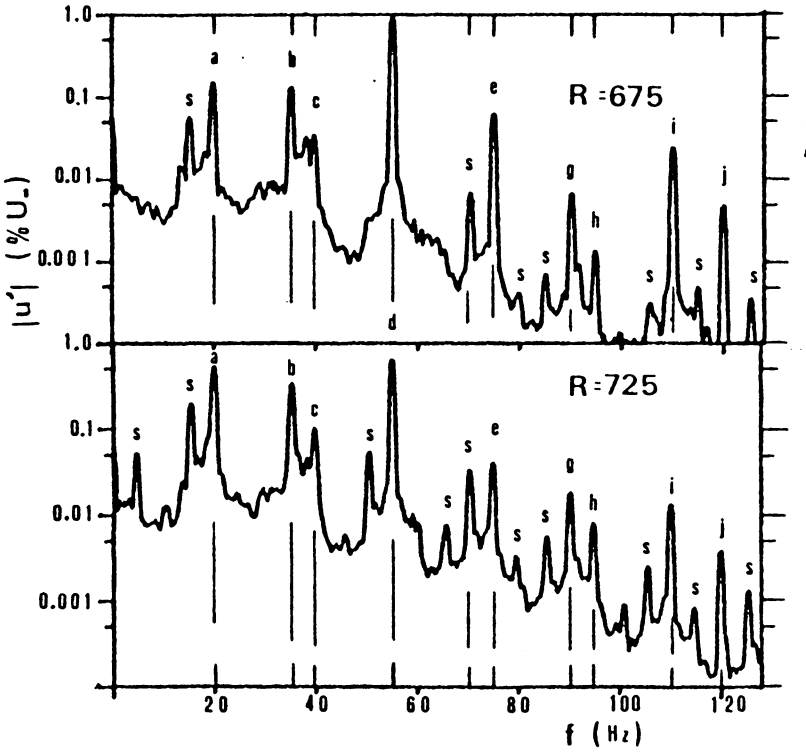

Spectra at two Reynolds numbers of Fig. 4b. Amplitude peaks are defined as:
(a) $F_1 - F_2$
(b) $2F_1 - F_2$
(c) $2F_1 - 2F_2$
(d) F_1
(e) F_2
(g) $3F_1 - F_2$
(h) $F_1 - 2F_2$
(i) $2F_1$
(j) $F_1 + F_2$
(s) possible 3-D effects.

Figure 3.21 Disturbance spectra for test case II.

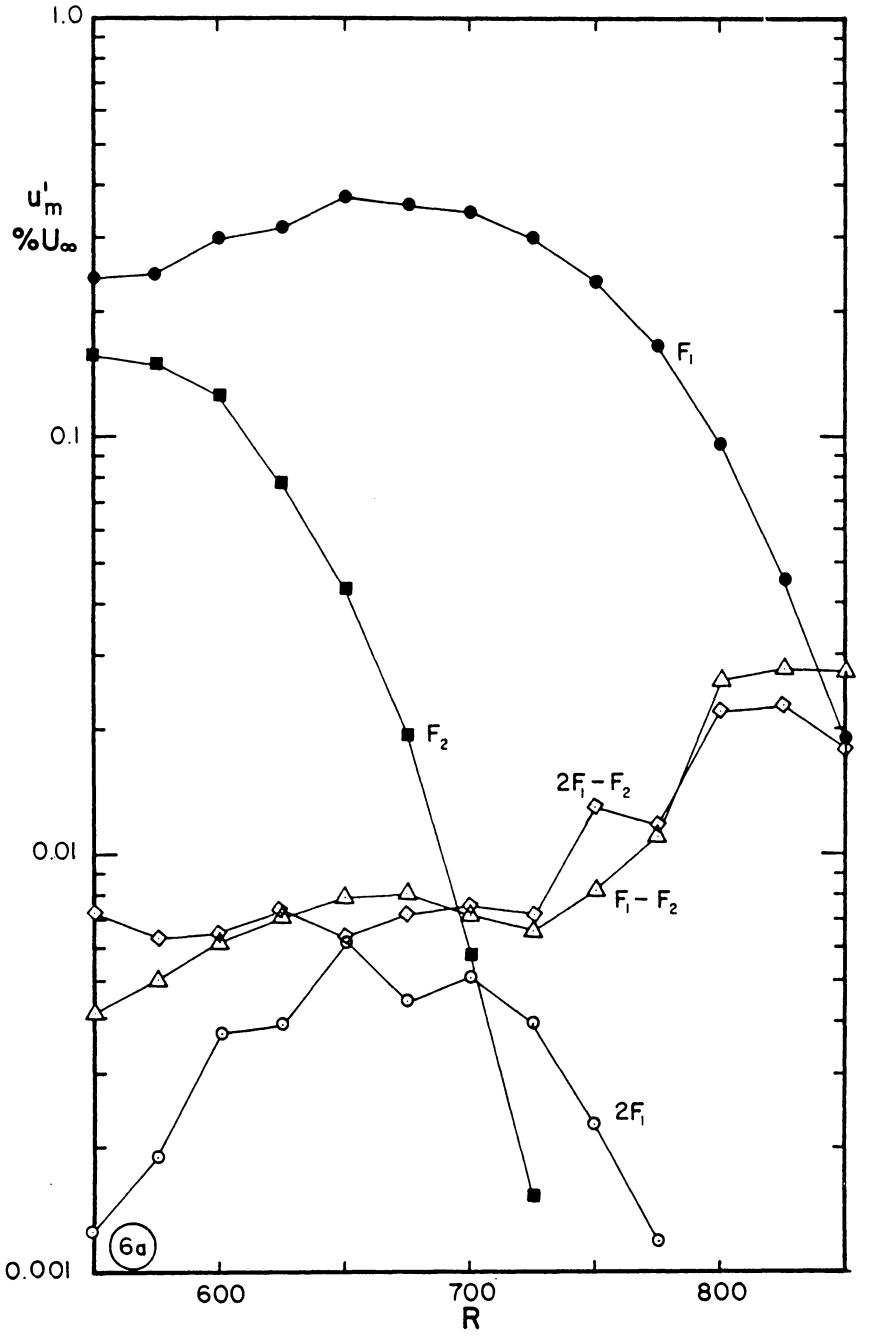

Figure 3.22 Results of nonlinear test case II - low amplitude.

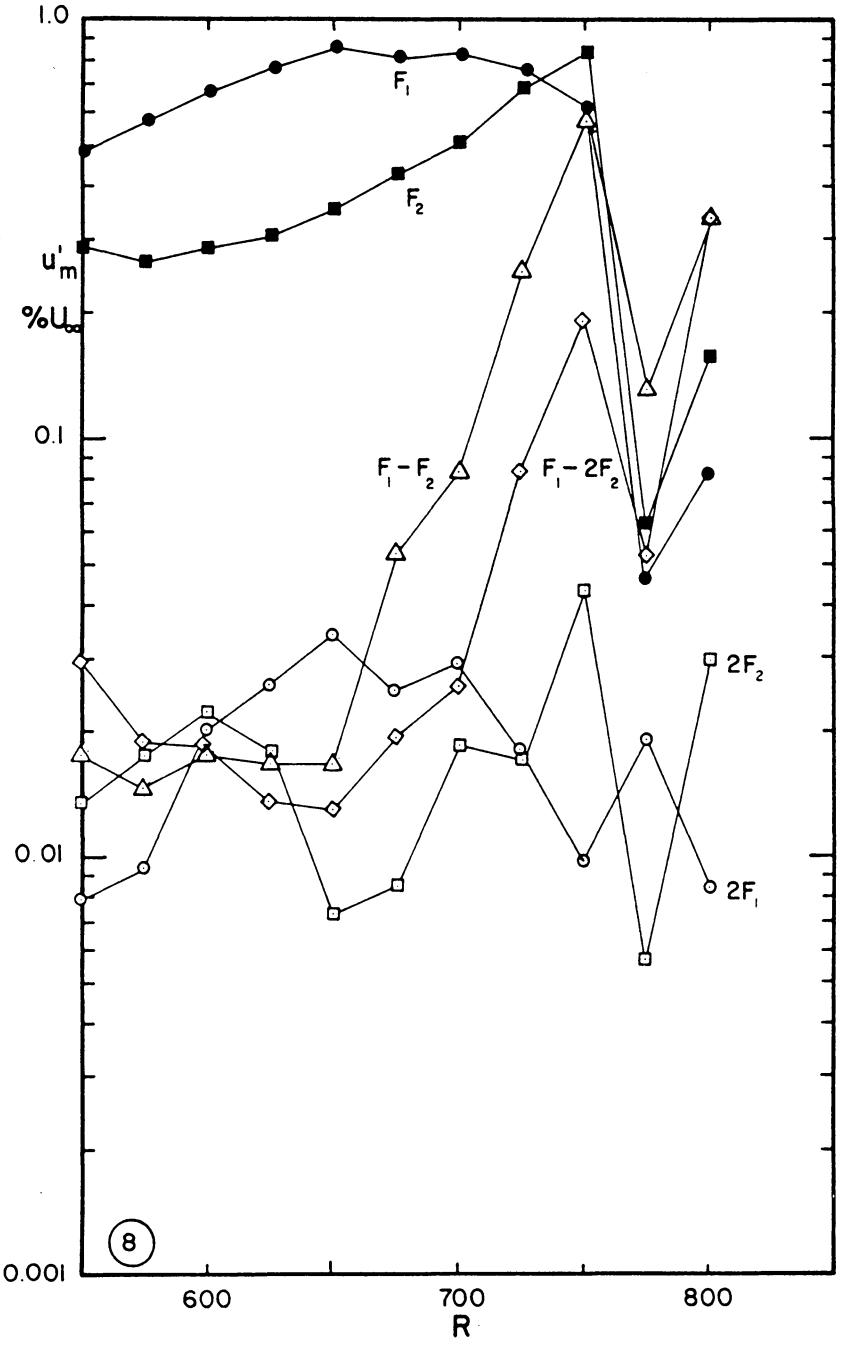

Figure 3.23 Results of nonlinear test case III - high amplitude.

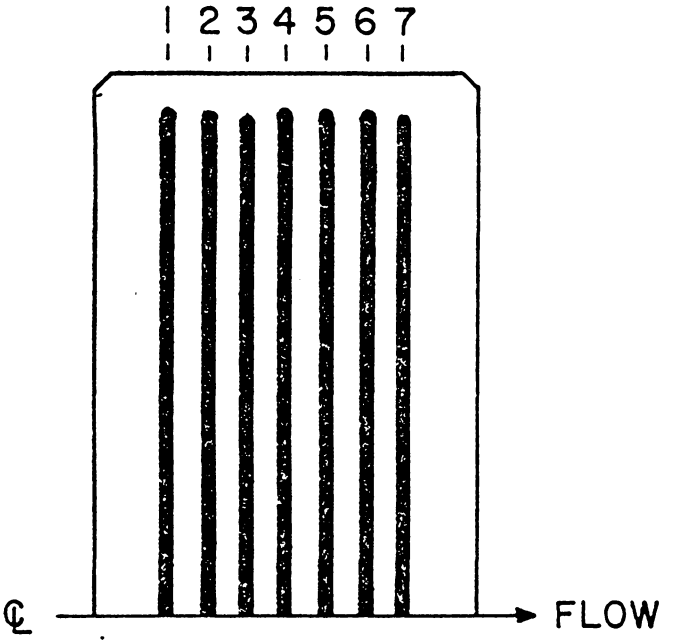

	1	2	3	4	5	6	7
PANEL # 1	184.8	187.9	191.1	194.3	197.5	200.6	203.8
PANEL # 2	238.1	241.2	244.4	247.6	250.8	253.9	257.1

Figure 3.24 Suction-strip locations in centimeters from the leading edge.

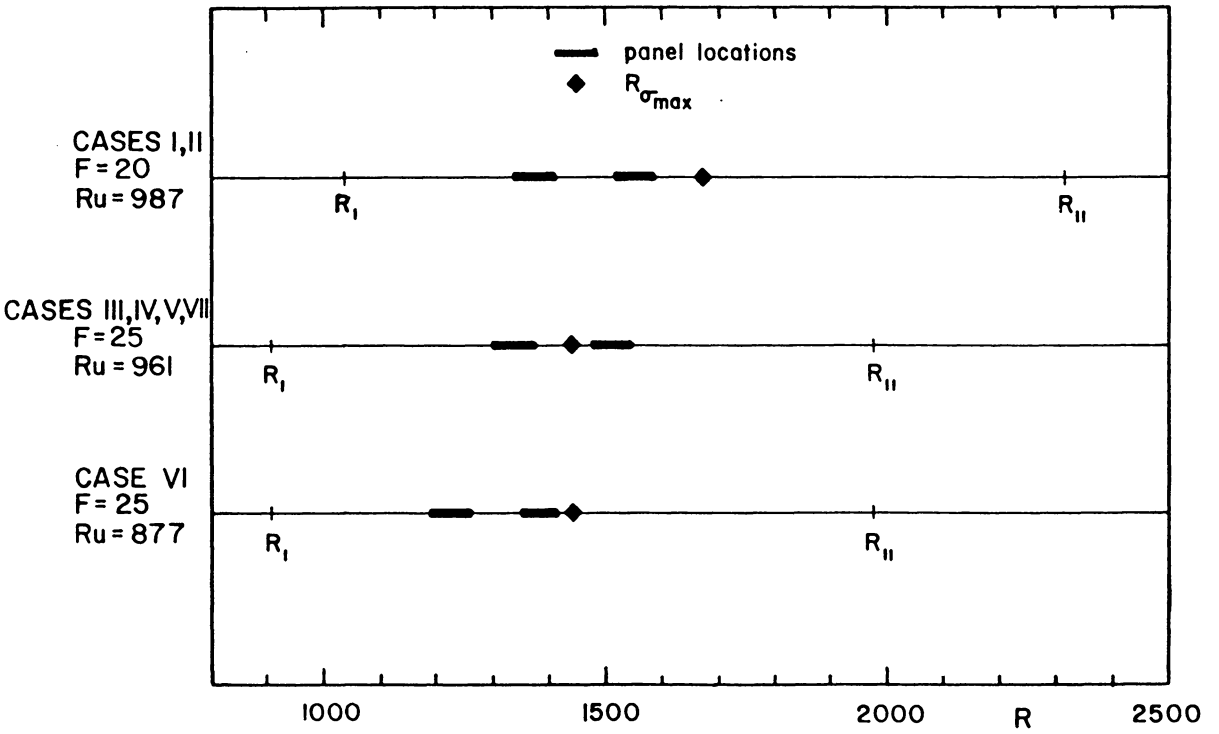

Figure 3.25 Suction-panel placement relative to the neutral stability curve for seven sucton cases.

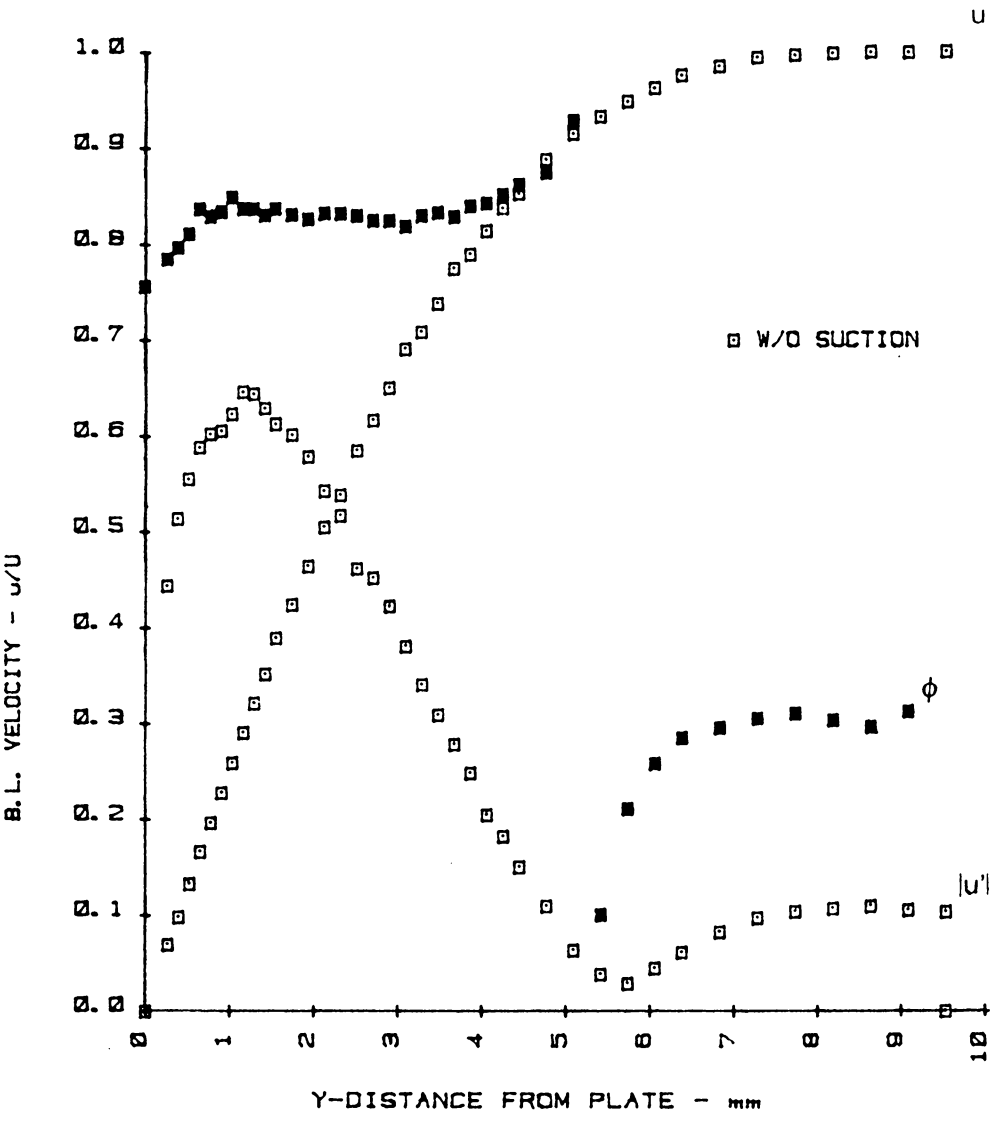

Figure 3.26 Boundary-layer profile of u, $|u'|$, and ϕ.

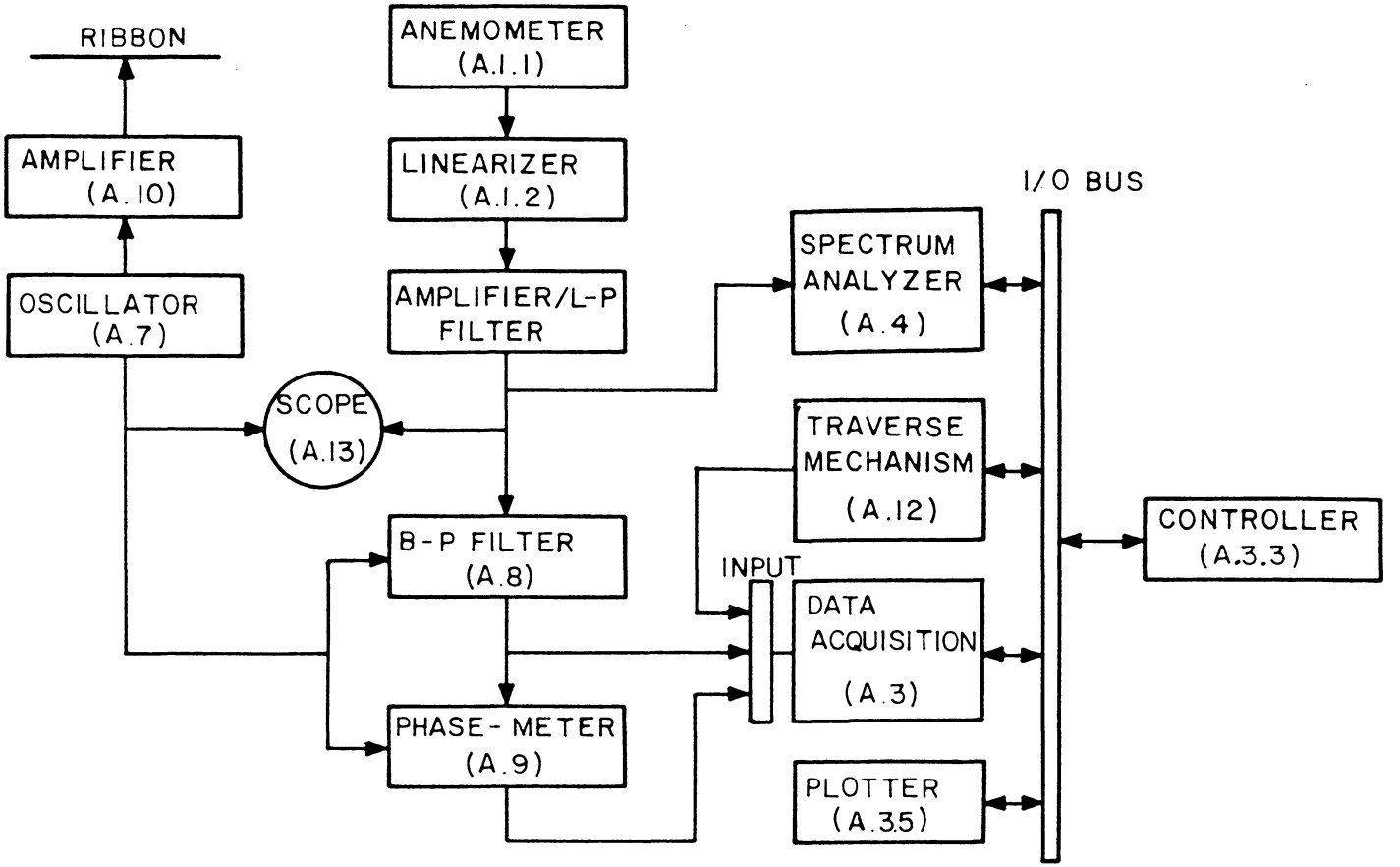

Figure 3.27 Flow chart of instrumentation for suction experiments.

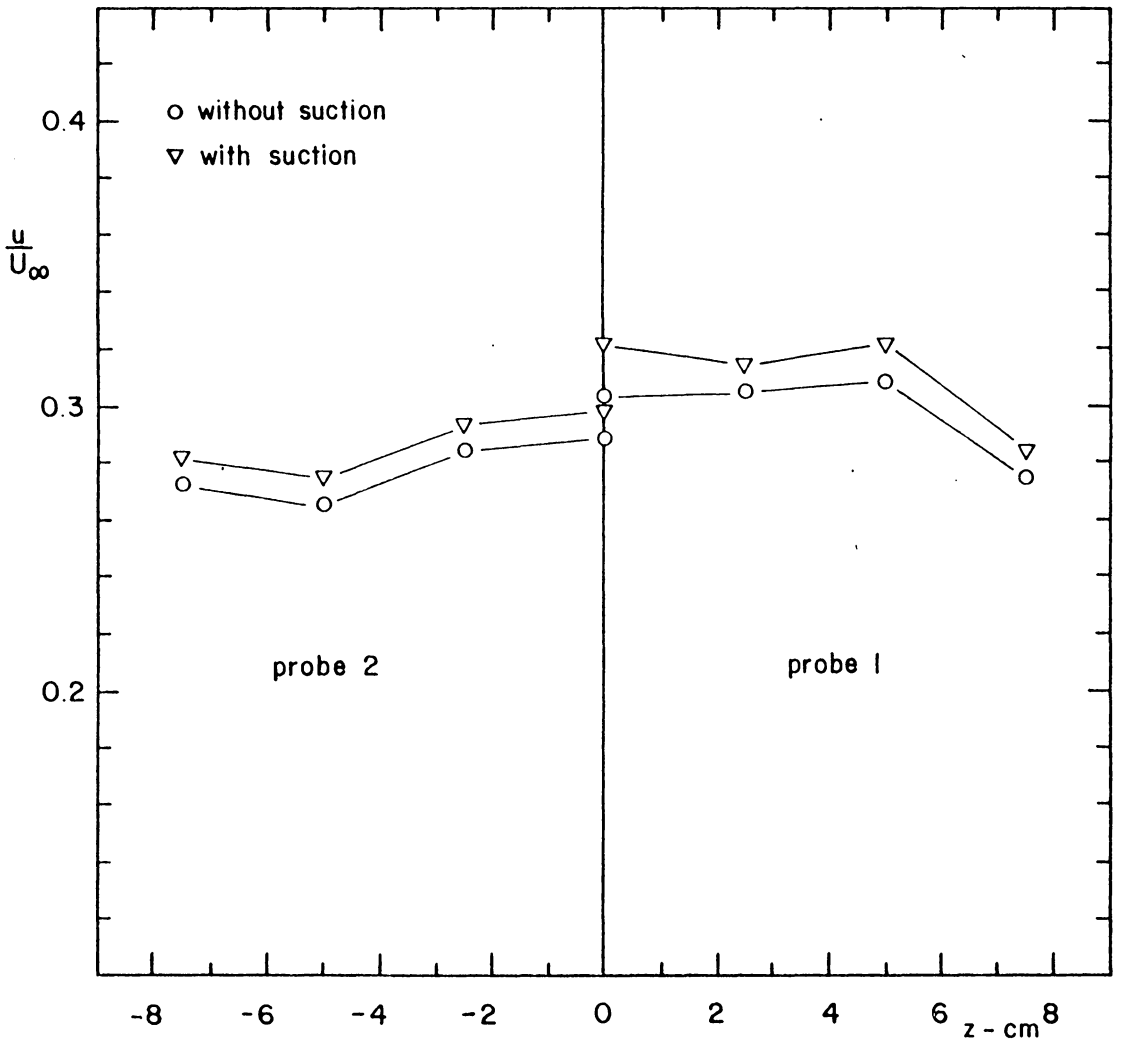

Figure 3.28 Spanwise mean-flow measurements with and without suction, obtained using multiple positions of two fixed probes.

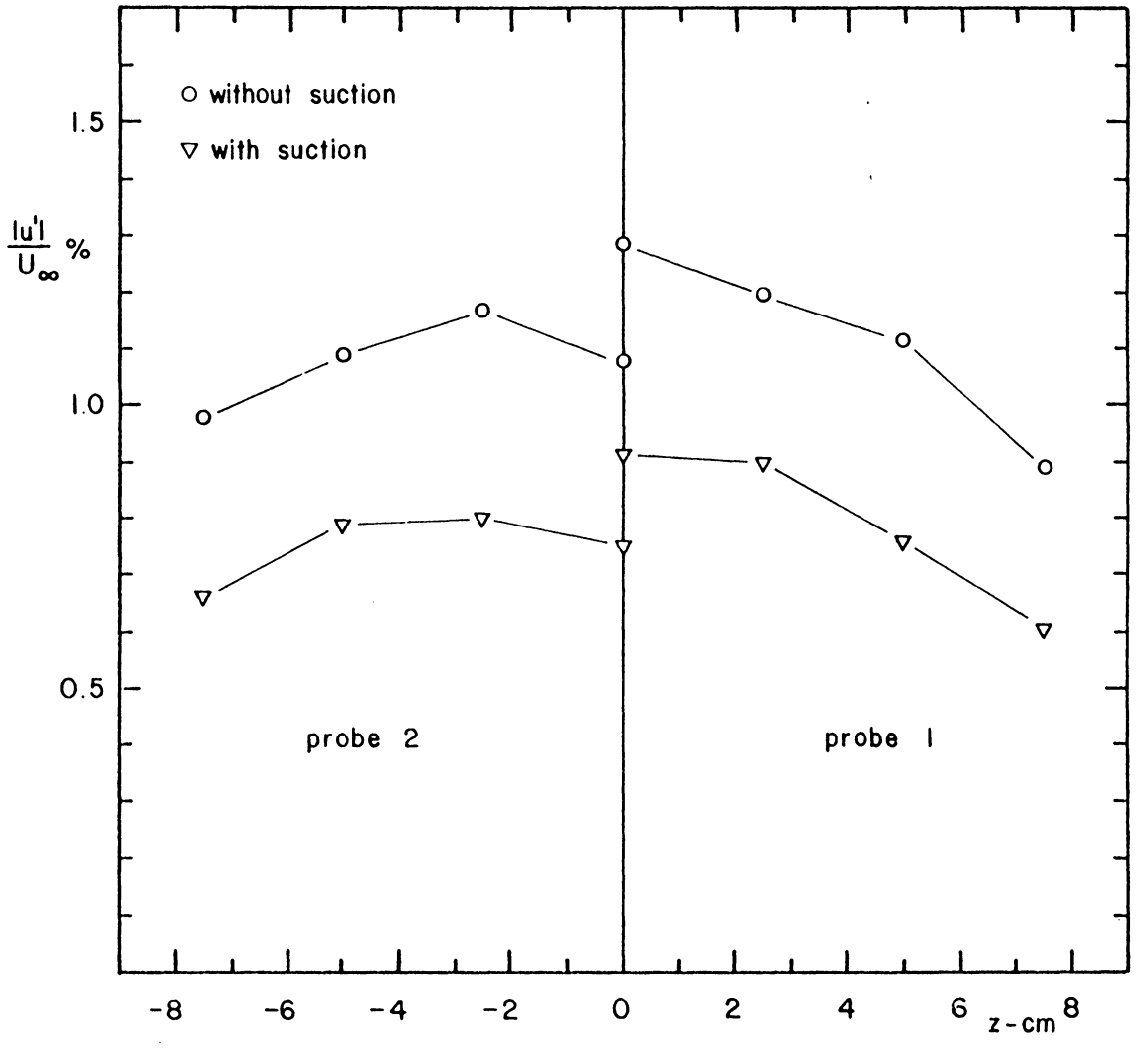

Figure 3.29 Spanwise disturbance-amplitude measurements with and without suction, obtained using multiple positions of two fixed probes.

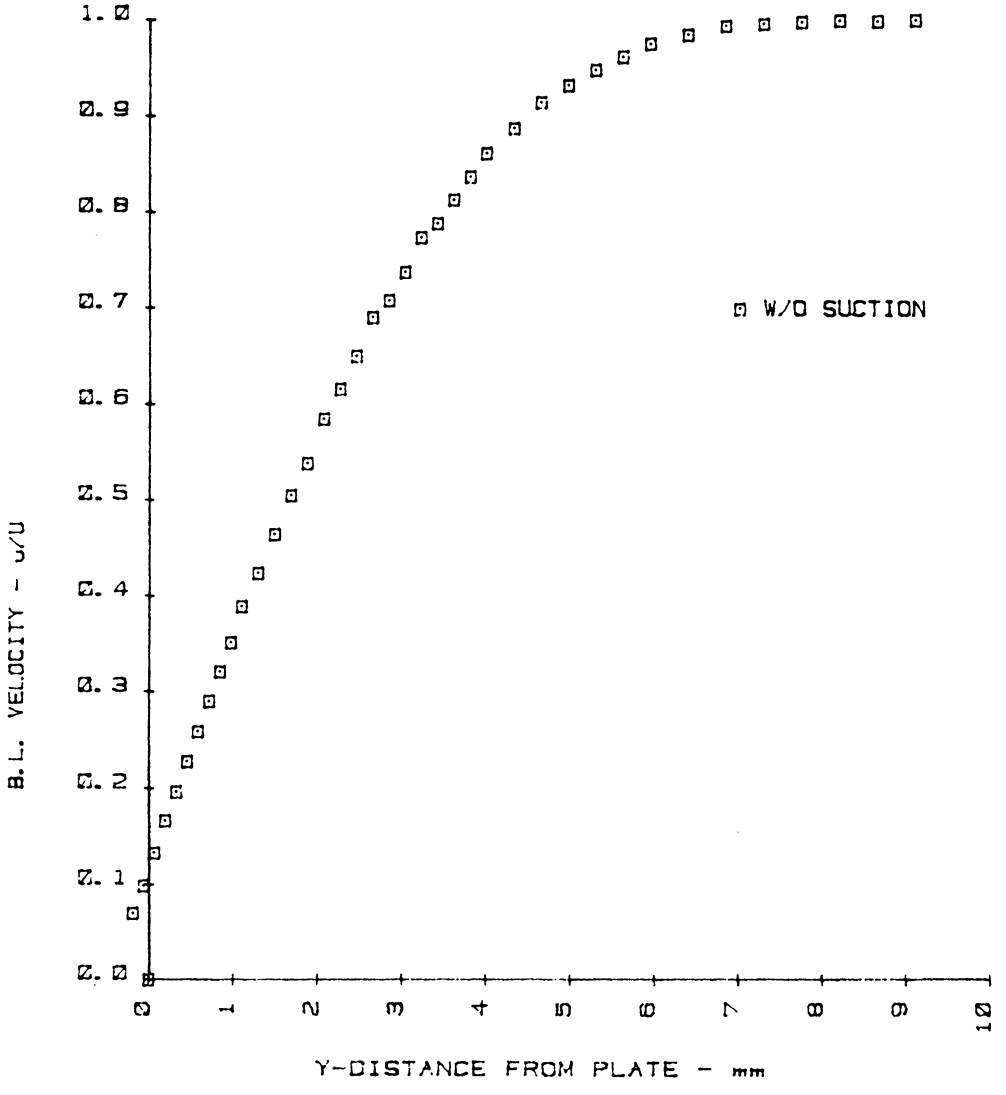

Figure 3.30 Mean-velocity profile before shifting.

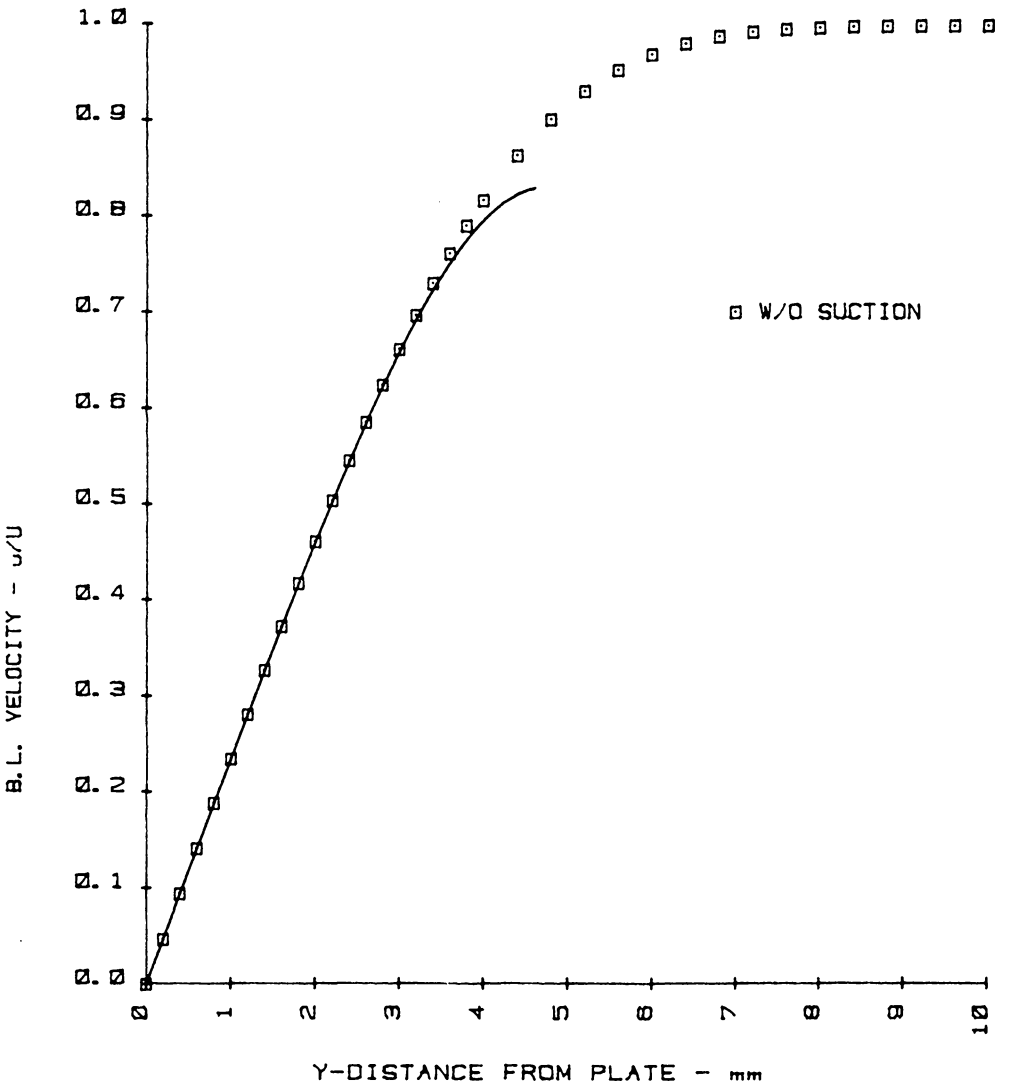

Figure 3.31 Curve fit of the Blasius Solution using $u = a\eta^4 + b\eta + c$.

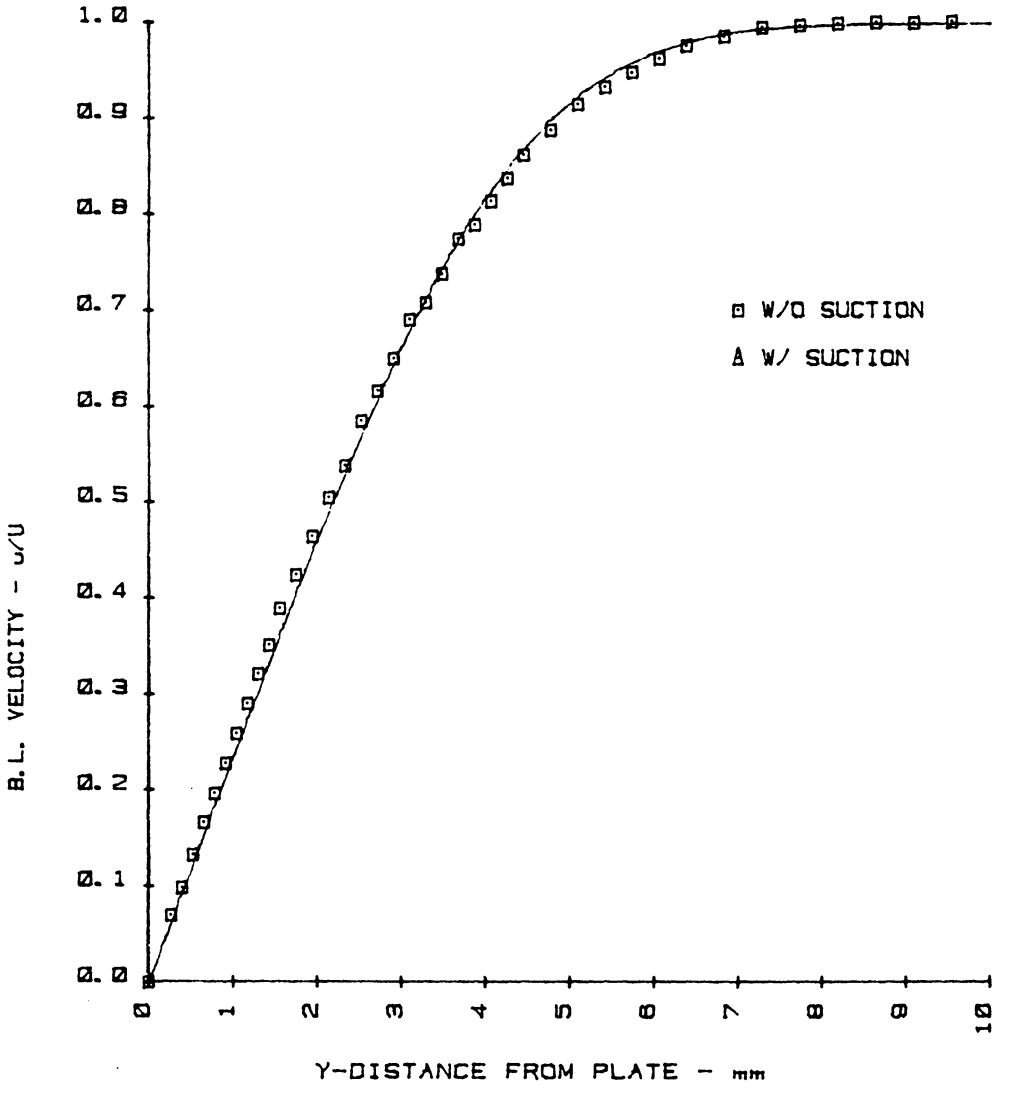

Figure 3.32 Mean-velocity data superposed on Blasius solution.

Suction Test Cases

Case No.	Frequency F x 10^6	Unit Reynolds No. Ru	No. Strips Opened panel #1	panel #2
I	20	987	0	1
II	20	987	1	0
III	25	961	1	0
IV	25	961	3	3
V	25	961	7	3
VI	25	877	7	3
VII	25	961	15	15

Figure 3.33 Table of seven suction test cases.

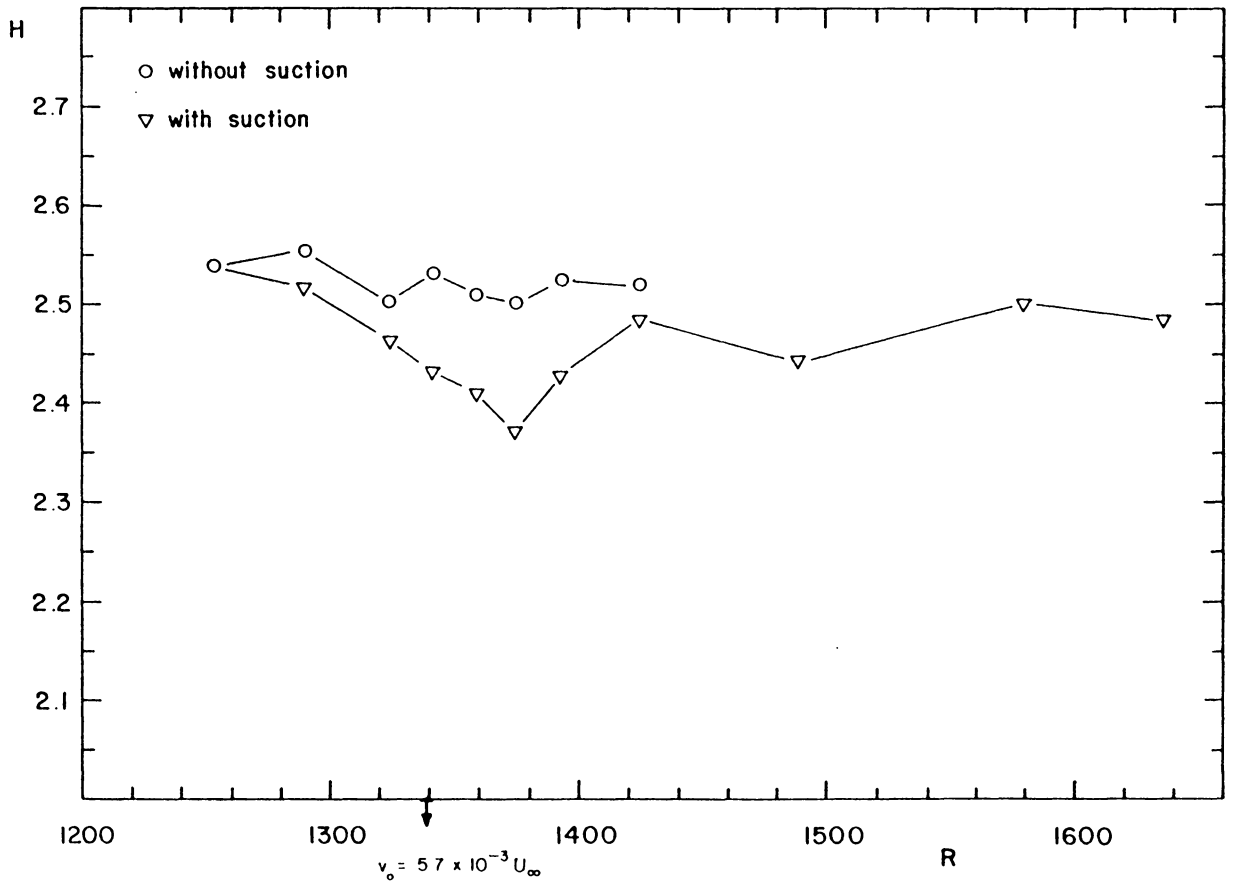

Figure 3.34 Shape factor variation for single suction-strip configuration, case III.

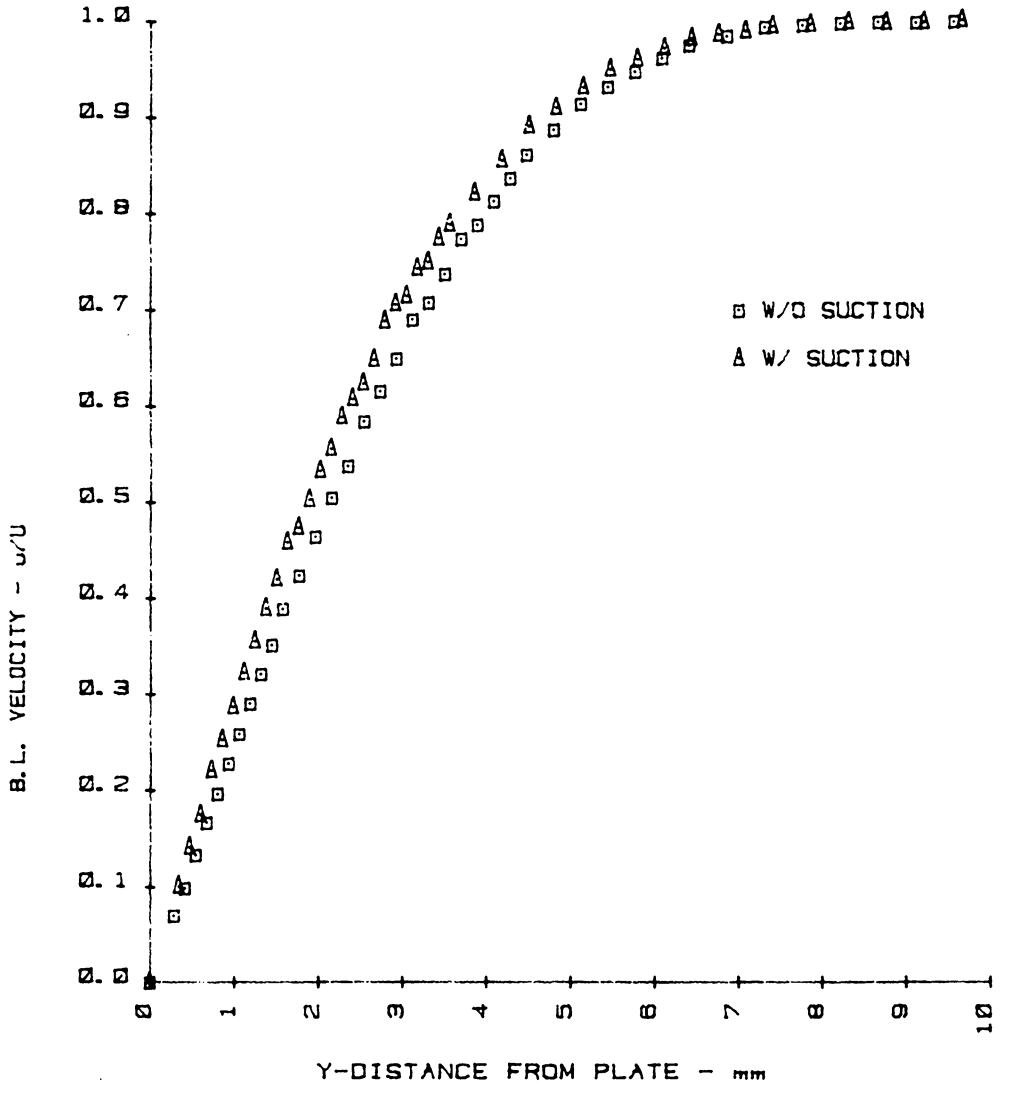

Figure 3.35 Mean-velocity profile with and without suction for case III, and at R = 1376.

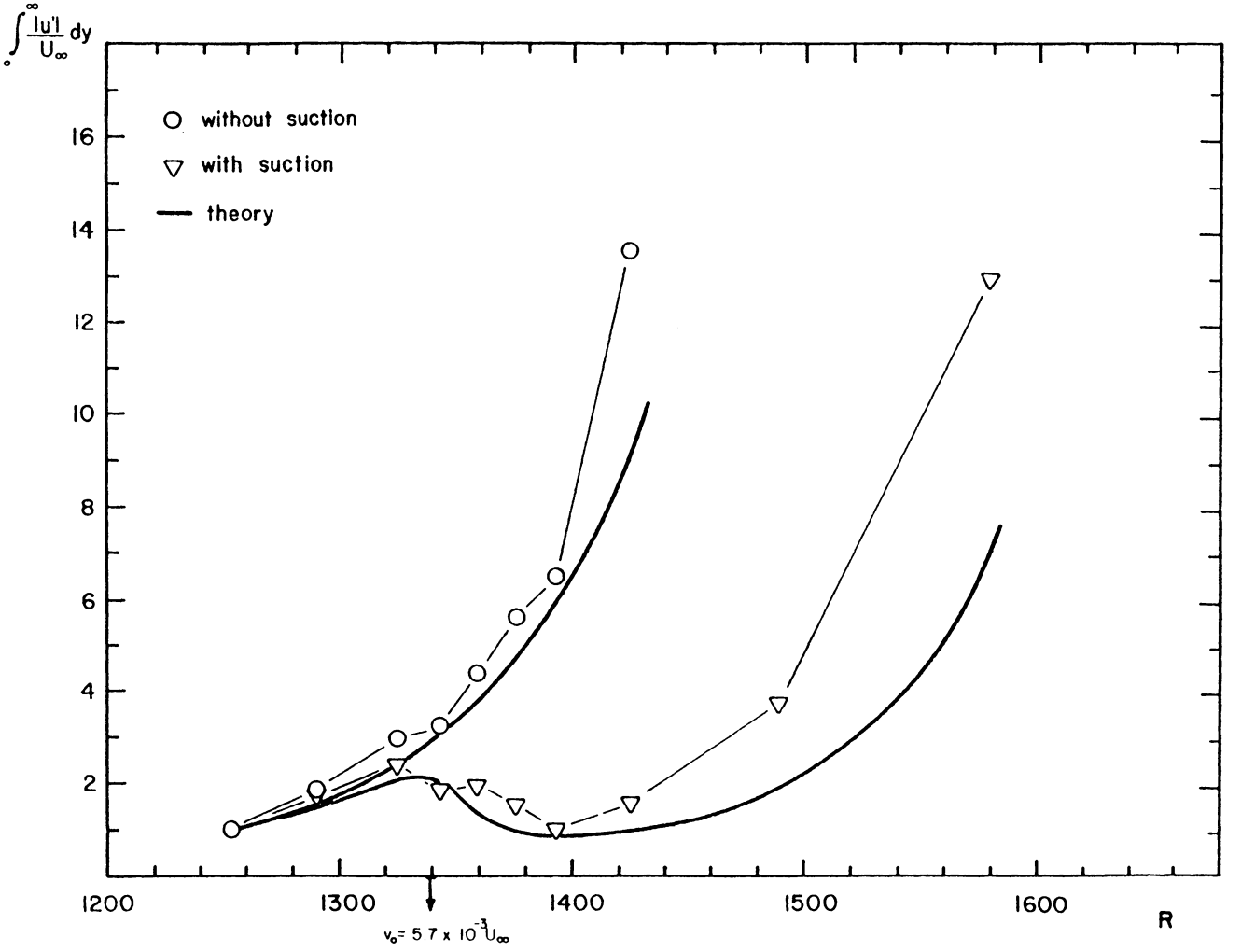

Figure 3.36 Results for suction-case III. Suction is located as shown on the abscissa.

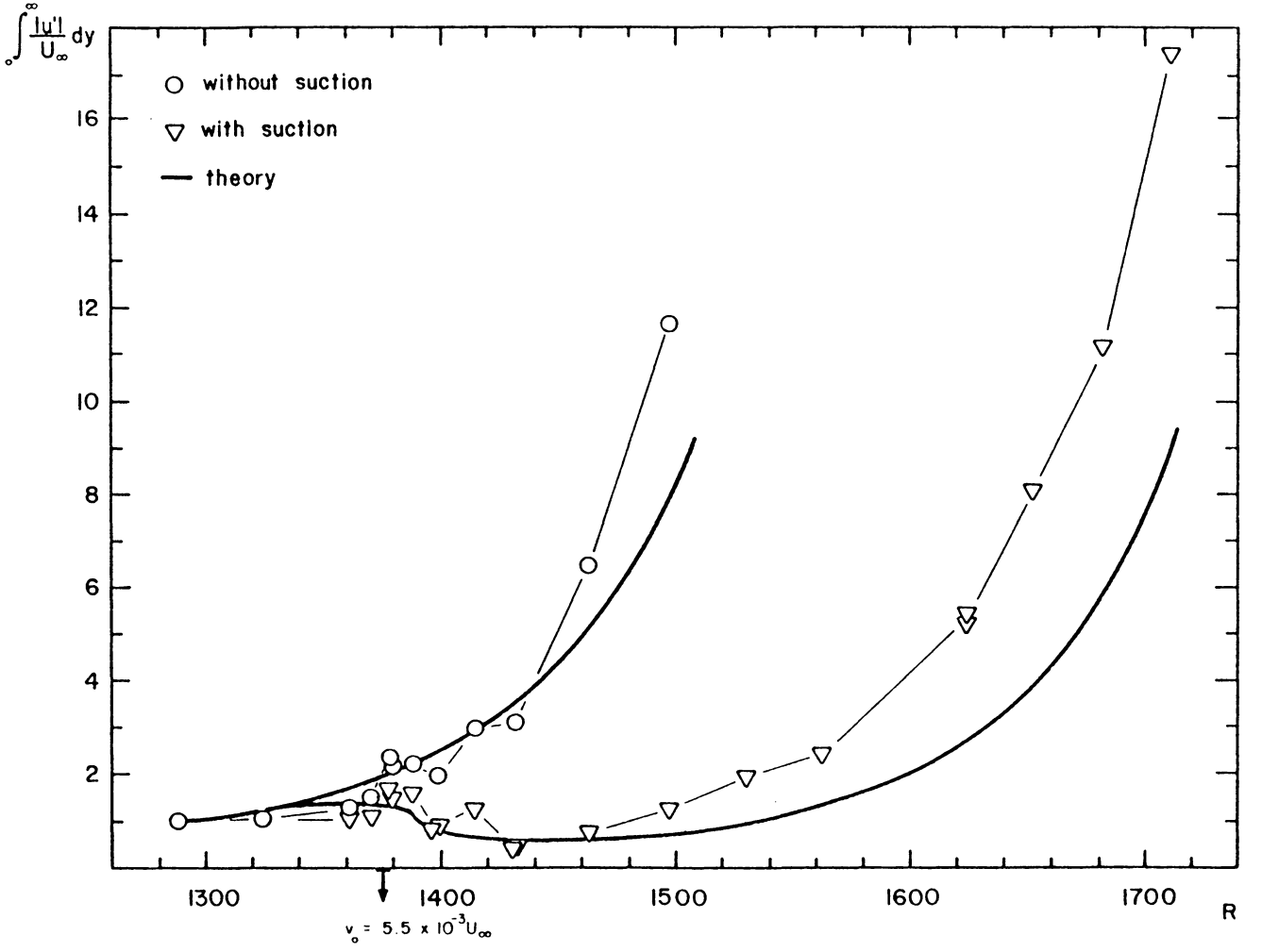

Figure 3.37 Results of suction-case II. Suction is located as shown on the abscissa.

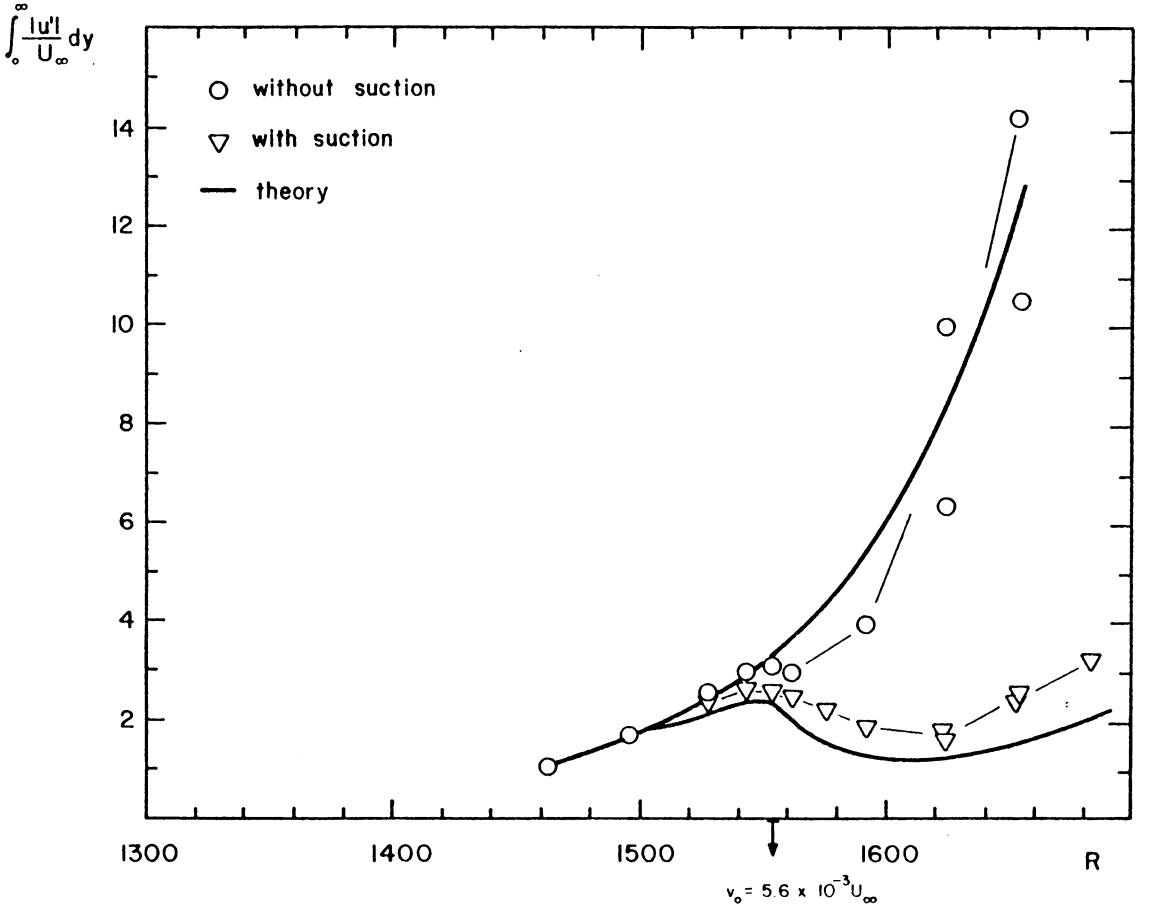

Figure 3.38 Results of suction-case I. Suction is located as shown on the abscissa.

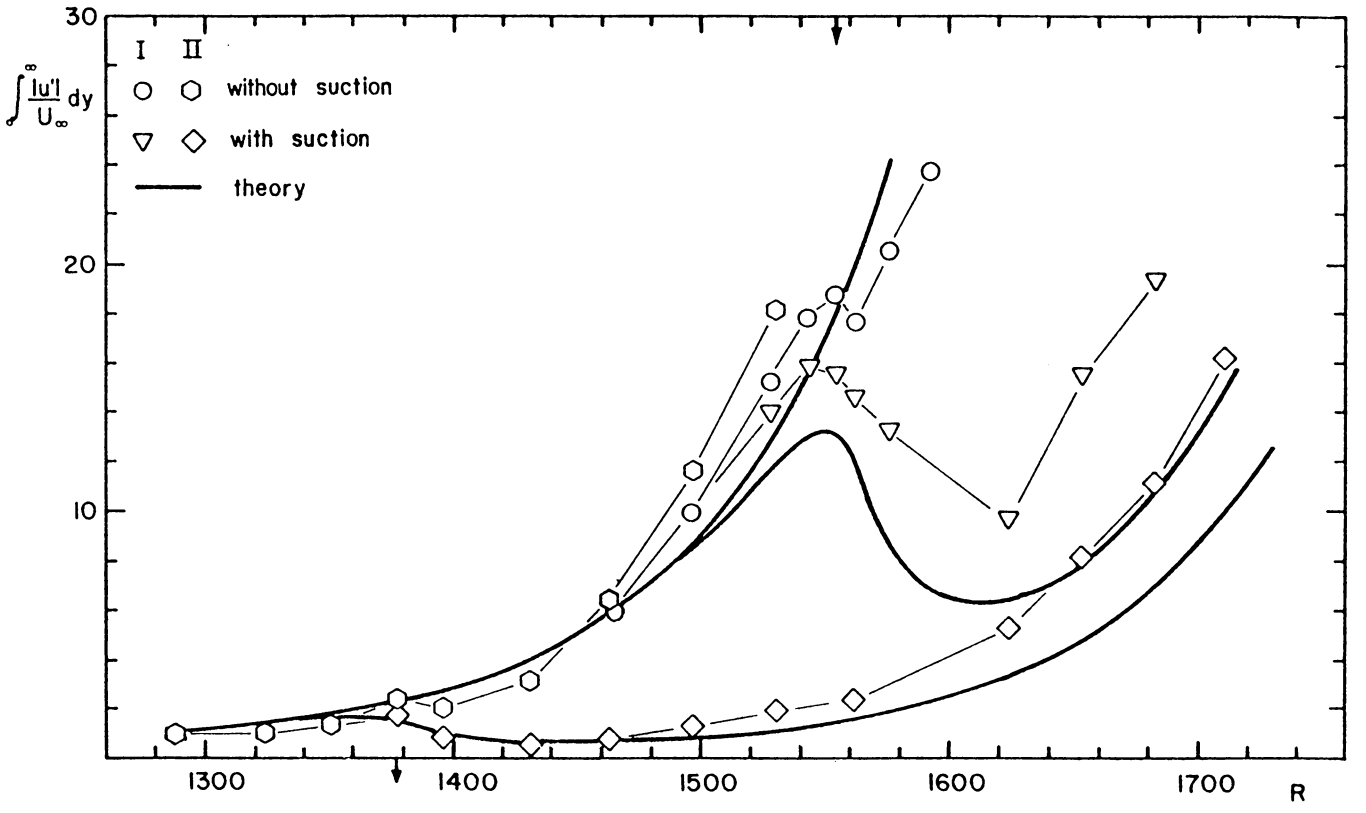

Figure 3.39 Results of suction-case I and II superposed. Suction is located as shown on the lower abscissa for case II and on the upper abscissa for case I.

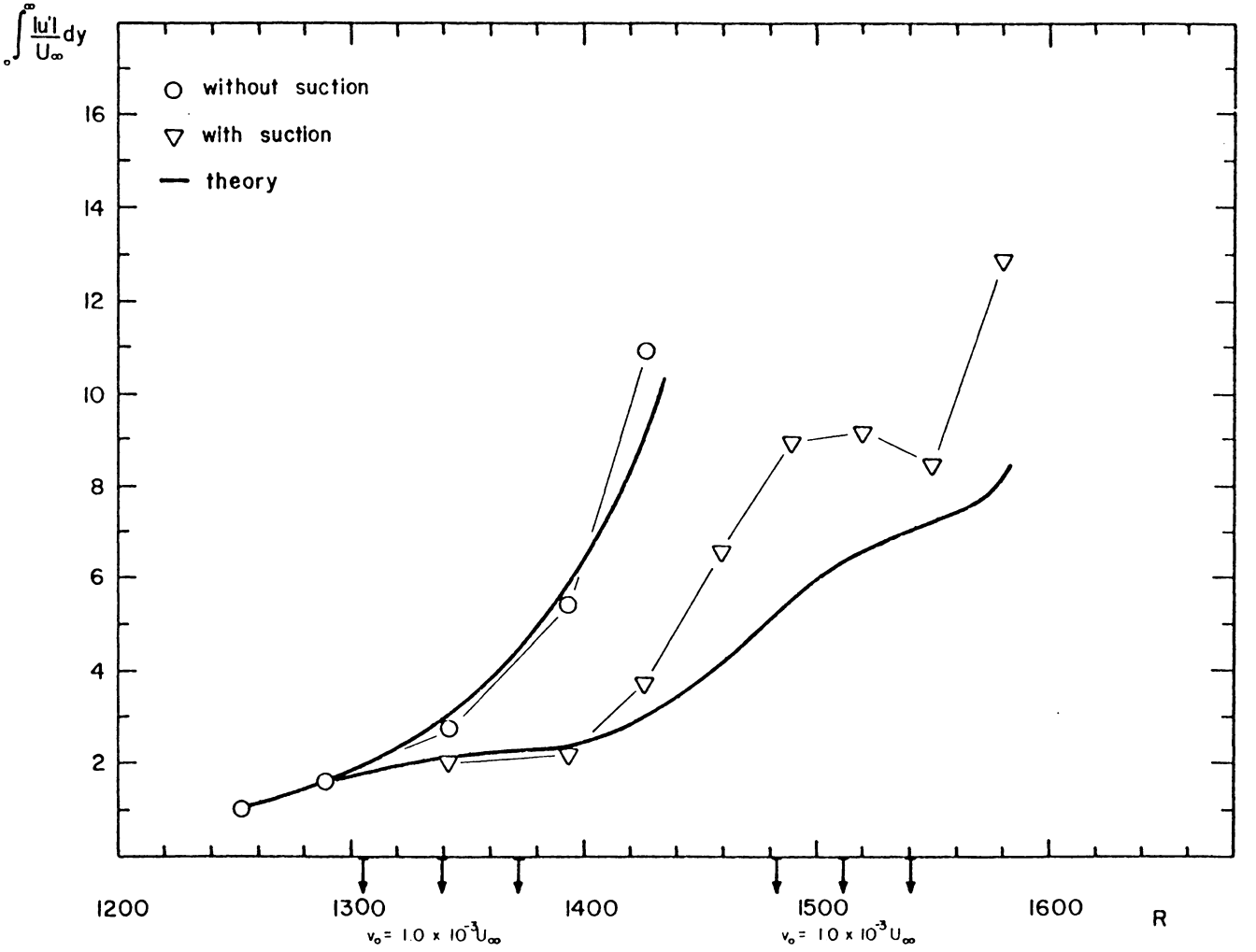

Figure 3.40 Results of suction-case IV. Suction is located as shown on the abscissa.

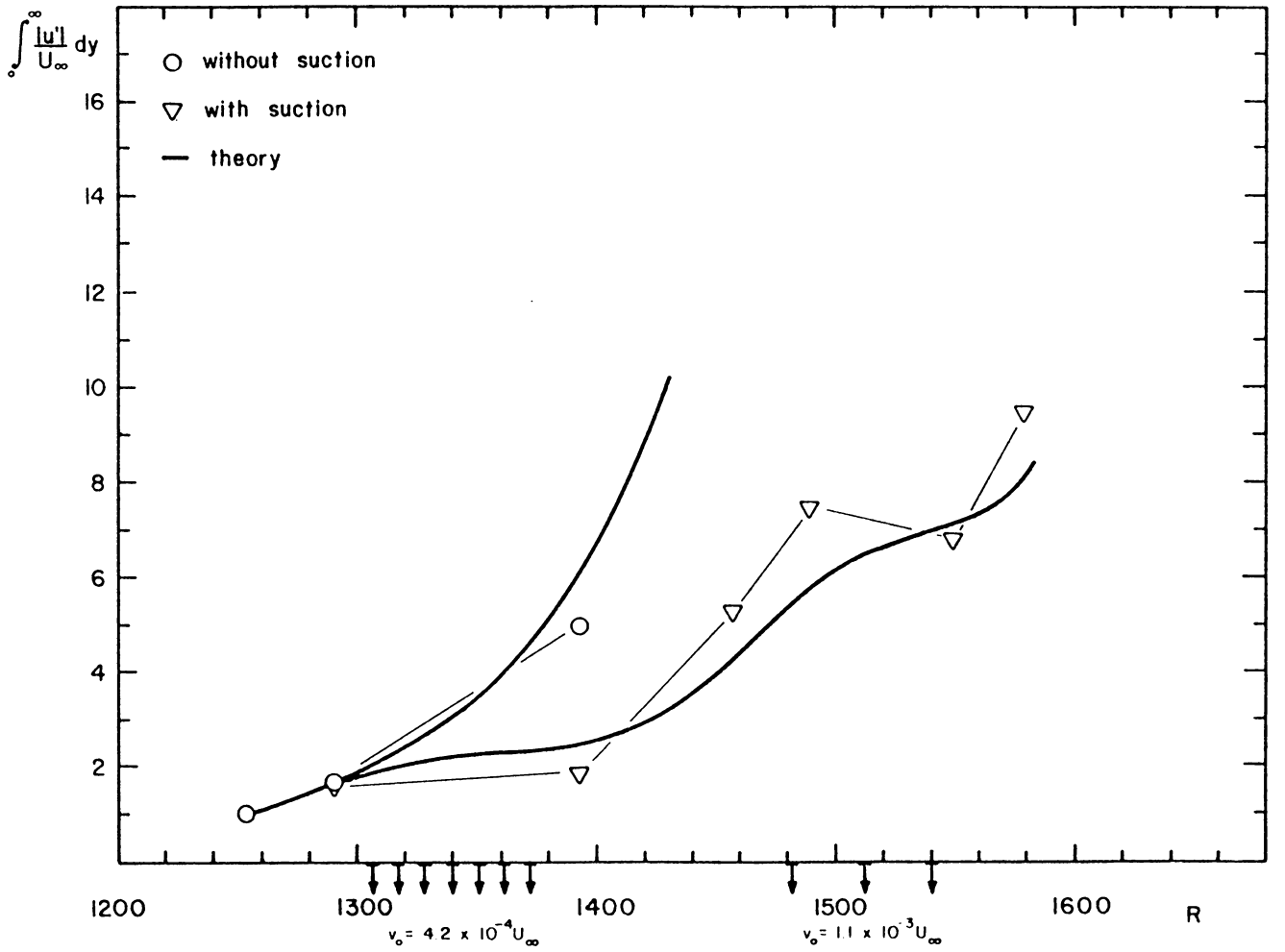

Figure 3.41 Results of suction-case V. Suction is located as shown on the abscissa.

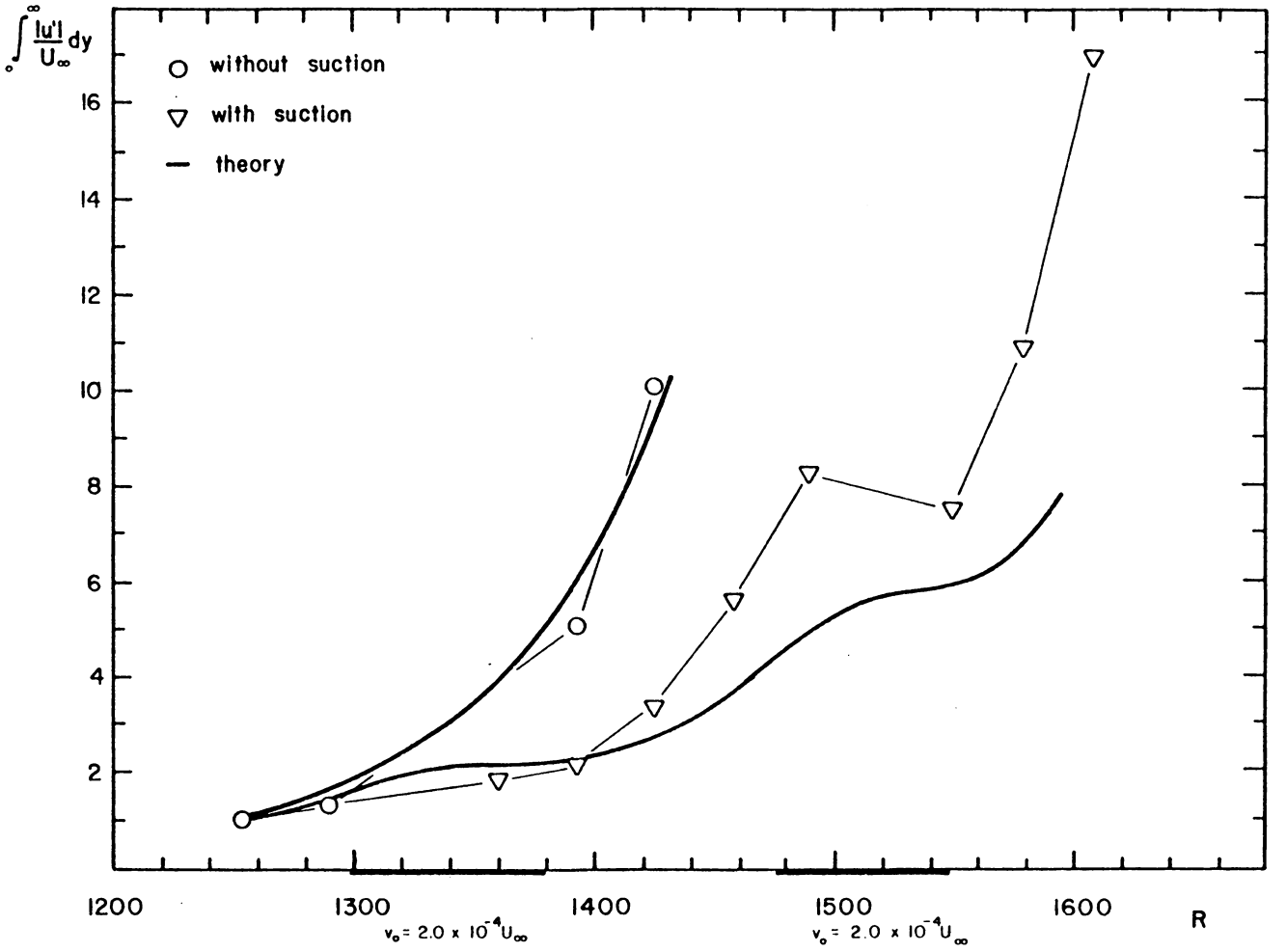

Figure 3.42 Results of suction-case VII. Suction is located as shown on the abscissa.

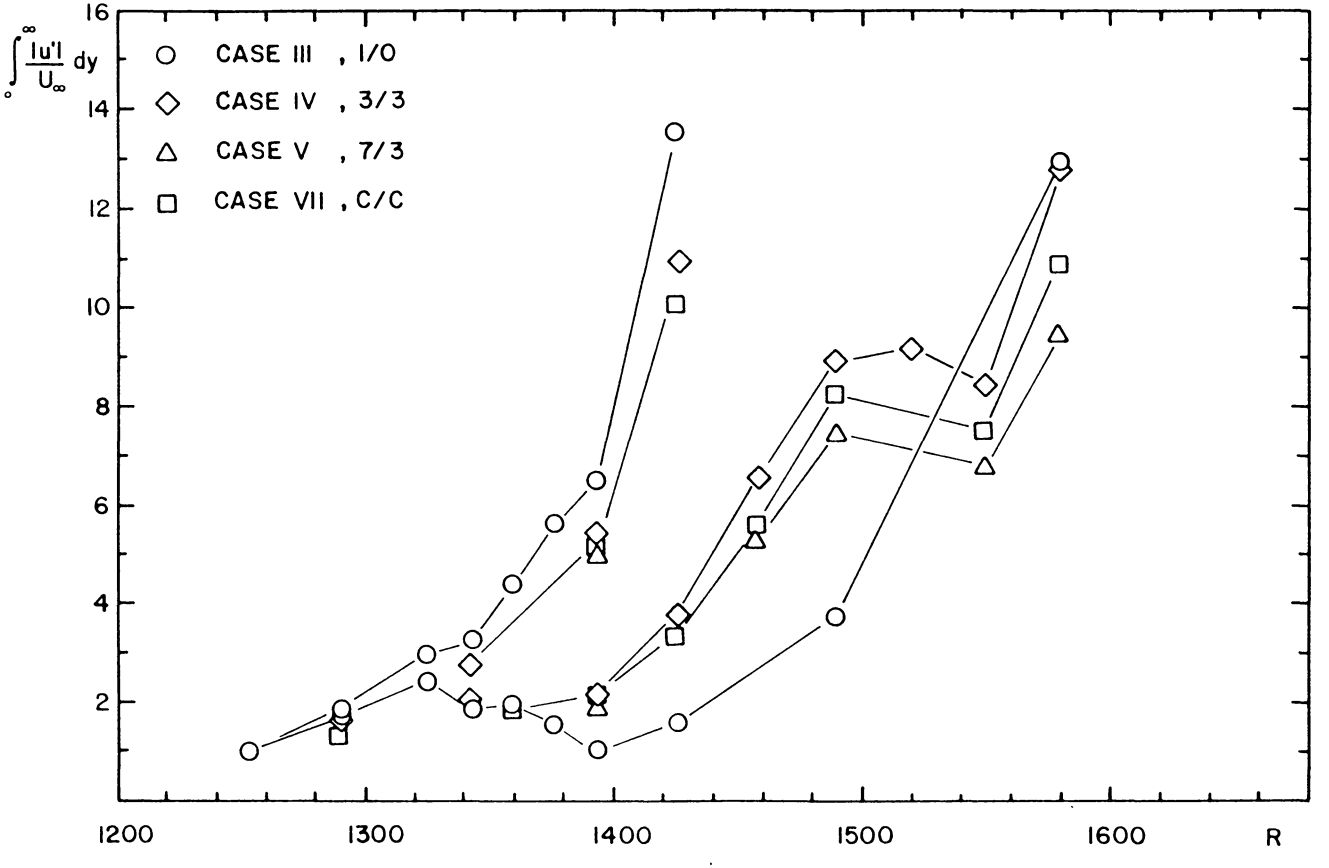

Figure 3.43 Results of suction-case III, IV, V, and VII superposed.

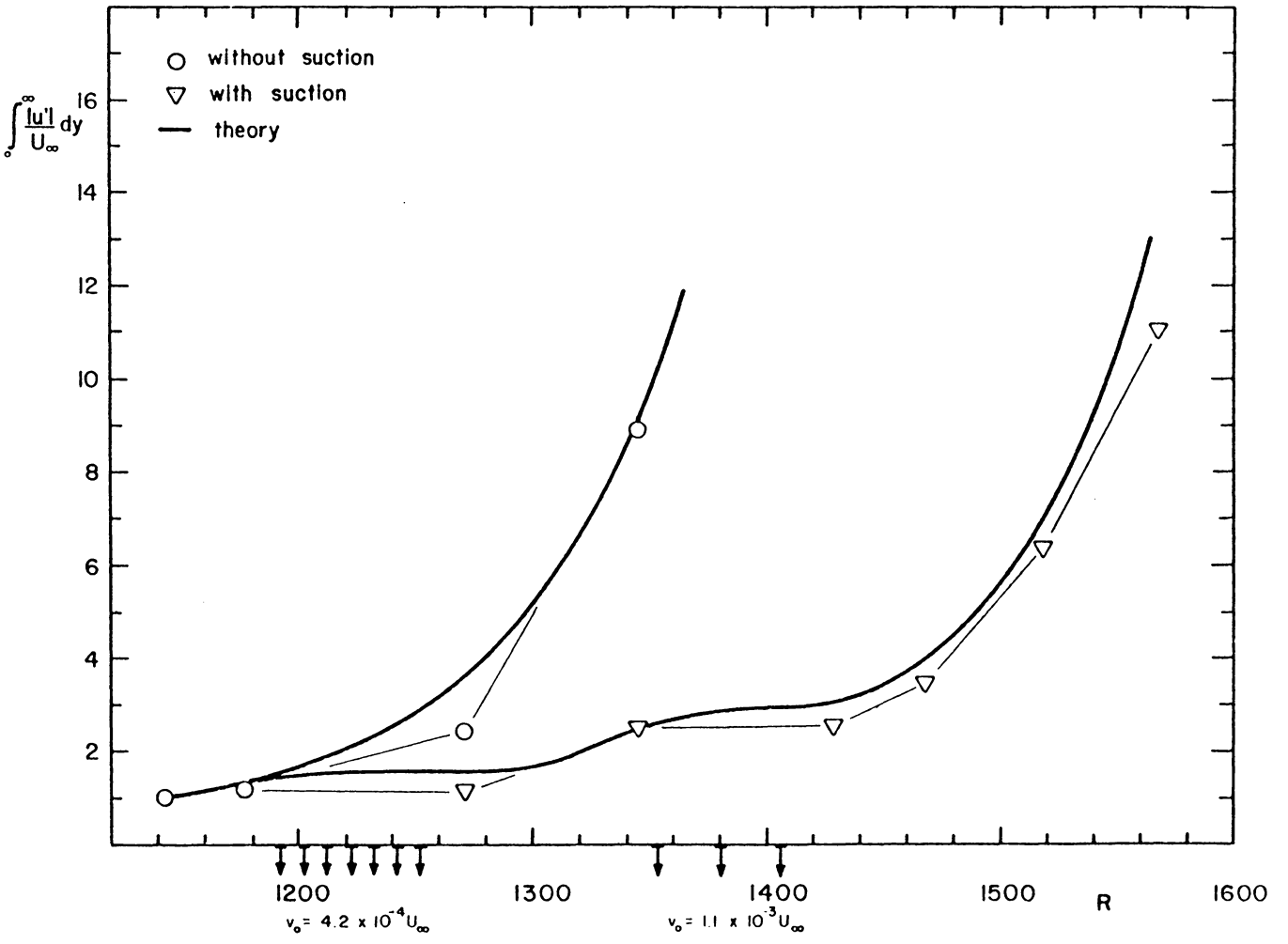

Figure 3.44 Results of suction-case VI. Suction is located as shown on the abscissa.

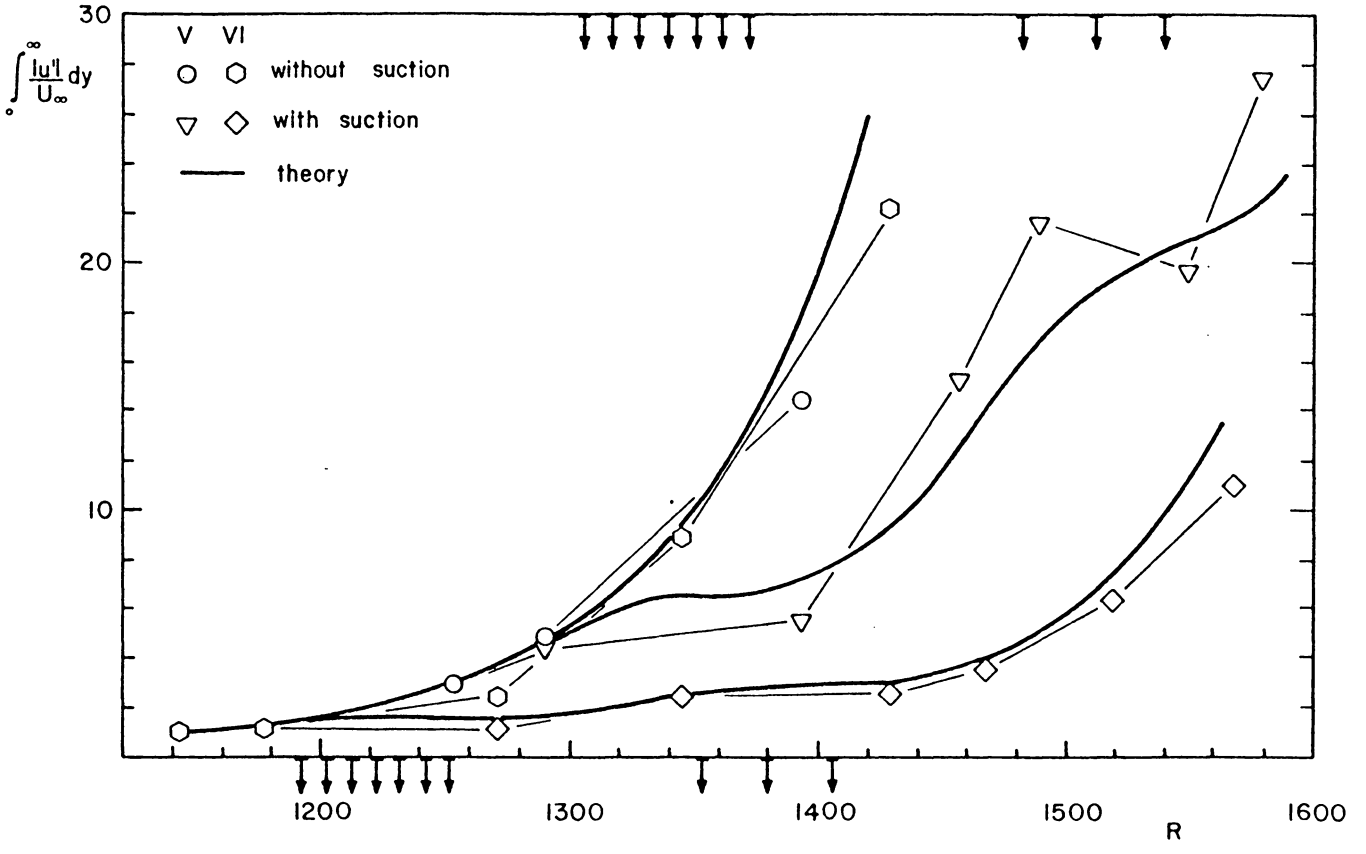

Figure 3.45 Results of suction-cases V and VI superposed. Suction is located as shown for case VI on the lower abscissa and for case V on the upper abscissa.

The vita has been removed from the scanned document

EXPERIMENTS ON THE STABILITY OF THE FLAT-PLATE BOUNDARY LAYER WITH SUCTION

by

Gregory A. Reynolds

(ABSTRACT)

The effects of boundary-layer suction in stabilizing the laminar boundary layer were considered in this experimental work. The experiments were conducted on a flat-plate wind-tunnel model in the V.P.I. & S.U. Stability Tunnel. The capabilities of the wind tunnel in terms of mean flow uniformity and low turbulence level were established and the basic flat-plate experiment was verified by comparison with the well known stability results for the Blasius boundary-layer. The two-dimensional Tollmein-Schlichting waves were introduced into the boundary layer using a vibrating ribbon.

Suction was applied through the model surface via two porous panels which could be located at various streamwise positions on the model. The porous Dynapore surface material of these panels was adapted by Douglas Aircraft Co. for possible use as a wing surface material on aircraft equipped with Laminar Flow Control. Detailed mean-flow measurements without suction showed that the Dynapore had no destabilizing effects in the laminar boundary layer.

Using the porous panels, suction could be applied either continuously or in a discrete fashion through spanwise suction strips. With suction applied through a single spanwise strip, the mean-flow

effects were determined in terms of the boundary-layer shape factor. Measurements of the disturbance behavior with suction were conducted to determine the relative merits of spatially continuous suction versus suction applied through various discrete suction strip configurations. These measurements were conducted in terms of the integral across the boundary layer of the streamwise disturbance amplitude, that is $A = \int |u'| dy$. These results were compared with the theory of Reed & Nayfeh (1981). A method was also proposed by this theory for optimization of suction strip placement, and measurements were made which provided partial confirmation as to the validity of this optimization scheme.

Experiments were also conducted without suction to investigate the weak nonlinear two- and three-wave interactions which occur at higher wave amplitudes. In these experiments, two-frequency Tollmein-Schlichting waves were introduced simultaneously using a single vibrating ribbon, and initial disturbance amplitudes were controlled. In particular, these experiments established appropriate initial conditions for comparison with analytical models and considered the role of the difference frequencies which were generated through the nonlinear interaction of the two fundamental waves. This work also considered the behavior of the harmonic waves in the nonlinear regime.